A combination of motion-compensated cone-beam computed tomography iame reconstruction and electrical impedance tomography

Pengpan, Thanyawee

Award date:
2012

Awarding institution:
University of Bath

A COMBINATION OF MOTION-COMPENSATED CONE-BEAM COMPUTED TOMOGRAPHY IMAGE RECONSTRUCTION AND ELECTRICAL IMPEDANCE TOMOGRAPHY

Thanyawee Pengpan

A thesis submitted for the degree of Doctor of Philosophy
University of Bath
Department of Electronic and Electrical Engineering
July 2012

Table of Contents

Table of Figures

Acknowledgements

I would like to express my gratitude to all those who gave me the possibility to complete this thesis. First and foremost, I am deeply thankful to my supervisor, Dr. Manuchehr Soleimani, for supporting me throughout my PhD study and research. He has provided me encouragement, guidance, and advice in all the time of research and writing up this thesis.

I would also like to state my gratitude to Dr. Nathan Smith who has provided me good teaching and explanation about iterative algorithms. He also helped me with proofreading, correcting and organising my two published papers.

I am indebted to my friends, Dr. Sarawut Kumphune and Nitirut Nernpermpisooth, for valuable suggestions and assistances.

I would also like to express my gratitude to the Thai Government Science and Technology Scholarship for the award of Commission of Higher Education Scholarship, which has supported me during my PhD, and the Office of Education Affairs, London, for support.

Finally, I would like to give my special thanks to my family for their love, understanding and supporting throughout my life. Without them, I would not have finished the degree.

Abstract

Cone-beam computed tomography (CBCT) is an imaging technique used in conjunction with radiation therapy. CBCT is used to verify the position of tumours just prior to radiation treatment session. The accuracy of the radiation treatment of thoracic and upper abdominal tumours is heavily affected by respiratory movement. Blurring artefacts, due to the movement during a CBCT scanning, cause misregistration between the CBCT image and the planning image. There has been growing interest in the use of motion-compensated CBCT for correcting the breathing-induced artefacts. A wide range of iterative reconstruction methods have been developed for CBCT imaging. The direct motion compensation technique has been applied to algebraic reconstruction technique (ART), simultaneous ART (SART), ordered-subset SART (OS-SART) and conjugate gradient least squares (CGLS). In this thesis a dual modality imaging of electrical impedance tomography (EIT) and CBCT is proposed for the first time. This novel dual modality imaging uses the advantages of high temporal resolution of EIT imaging and high spatial resolution of the CBCT method. The main objective of this study is to combine CBCT with EIT imaging system for motion-compensated CBCT using experimental and computational phantoms. The EIT images were used for extracting motion for a motion-compensated CBCT imaging system. A simple motion extraction technique is used for extracting motion data from the low spatial resolution EIT images. This motion data is suitable for input into the direct motion-compensated CBCT. The performance of iterative algorithms for motion compensation was also studied. The dual modality CBCT-EIT is verified using experimental EIT system and computational CBCT phantom data.

List of Abbreviations

1D	One Dimension
2D	Two Dimension
3D	Three Dimension
4D	Four Dimension
AP	Anteroposterior
ART	Algebraic Reconstruction Technique
CBCT	Cone-Beam Computed Tomography
CGLS	Conjugate Gradient Least Squares
cm	Centimetre
CT	Computed Tomography
EIDORS	Electrical Impedance Tomography and Diffuse Optical Tomography Reconstruction Software
EIT	Electrical Impedance Tomography
EPIDs	Electronic Portal Imaging Devices
FBP	Filtered-Back Projection
FDK	Feldkamp, Davis and Kress algorithm
GPU	Graphics Processing Unit
GTV	Gross Tumour Volume

IGRT	Image-Guided Radiation Therapy
Linac	Linear Accelerator
mA	Milli-ampere
MIT	Magnetic Induction Tomography
mm	Millimetre
MRI	Magnetic Resonance Imaging
MSCT	Multi-Slice Computed Tomography
MSE	Mean Square Error
NCAT	NURBS-based Cardiac-Torso
NI	National Instruments
NURBS	Non-Uniform Rational B-Splines
OS-SART	Ordered-Subset Simultaneous Algebraic Reconstruction Technique
PET	Positron Emission Tomography
PTV	Planning Treatment Volume
RMSE	Root Mean Square Error
SART	Simultaneous Algebraic Reconstruction Technique
SBRT	Stereotactic Body Radiotherapy
SI	Superoinferior
SPECT	Single Photon Emission Computed Tomography

Chapter 1
Introduction

Radiotherapy is a method of treatment for cancer using ionizing radiation. The purpose of radiotherapy is to kill cancer cells with high radiation dose whilst the normal tissue around the tumour must be affected as less as possible. In practice, radiotherapy is performed by more than one radiation beam, not only to achieve the planned radiation dose but also to reduce the radiation dose to the critical organs and normal tissues around the tumour. Segmented beam delivery that is fractionated. However, due to the tumour movement, extending the treatment volume is aimed to ensure that the target receives the planned doses during the treatment (EKBERG et al., 1998). On the other hand, the critical organs and normal tissues should receive as low radiation dose as possible. This technique introduces unnecessary radiation doses to healthy tissues. Moreover, the size, shape, and location of the tumour can change during the treatment course which results in radiation delivery errors. In addition, the patient positioning and machine set-up errors can also be found due to shifting of the makers on patient skin and changing of patient shape.

In an attempt to verify the patient treatment position, irradiation fields and target location, size and shape as planned prescriptions, image-guided radiation therapy (IGRT) has been introduced for improving the delivery of radiation treatment to tumours by using an imaging system before receiving the treatment fraction. The verifying image is used in compare with reference images produced during the planning process. The errors can be compensated by the patient set-up adjustments. A wide range of imaging systems have been used in radiotherapy for patient position

verification. The developments in the imaging technology encourage the improvements in the accuracy of the patient verification. The early IGRT was incorporated with a radiographic portal imaging. The portal radiographs were irradiated by the megavoltage (MV) X-ray beam resulting in poor image contrast, low image quality and lack of immediate results. Due to an introduction of digital imaging, electronic portal imaging devices (EPIDs) were developed. The main advantage of this system is providing real-time digital images (no longer need the film processing process) (ANTONUK, 2002). Then, a kilo-voltage fluoroscope was introduced to IGRT which produces an improved contrast and real-time images. The developments in the diagnostic imaging play as an important role for the imaging technique in radiotherapy. Computed tomography (CT) was first developed for the diagnostic purpose, then has been used as in-room imaging system in radiotherapy (AOKI et al., 1987). This enables volumetric imaging and produces diagnostic CT image quality. However, the transferring patient from imaging couch to treatment couch is needed which may lead to a patient positioning error (DAWSON and JAFFRAY, 2007) . To avoid this type of errors, CT was combined into the treatment machine by using the CT detector with mega-voltage X-rays source, so called "mega-voltage CT (MVCT). The MVCT produces sufficient images quality for verifying the patient's position but, due to higher energy radiation, the image quality is lower than the diagnostic CT (RUCHALA et al., 1999). Recently in the field of IGRT, cone-beam CT (CBCT) was combined with the treatment machine to improve the accuracy of treatment verification (JAFFRAY et al., 2002, DIETRICH et al., 2006, BODA-HEGGEMANN et al., 2011). Moreover, the technology of CBCT, integrated with treatment machine, provides the patient's images in the same position as the position of radiation treatment without moving and also produces higher image quality than MVCT.

CBCT is a volumetric imaging system, which couples a kilo-voltage X-ray source with a large area two-dimensional (2D) detector, in order to produce three-dimensional (3D) tomographic images. This X-ray source produces a wide angle beam while the diagnostic X-ray source produces a narrow angle beam. A major limitation of CBCT is movements of the internal organs, especially the treatment of

the thoracic and abdominal parts (BALTER et al., 1996, BORTFELD et al., 2002, GOITEIN, 2004, CHEN et al., 2004). A set of 2D projections is collected over 30 to 240 second (DAWSON and JAFFRAY, 2007), while the respiratory cycle period is about 5 seconds. Therefore, the chest is continuously moving during CBCT acquisition, which results in blurring artefacts on tumour boundary in CBCT images and leads to misregistration between the CBCT image and the planning image (PURDIE et al., 2007, SHIRATO et al., 2007, SONKE et al., 2008, SONG et al., 2009).

To show the effects of respiratory motion in CBCT image reconstruction, images of 4D NURBS-based cardiac-torso (NCAT) phantom data from Segars (SEGARS, 2001) was produced. The NCAT phantom provides a realistic and flexible model of the human anatomy and physiology.

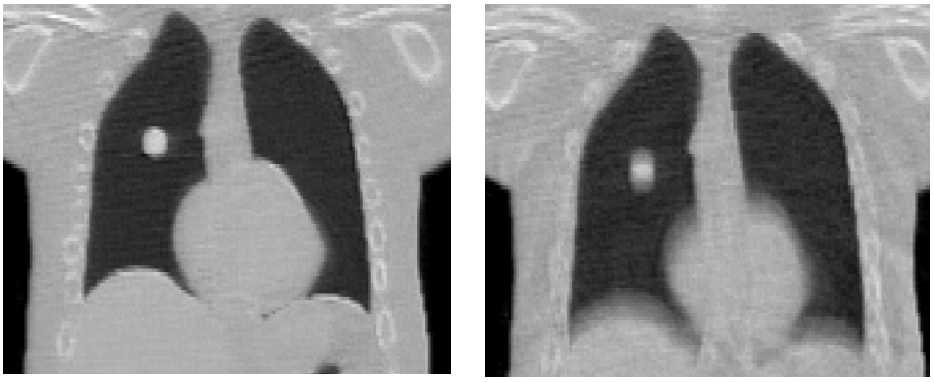

(a) (b)

Figure 1-1 CBCT reconstructed images (a) with no motion, and (b) with respiratory movement.

Figure 1-1 shows the CBCT reconstructed images of the NCAT phantom with a synthetic tumour lesion in the right lung, with and without the introduction of respiratory motion. Both of these images were reconstructed using ART algorithm, which was experimentally tested with CBCT data (QIU et al., 2010). These images show that the boundary of the tumour in figure 1-1(b) was blurred as a result of the motion. To reduce the motion artefacts in CBCT reconstruction, motion correction and motion compensation techniques have been investigated in the last decade

(SONKE et al., 2005, RIT et al., 2005, PURDIE et al., 2006, RIT et al., 2009b, BODA-HEGGEMANN et al., 2011, MARCHANT et al., 2011, MARCHANT et al., 2012).

There were several methods that have been investigated for improving the respiratory artefacts in CBCT imaging. It is a challenging problem, since a reliable technique to compensate for breathing movement is required for enhancing the accuracy of tumour localisation. There are various approaches used to detect and estimate the respiratory motion (LU et al., 2007, EHRHARDT et al., 2007, RIT et al., 2009b). For example, the surrogate devices can be used to detect the movement of the chest wall (VEDAM et al., 2003). However, the motion can only then be estimated in the anteroposterior (AP) direction, which is not appropriate in case of lung cancer, according to the greatest respiratory motion for lung cancer is in the superoinferior (SI) direction (SEPPENWOOLDE et al., 2002, JIANG et al., 2003b). This discrepancy could not be detected by external motion detection devices.

A combination of external measurements with biomechanical modelling, detecting the movement of the diaphragm, has not yet been successfully achieved. Alternatively, metallic seeds can be implanted and the respiratory motion of each patient retrieved (SHIRATO et al., 2000, BECKER et al., 2010, ALI et al., 2011, MARCHANT et al., 2012). However, this technique seems not to be preferred, due to the invasiveness of the technique that could result in a potential discomfort or complication. Another approach is the direct extraction of the motion achieve from 2D CBCT projections (MARCHANT et al., 2008); in this way, the displacement of the diaphragm can be tracked. However the diaphragm displacement is angle-dependent, for example, the lung may be obscured behind bones in many of the projections; hence the motion model deduced from the full set of projections may be inaccurate. Therefore, the problem of patient-specific bio-mechanical modelling of thorax movement is still a challenging research question. Finally, motion-compensated CBCT can be implemented by using a motion model, which was collected during the treatment planning process. However, the respiration patterns of patients who have lesions in their chest cavity may be varied over a period of time,

and fixing procedure prior to motion model, also can cause target mispositioning on different days of treatment.

There are many image reconstruction algorithms used in CBCT imaging. The algorithm used in commercial CBCT units is the Feldkamp, Davis and Kress (FDK) algorithm which based on filtered-back projection (FBP) (FELDKAMP et al., 1984). This is a convolution-based direct 3D reconstruction using 2D projection data from different angles. FDK was first developed for material testing in the Ford Motors by using a micro-focus X-ray source with an electronic image intensifier system. The most important concept of FDK method is weighting the projection data for the cone-angle. Feldkamp et al showed that this method produces blurring effects in the axial direction, especially for a large cone angle. The larger angle was, the greater blurring was. Compared to unmodified fan-beam reconstruction using FBP, FDK produced lesser distortion. In 2000, FDK was used in an initial investigation of using CBCT for medical imaging in radiotherapy (JAFFRAY and SIEWERDSEN, 2000).

A limitation of FDK is that the algorithm does not allow to implement the image data between the reconstruction process while algebraic iterative methods can do. Moreover, FDK, based on FBP, can produce artefacts when limited data is used. Therefore, the algebraic iterative algorithms were of interest for compensating the motion by updating the motion information into each successive iteration during the reconstruction process. Simultaneous Algebraic Reconstruction Technique (SART), one of algebraic reconstruction methods, has been studied for motion-compensated CBCT (RIT et al., 2009a).

In this thesis, the electrical impedance tomography (EIT) is one of the interested system, because it is a rapid imaging system, which can capture images of moving organs. EIT is a technique for imaging the impedance distribution within electrically conductive objects using surface electrical measurements. Typically, conducting electrodes are attached to the surface of the subject and small alternating currents are applied to some or all of the electrodes, and the resulting electrical potentials are

measured. EIT has been developed for clinical applications such as imaging of lungs, breast and brain (HOLDER, 1992, DIJKSTRA et al., 1993, TOWERS et al., 2000, FRERICHS, 2000, ZOU and GUO, 2003). For lung imaging, EIT can measures the conductivity of the air in lungs which has large contrast compared to the other tissues in the thorax. Real time images can be provided by EIT systems for applications in the continuous monitoring of cardiac and respiratory functions (EDIC et al., 1995). Recently, a growing number of clinical studies has been performed by using EIT for lung monitoring (BAYFORD, 2006, HAHN et al., 2006, BRUNNER et al., 2007, HAHN et al., 2008, CHEN et al., 2009b, NEBUYA et al., 2010, BORSIC et al., 2010). EIT has already been used in critical care units for lung monitoring (BODENSTEIN et al., 2009, BIKKER et al., 2010).

Furthermore, the EIT electrodes are typically radiopaque materials, which could be seen as metal artefacts on a CBCT image. These artefacts possibly superimpose some important organs or lesions on the CBCT image. Hence, to achieve the CBCT-EIT combination, radiolucent EIT electrodes should be used in this combination. KAO et al developed the radiolucent electrode array for the combination of EIT and mammography (KAO et al., 2007). The electrode was not appeared on the radiographic images but some parts of this array were shown. However, CBCT might more sensitive to this electrode array due to a full rotational scan. Therefore, it needs to be further studies.

The main aim of this study is to develop a combination of a motion-compensated CBCT and EIT in a software based phantom, by using EIT imaging as a motion monitoring system. The proposed approach takes advantages of the high temporal resolution of EIT images for detecting the motion. Then, the motion information extracted from the EIT images was incorporated into an iterative CBCT image reconstruction algorithm as shown in figure 1-1. This proposed method is a prospective motion compensation technique which taking EIT images at the same time as acquiring CBCT data. In real clinical settings, it would be more beneficial to develop a patient specific model for the EIT imaging that can be done with diagnostic CT images. It could be potentially useful to use EIT in adaptive

radiotherapy, by having the EIT imaging during the radiotherapy. However, these issues are beyond the scope of the thesis. This thesis is focused on the theoretical and experimental validations of the CBCT-EIT combination.

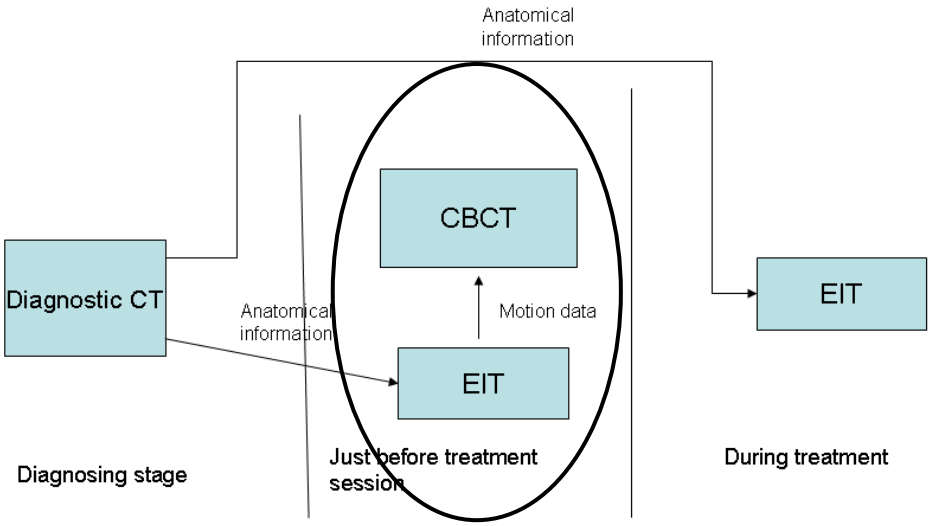

Figure 1-2 Possible use of the EIT system in CBCT system.

The thesis is organised as follows: chapter 2 describes a brief introduction to the basic principles of the CBCT imaging system and focuses on a literature review of motion-compensated CBCT, which involves the respiration-induced target movement. Chapter 3 begins by laying out the iterative image reconstruction as a tool for the motion-compensated CBCT and looks at image quality assessment. Chapter 4 introduces EIT imaging as well as a simple motion extraction technique. Chapter 5 is dedicated to the study of the feasibility of the developed motion-compensated CBCT with full data reconstruction using the Algebraic Reconstruction Technique (ART). Chapter 6 shows the study of the motion compensation with limited data reconstruction (one-fourth data set) using ART, Simultaneous ART (SART), Ordered-Subset SART (OS-SART) and Conjugate Gradient Least Squares (CGLS). Chapter 7 deals with the dual modality of CBCT-EIT, in which the EIT images are used to generate the motion information. The last chapter presents the conclusions and future works.

Chapter 2
CBCT Guided Radiotherapy

CT was first introduced to radiotherapy as a simulator for treatment planning purposes (WEBB et al., 1977). In 1990s, 3D imaging became important in medical applications. The advancement of 3D imaging in treatment planning was typically need to analyse 30 – 60 slices of the CT images. The scanning time of 3D CT simulation could be at least 240 s. To reduce scanning times, the acquisition of multiple slices in single rotation of an X-ray source is required. The scanning time could be reduced to 3-6 s for 48 cm scanning length with 8-slice scanner (AIRD and CONWAY, 2002). Then, CT is not only used for treatment simulation and planning, but also used for treatment verification in treatment rooms. The studies of using CT in IGRT were carried out by many researches (AOKI et al., 1987, DAWSON and JAFFRAY, 2007). CBCT is one of the imaging systems, which is able to achieve multiple slices in a single scan by using a multiple row X-ray detector with a wide angle X-ray beam.

A CBCT system produces a volumetric 3D image, which consists of an X-ray source and a large area of flat panel detector. Feldkamp, Davis and Kress (FDK) algorithm is used in a commercial CBCT unit which was first developed in the Ford Motors for material testing(FELDKAMP et al., 1984). In 2000, FDK algorithm was introduced into a prototype CBCT by Jaffray (JAFFRAY and SIEWERDSEN, 2000).

The limitation of the radiotherapy for thoracic and abdominal tumours is the changing and moving of tumours, during and between the radio-treatment sessions.

This leads to inaccuracy of radiation delivery to the target area. Slow rotating CBCT has been introduced to IGRT for verifying the position of the target before each treatment session, to achieve the planned radiation dose (JAFFRAY et al., 2002). However, breathing-induced motion during the CBCT scanning, causes blurring artefacts and results in misalignments of the target tissues. This chapter reviews basic principles of CT and CBCT imaging. Additionally, this chapter extend to the literatures concerning about the respiratory movement in radiotherapy, motion correction and motion compensation in CBCT.

2.1 Basic principles of CT

A gamma ray source was first used in Hounsfield's experiment and emits monochromatic rays (ISHERWOOD, 2005). When the monochromatic rays penetrate through a homogeneous object as shown in figure 2-1(a), the ray attenuation can be explained by Lambert-Beer law (SEERAM, 2000, BUZUG, 2008) as follows

$$I = I_0 \cdot e^{-\mu x} \tag{2-1}$$

where I_0 and I are an incident photon intensity and an intensity of photons after having passed an object with thickness x. The purpose of CT is to determine the linear attenuation coefficient μ of the object and convert those values to a gray-scale image. The attenuation coefficient is measured in units of m^{-1}.

Unfortunately, body organs which photons pass through are not homogeneous tissues as shown in figure 2-1(b). Equation (2-1) must be modified to

$$I = I_0 e^{-(\mu_1+\mu_2+\mu_3+...+\mu_n)x} \tag{2-2}$$

Moreover, the human organs are not only inhomogeneous tissues but also different in the tissue thicknesses as illustrated in figure 2-1(c). In this model, the numbers of photons are calculated by

$$I = I_0 \cdot e^{-(\mu_1 x_1 + \mu_2 x_2 + \mu_3 x_3 + \ldots + \mu_n x_n)} \tag{2-3}$$

then,

$$I = I_0 \cdot e^{-\sum_{i=1}^{n} \mu_i x_i} \tag{2-4}$$

and,

$$I = I_0 \cdot e^{-\int_0^x \mu x dx} \quad . \tag{2-5}$$

For clinical CT scanners, an X-ray source produce an X-ray beam with a wide range of photon energies (polychromatic radiation). The attenuation values depend on the photon energy *E*, which could not be calculated by equation (2-5). Therefore, the equation (2-5) can be extended to

$$I = \int_0^{E_{\max}} I_0(E) \cdot e^{-\sum_i^n \mu_i(E) x_i} dE \tag{2-6}$$

then,

$$I = \int_o^{E_{\max}} I_0(E) \cdot e^{-\int_0^x \mu(E) x dx} dE \quad . \tag{2-7}$$

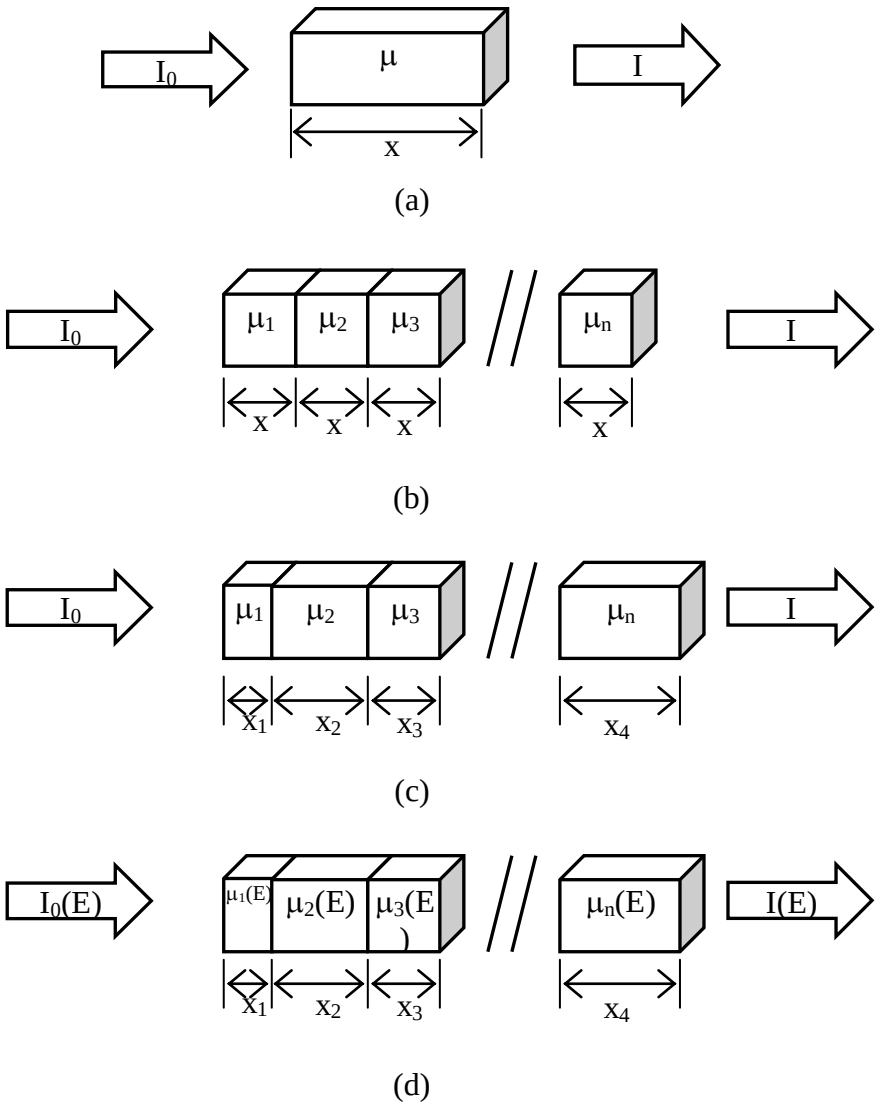

Figure 2-1 (a) Attenuation of monochromatic rays running through a homogenous object; (b) Attenuation of monochromatic rays running through an inhomogeneous object with all the same thickness; and (c) Attenuation of monochromatic rays running through an inhomogeneous object with different thicknesses; (d) Attenuation of polychromatic rays running through an inhomogeneous object with different thicknesses.

The summation of the attenuations in the particular X-ray path can be defined as

$$\ln \frac{I_0(E)}{I} = \int_0^x \mu(E) x dx \,. \tag{2-8}$$

The natural logarithm of the ratio of the incident photons and the outgoing photons ($\ln \frac{I_0}{I}$) is known as ray sums. A set of ray sums at a particular angle is a projection as shown in figure 2-2(a).

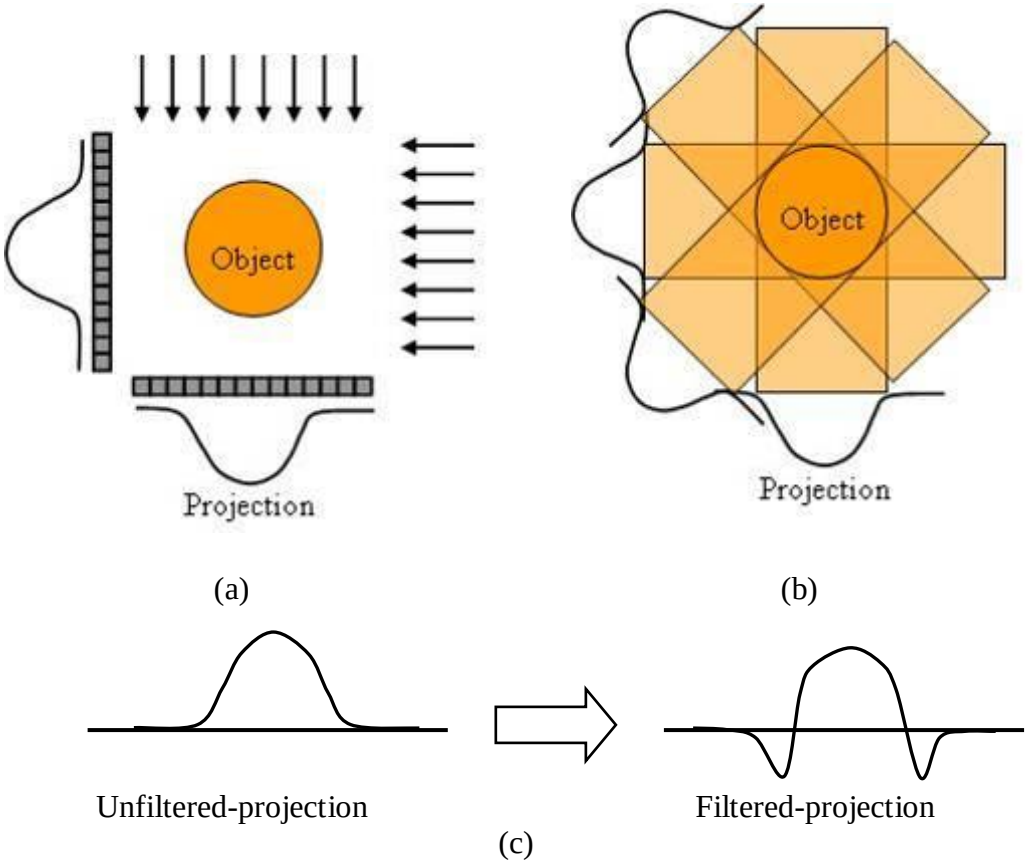

Figure 2-2 (a) X-ray projections, (b) back projection reconstruction, and (c) unfiltered-projection and filtered-projection.

A back projection algorithm is typically used for calculating the linear attenuation coefficients μ in an image matrix of an object by projecting all projections backwards in the direction of each raypath. In case of small numbers of projections, the reconstructed image would show a spiky artefact (figure 2-2(b)). This is also known as a star artefact. On the other hand, blurring around the edges of the images would be developed from spikiness with more projections used. It shows as top hat

shapes for point spread function which can be corrected by convolution with biphaic convolution kernel.

In order to remove this artefact, a mathematical filtering process can be used. Digital filters are implemented to raw projection data and the results, called filtered projection, is back-projected to the image matrix (FARR and ALLISY-ROBERTS, 1998, SEERAM, 2000).

CT imaging system can be classified into generations one to five, multi-slice CT (MSCT) and CBCT. Before the last decade, most of the diagnostic CT used in clinics was the third generation. This generation is based on parallel-fan beam X-ray coupled with a single-row curved detector. The acquisition technique of this generation is slice by slice scanning. The X-ray tube and detector are rotated as one around the scanned part of the body, which the stationary on the couch. Then the couch and patient are indexed to the next position of the scanning. The MSCT has become more widely used for diagnostic CT imaging nowadays. This was developed from the third generation, which has narrow-angle cone-beam geometry with a multiple-row curved detector. MSCT still uses couch indexing while the X-ray tube and detector are continuously rotated during scanning (SEERAM, 2000).

2.2 Basic principles of CBCT

Cone beam computed tomography (CBCT) was first developed in 2000 (JAFFRAY and SIEWERDSEN, 2000) using a square flat panel, amorphous silicon imager to detect radiation indirectly (ANTONUK et al., 1998). This allowed truly wide-angle CBCT to be developed for radiation therapy . Coupling of an X-ray tube and this flat panel detector allows to acquire a set of 2-dimensional projection data in single rotation. An volumetric image is reconstructed from these 2-dimensional projection data. A graphical representation of CBCT with an X-ray tube and a flat panel detector is shown in figure 2-3.

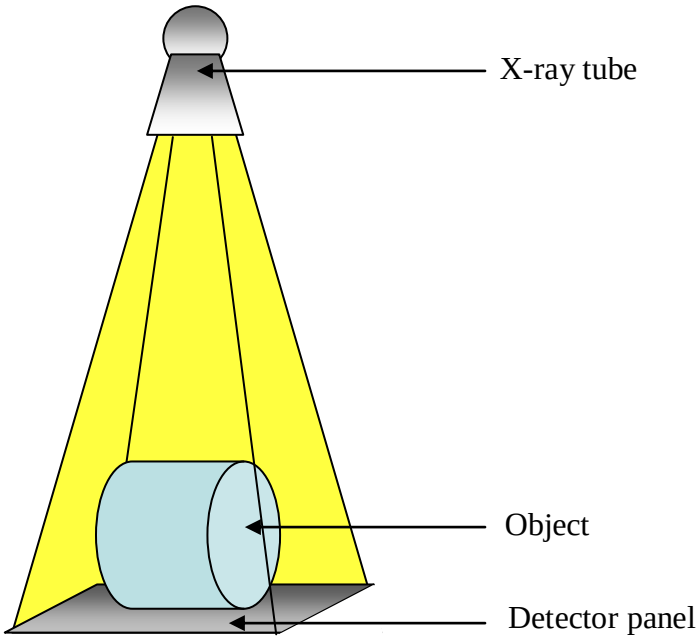

Figure 2-3 Graphical representation of CBCT with an X-ray tube and a flat panel detector.

A detector of CBCT is based on Antonuk's detector. It consists of two main components: a scintillation layer and an amorphous silicon matrix. The face of the detector, which the X-rays hit, is the scintillation material layer. This material converts the energy of X-ray photons to the intensity of light and, then, they are passed directly to the amorphous silicon matrix which convert the light to signal-intensity charges. Typical scintillation materials is rare earth materials such as Caesium Iodide (CsI) or Gadolinium Oxysulphide (Ga_2O_2S). The intensity of the signal is a proportional to the energy of the X-ray photons (ANTONUK et al., 1998, BUZUG, 2008). Figure 2-4 shows the CBCT system that is used in a clinical setting. It includes CBCT and Linac for radiotherapy.

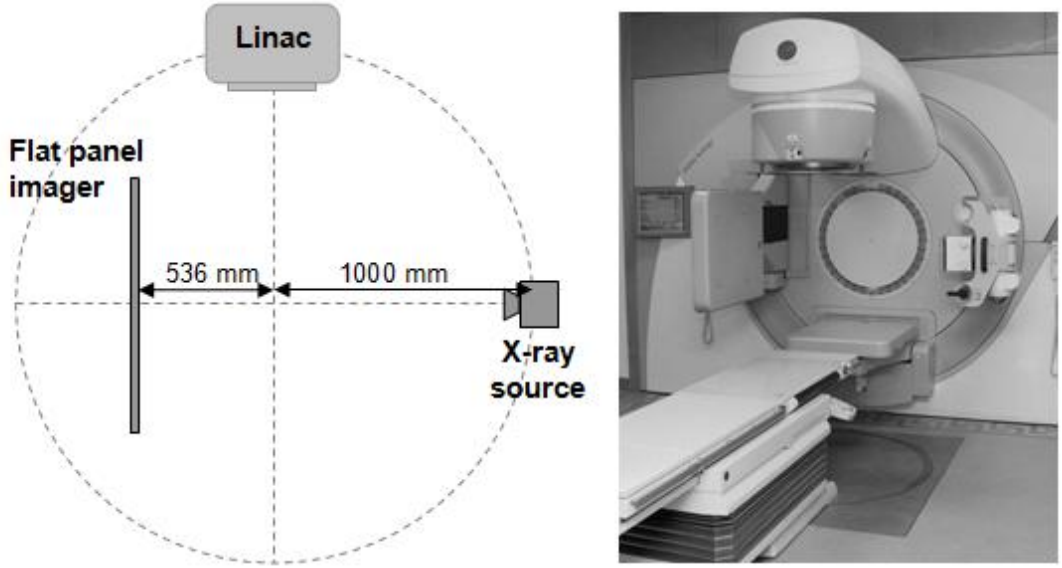

Figure 2-4 A CBCT system from Christie hospital in Manchester (QIU et al., 2010).

2.3 Respiratory movement in radiotherapy

Respiratory-induced tumour motion in radiotherapy can be divided into two types: intra-fractional motion and inter-fractional motion. The intra-fractional motion are changes in patient or target position, during the treatment session. For inter-fractional motion, there is a variation of patient position between treatment sessions. The causes of this motion are patient set up changes and patient anatomy changes.

Respiratory movement during the radiation treatment has been investigated by many researchers. In 2002, Seppenwoolde et al. studied the 3D motion of lung cancers in 20 patients during radiotherapy (SEPPENWOOLDE et al., 2002). The results showed that the average of amplitude of tumour movement due to respiration was mainly in the superoinferior (SI) direction about 12±2 mm for tumours located in lower lobe and not attached to rigid structures such as the chest wall. On the other hand, the tumour motion was very small in the anteroposterior (AP) and the left-right (LR) directions. The duration of exhale was longer than the duration of inhale, so that the time-average tumour position was close to the position of exhale.

Jiang et al. performed the retrospective study of lung tumour movement of 30 patients detected by two X-ray imaging systems. The results confirmed the study of Seppenwoolde et al. that the largest motion was in the SI direction for most patients. The average tumour displacements were 10.42 ±7.09SD mm and 8.64±6.38SD mm for inhalation and exhalation, respectively. The maximum displacement was 29.49 mm for inhalation (JIANG et al., 2003).

Mageras et al. investigated lung tumour motion by using respiratory correlated CT of helical single slice and 4-slice CT (MAGERAS et al., 2004). The retrospective image sorting was done into different respiratory phases recorded while performing CT scanning. The inter-fractional gross tumour volume (GTV) variation was measured by calculation of the ratio of GTV and GTV displacement, which was estimated from the diaphragm displacement. The GTV displacement was mainly in the SI direction. This research suggested that respiratory correlated CT was able to estimate inter-fractional variability.

Breathing variations in infra- fractional and inter-fractional treatments of lung cancer were investigated by Juhler et al. External markers were used for the monitoring of chest wall movement. The variations of both infra-fraction and inter-fraction over treatment course were 5.5 – 26.7 mm (15.2 mm median). The inter-fractional variations in breathing were up to ten times larger than the infra-fractional variations (JUHLER et al., 2007).

Chen et al. reported that the centre of a lung tumour is shifted over the period of fractionated radiotherapy (CHEN et al., 2009). During the treatment session, the size of the tumour has shrunk markedly. The imaging of the target can be used to verify and compensate for the size changes.

2.4 Motion correction in CBCT

The CBCT was first investigated for IGRT by Jaffray et al. in 2002, who studied the performance of CBCT combined with Linac (JAFFRAY et al., 2002). A kilo-voltage

X-ray source was mounted on a rotating gantry of Linac and flat-panel X-ray detector placed opposite to the X-ray source. This demonstrated that high spatial resolution (submillimeter resolution) was achieved for high contrast objects in the coronal and sagittal planes. However, the reconstructed image was affected by loss of details, misregistration, and streak artefacts.

Nevertheless, motion remains a considerable problem due to CBCT being mounted on a slow rotating gantry of the Linac. Many researchers are interested in solving this motion problem. The motion correction techniques can be divided into two methods: motion-correlated CBCT and motion-compensated CBCT.

2.4.1 Motion-correlated CBCT

This method is a retrospective motion correction of respiration-induced motion. The respiratory signal is recorded and used for grouping CBCT projection data into their positions in the respiratory phase. Each group of projections is reconstructed for each phase.

Various techniques for detecting breathing motion by using external monitoring systems in radiotherapy have been studied. Vedam et al. have used a commercial respiratory motion monitoring system, which provides an external motion model for achieving four-dimensional (4D) CT (VEDAM et al., 2003). This motion monitoring is based on an infrared camera tracking system. A phase-based retrospectively sorting technique was used to correct the respiratory motion, in both a motion phantom and a patient experiment. The results demonstrated that the motion artefact in 4D CT image was reduced compared with the 3D CT image.

An alternative method of 4D CT was using tidal lung volume, which is measured by digital spirometry. The tidal lung volume was recorded during a free-breathing multi-slice CT (MSCT) scan for three patients with lung tumour. The 4D CT image was achieved by retrospectively sorting the 3D image data into their correlated tidal-

volume bins. The 4D CT images showed relatively small motion artefacts along the diaphragm for the sagittal and coronal images (LOW et al., 2003).

In addition, the respiratory motion model extracted from CBCT projection data has been studied by Sonke et al. and Rit et al (SONKE et al., 2005, RIT et al., 2005). Sonke et al. have developed an alternative respiratory-corrected CBCT (4D CBCT) by retrospectively sorting projection data into each respiratory phase. The one-dimensional (1D) respiratory model in the SI direction was directly extracted from 2D projection data based on detection of the motion of the diaphragm. The results of both phantom and patient studies showed that the motion artefact was significantly reduced in 4D CBCT, compared to 3D CBCT. It suggested that this respiratory-corrected CBCT technique can be used for verifying the patient position prior to the treatment. The main advantage of this technique is that there is no need for external respiratory movement monitoring devices. However, this involved tracking the displacement of the diaphragm, which might be a different part of the diaphragm in different angles of gantry. It may be less accurate because the method tracks the position of the diaphragm, not exactly the position of tumour.

The motion extraction technique of Sonke et al., which published in 2005, was evaluated for the respiratory-induced tumour motion error in Sonke et al., 2008 (SONKE et al., 2008). The shape and mean position of lung tumours during a radiation treatment course has been investigated in 56 patients. The patients were imaged by the CBCT with the respiratory motion correction. The results showed that the shape of tumours had a small change and the largest displacements of the inter-fraction, mean tumour displacement was 3.9 mm in the SI direction. The displacement was very small when compared with uncompensated CBCT. This results suggested that respiratory-corrected CBCT has a high level of accuracy in monitoring the changing of tumour shape and position, and it can be used for daily imaging to register the soft-tissue target in lung cancer.

Rit et al. were also interested in respiratory motion extraction from the CBCT projection data (RIT et al., 2005). Points of interest were considered as a uniform set

of points of the pixels of the CBCT projections. Typically, 100,000 to 200,000 points were used in this study. The motion extraction was tracking the points of interest from projection to projection over the acquisition time. The results showed that the extracted motion model was 96.4 percent correlated with the reference model. This study assumed that the motion seen during treatment planning can be modelled and remains applicable later during treatment CBCT. It uses rigid registration (of points of interest in defined regions) between planning CT and treatment CBCT reconstructions i.e. no corresponding points were actually identified. In 2009, he made the same assumption that motion during the planning and the treatment are one and the same, except he uses the model to compute the motion phase of each X-ray projection image. FDK back projection is then implemented for wrapped acquisition lines (RIT et al., 2009b).

Purdie et al. used the respiratory-corrected CBCT technique developed by Sonke et al., which was published in 2005, in respiratory-corrected CBCT study of stereotactic body radiotherapy (SBRT) of lung tumours (PURDIE et al., 2006). The 4D CBCT was acquired by phase-based sorting of 2D projection data. The motion model was tracked from the position of the diaphragm. The 4D CBCT image was compared with the 4DCT image. The results suggested that the respiratory-corrected CBCT might not be suitable for short course treatment techniques such as the SBRT.

2.4.2 Motion-compensated CBCT

All published works mentioned above involve the retrospective sorting for respiratory-corrected CBCT. Full CBCT projection data are acquired during scanning and then motion-correction is done after scanning. Recent research has been extended to prospective motion-correction technique.

On-the-fly motion-compensated CBCT has been studied by Rit et al. (RIT et al., 2009b). The study used an a priori model of the respiratory motion, which was measured by an external motion detection system acquired during a CT planning scan. This model was used as a reference motion model. During the CBCT scan, the

model was compared with the breathing signal tracked from the position of the diaphragm in the 2D CBCT projection data (RIT et al., 2005). This respiratory motion model was used to compensate during CBCT reconstruction. It was studied for simulated data, phantom study and patient data. Reducing motion artefacts could be found on motion-compensated CBCT images for all experiments. The main benefit of this study is predominantly in the "on-the-fly motion compensation". However, they suggested that the performance of a priori motion model might need to be improved because of the inaccuracy of a priori motion model, which was observed on patient data in experiments. This motivates the study of using a motion model extracted while collecting the projection data to compensate for motion artefacts.

Chapter 3

Iterative Image Reconstruction and Image Quality Assessment

There are various image reconstruction methods in the volumetric X-ray CT in medical applications. The Feldkamp, Davis and Kress (FDK) algorithm (FELDKAMP et al., 1984) is typically used in clinical CBCT units. This algorithm is a direct method of image reconstruction, which implements the filtered-back projection (FBP) for the CBCT. The FDK was developed for material testing in the Ford Motors. There are a number of limitations in the FDK based method, one of which is data insufficiency. Based on a single circular scan geometry of CBCT, the FDK does not satisfy Tuy's condition which requires X-ray trajectory intersecting all imaging planes passing through an object (TUY, 1983). Hence, reconstruction errors in the axial direction outside the mid-plane could be seen especially for a large cone angle. Additionally, the FDK also introduces object geometry distortion and blurring effects of slices parallel to and away from the mid-plane when a large cone angle is used. Moreover, this thesis also study a limited projection data reconstruction, which the FDK, FBP based method, could produce artefacts when fewer projection data are used (CHLEWICKI et al., 2001).

To overcome the FDK shortcoming, many image reconstruction algorithms have been studied for CB reconstruction (MUELLER et al., 1999, CHLEWICKI et al., 2001, YU et al., 2006, RIT et al., 2009a, HANSIS and LINGXIONG, 2011, JIA et al., 2011). Among these techniques, algebraic iterative approaches are expected to provide higher image quality for motion-compensated CBCT (RIT et al., 2009a).

The algebraic reconstruction technique (ART) is one of the reconstruction algorithm techniques that has been studied for medical imaging systems (GORDON et al., 1970). It is a simple algebraic iterative reconstruction method, which uses Kaczmarz's method (NATTERER, 2001), in effect, to solve a weighted least-squares problem. This method is based on ray-by-ray updates (KAK and SLANEY, 1999). The ART has been studied for imaging systems such CBCT, positron emission tomography (PET) (KINAHAN et al., 1994), and single photon emission computed tomography (SPECT) (ROS et al., 1996). The simultaneous ART (SART) was introduced by Andersen and Kak (ANDERSEN and KAK, 1984) and simultaneously updates the solution using all rays at once. The SART was investigated for motion-compensated CBCT reconstruction comparing to adapted FDK by Rit et al. (RIT et al., 2009a). Adapted FDK showed streak artefacts resulting from motion whilst SART provided better results. However, the reconstruction time when using adapted FDK was significant faster than using SART. Next the ordered-subset SART (OS-SART), projection data is partitioned into blocks, and an iterative update is sequentially calculated for each block (GE and MING, 2004, HUDSON and LARKIN, 1994).

Furthermore, the conjugate gradient least squares (CGLS) has been introduced to CBCT image reconstruction (JIA et al., 2011). The advantages of CGLS has over ART and SART are a faster in convergence rate and the possibility of parallel computation. The CGLS algorithm can provide an opportunity for improving the imaging quality of limited data which is an issue for FDK. Hence, CGLS was also investigated for the motion-compensated CBCT reconstruction in this study.

Additionally, image quality measures are introduced in this chapter so that the effectiveness of proposed methods can be evaluated.

3.1 Algebraic reconstruction methods: ART, SART, and OS-SART

An iterative reconstruction algorithm is a technique that uses the differences between the measured data and the calculated data to update an image. In this section, the approaches and definitions for SART and OS-SART in Jiang and Wang are described (JIANG and WANG, 2003). For example, an image $\mathbf{x}$ is required which solves

$$\mathbf{Ax} = \mathbf{b}, \tag{3-1}$$

where $\mathbf{x} \in \Re^N$ is the image value for N cells and $\mathbf{b} \in \Re^M$ is measured data from M measurements. Each element $\mathbf{A}_{mn}$ of the weight matrix makes $\mathbf{A} \in \Re^{M \times N}$ is the length of intersection of the m^{th} ray with the n^{th} cell, for example $\tilde{\mathbf{a}}_1$ is the weight matrix of the intersection between 1^{st} ray with a 2-by-2 image matrix as illustrated in figure 3-1.

For iterative reconstruction, equation (3-1) can be solved by

$$\mathbf{x}^{(k+1)} = \mathbf{x}^{(k)} + \lambda_n \delta\mathbf{x}^{(k)}, \tag{3-2}$$

where $\delta\mathbf{x}^{(k)}$ is an update, λ_n is a relaxation parameter, k is the iteration index and n is the cycle index (one cycle is defined as all available dataset is used in one iteration), let

$$\mathbf{x} = \begin{bmatrix} x_1 \\ x_2 \\ x_3 \\ \vdots \\ x_N \end{bmatrix} \in \Re^N. \tag{3-3}$$

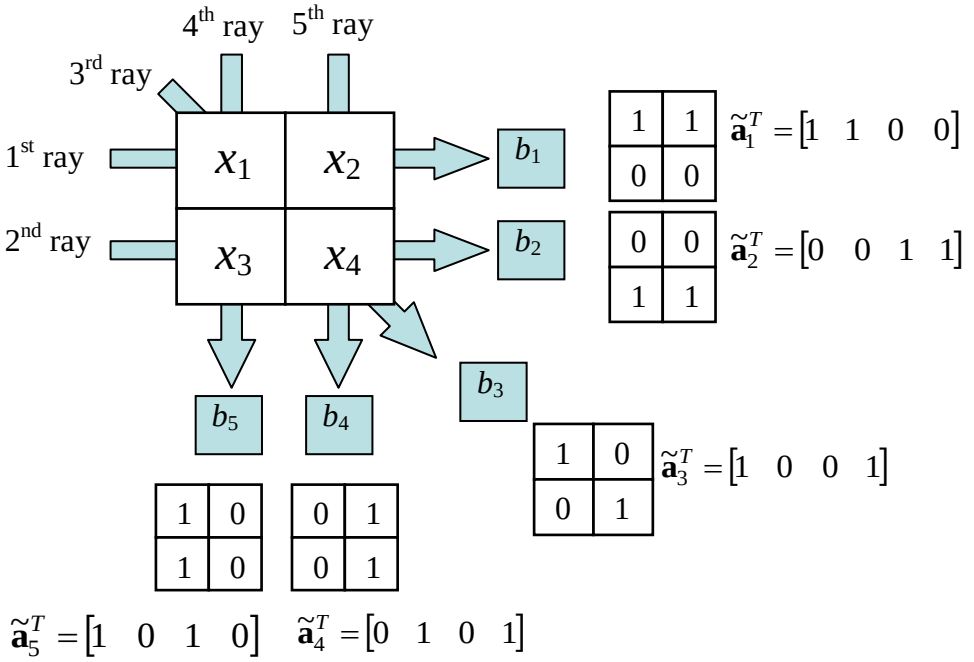

Figure 3-1 A simplified illustration of five rays passing through a 2-by-2 image matrix (here, $M = 5, N = 4$, $\mathbf{A} \in \Re^{5\times 4}$).

Usually, the initial image values are defined as all zero, then $\mathbf{x}^{(0)} = \mathbf{0}$.

Also let

$$\mathbf{b} = \begin{bmatrix} b_1 \\ b_2 \\ b_3 \\ \vdots \\ b_M \end{bmatrix} \in \Re^{M\times 1}, \tag{3-4}$$

and

$$\mathbf{A} = \begin{bmatrix} \tilde{\mathbf{a}}_1^T \\ \tilde{\mathbf{a}}_2^T \\ \tilde{\mathbf{a}}_3^T \\ \vdots \\ \tilde{\mathbf{a}}_M^T \end{bmatrix} \in \Re^{M \times N} . \tag{3-5}$$

ART updates row-by-row so

$$\mathbf{x}^{(k+1)} = \mathbf{x}^{(k)} + \lambda_n \frac{1}{\tilde{\mathbf{a}}_i^T \tilde{\mathbf{a}}_i} \left(b_i - \tilde{\mathbf{a}}_i^T \mathbf{x}^{(k)} \right) \tilde{\mathbf{a}}_i , \tag{3-6}$$

where i is the row index, and the relaxation parameter λ_n is changed by the cycle index n.

SART iteratively updates for the whole image as

$$\mathbf{x}^{(k+1)} = \mathbf{x}^{(k)} + \lambda_n \mathbf{V}^{-1} \mathbf{A}^T \mathbf{W} \left(\mathbf{b} - \mathbf{A}\mathbf{x}^{(k)} \right), \tag{3-7}$$

where $\mathbf{V}$ is diagonal with j^{th} diagonal element

$$\mathbf{V}_{jj} = \sum_{i=1}^{M} \left| \mathbf{A}_{ij} \right|, \tag{3-8}$$

and $\mathbf{W}$ is diagonal and with i^{th} diagonal element

$$\mathbf{W}_{ii} = \frac{1}{\sum_{j=1}^{N} \left| \mathbf{A}_{ij} \right|}, \tag{3-9}$$

and $\mathbf{A}_{ij}$ is the $(i, j)^{th}$ element of $\mathbf{A}$. A sample calculation of ART and SART for a 2-by-2 matrix is demonstrated in Appendix.

However, **b** can also be divided into *B* blocks where

$$\mathbf{b} = \begin{bmatrix} \mathbf{b}_1 \\ \mathbf{b}_2 \\ \mathbf{b}_3 \\ \vdots \\ \mathbf{b}_B \end{bmatrix} \in \Re^M \text{ , and } \mathbf{b}_\beta \in \Re^{M_\beta} \text{ , } \beta \in [1, B], \tag{3-10}$$

and $M = \sum_{\beta=1}^{B} M_\beta$. Similarly **A** can be divided into *B* blocks where

$$\mathbf{A} = \begin{bmatrix} \mathbf{A}_1 \\ \mathbf{A}_2 \\ \mathbf{A}_3 \\ \vdots \\ \mathbf{A}_B \end{bmatrix} \in \Re^{M \times N} \text{, and } \mathbf{A}_\beta \in \Re^{M_\beta \times N} . \tag{3-11}$$

The reconstruction method of divided blocks is so-called "OS-SART" which updates an image block-by-block using,

$$\mathbf{x}^{(k+1)} = \mathbf{x}^{(k)} + \lambda_n \mathbf{V}^{-1} \mathbf{A}_\beta{}^T \mathbf{W}_\beta \left(\mathbf{b}_\beta - \mathbf{A}_\beta \mathbf{x}^{(k)} \right), \tag{3-12}$$

where $\mathbf{W}_\beta$ is diagonal with i^{th} diagonal element

$$\left[W_\beta \right]_{ii} = \frac{1}{\sum_{j=1}^{N} \left| A_{ij}(\beta) \right|} . \tag{3-13}$$

To counteract the potential divergence of reconstruction after some cycles, in this study a relaxation parameter λ_n is scheduled corresponding to the cycle index *n* $(n \geq 1)$(PENGPAN et al., 2011) as

$$\lambda_n = sf \times \frac{1}{n^{\alpha}} \text{ , where } 0 < \alpha \leq 1 \tag{3-14}$$

and sf is the scaling factor. Denote that α is a rate of change of the relaxation parameter. This guarantees the convergence of the algorithms (JIANG and WANG, 2003).

3.2 Conjugate Gradient Least Squares (CGLS) algorithm

The CGLS is an iterative solution used in large sparse least squares problem of **Ax**=**b**. The weight matrix ($\mathbf{A} \in \Re^{M \times N}$) is created using a forward projection programme. The matrix **A** is a combination of the sub-matrix for each projection. In the case where the matrix **A** is positive-definite, the matrix $\mathbf{A}^{\mathrm{T}}\mathbf{A}$ is positive-definite for any matrix **A**. In the CBCT imaging system used in this study (256^3 voxels, 512^2 detectors), the matrix **A** is very sparse and only about 0.4% (for 2D reconstruction) and 0.0018% (for 3D reconstruction) of entries of matrix **A** are non-zero. The iterative method is terminated at i steps for $k = 0, 1, 2, \ldots, i$. The residual ($\mathbf{r}^k$) at each step is computed by (HESTENES and STIEFEL, 1952, BJORCK, 1996, HANSEN, 1998)

$$\mathbf{r}^k = \mathbf{b} - \mathbf{A}\mathbf{x}^k . \tag{3-15}$$

Starting with an initial approximation ($\mathbf{x}^0$), then, $\mathbf{r}^0 = \mathbf{b} - \mathbf{A}\mathbf{x}^0$, $\mathbf{p}^0 = \mathbf{A}^T\mathbf{r}^0$

and
$$\psi^k = \frac{\left\| \mathbf{A}^T\mathbf{r}^k \right\|^2}{\left\| \mathbf{A}\mathbf{p}^k \right\|^2}, \tag{3-16}$$

$$\mathbf{x}^{(k+1)} = \mathbf{x}^k + \psi^k \mathbf{p}^k , \tag{3-17}$$

$$\mathbf{r}^{(k+1)} = \mathbf{r}^k - \psi^k \mathbf{A}\mathbf{p}^k , \tag{3-18}$$

$$\beta^k = \frac{\left\|\mathbf{A}^T\mathbf{r}^{k+1}\right\|^2}{\left\|\mathbf{A}^T\mathbf{r}^k\right\|^2} \quad , \tag{3-19}$$

$$\mathbf{p}^{k+1} = \mathbf{A}^T\mathbf{r}^{k+1} + \beta^k\mathbf{p}^k \, . \tag{3-20}$$

Normally, an initial approximation is $\mathbf{x}^0 = 0$, then $\mathbf{r}^0 = \mathbf{b}$ and $\mathbf{p}^0 = \mathbf{A}^T\mathbf{b}$ where **p** is conjugate vectors. In the case of the residual **r** being zero, it implies that the problem is solved. Otherwise, if the residual **r** is non-zero, the desired solution for $\mathbf{r}^k$ to be minimised , which can be monitored by the L2 norm of the $\mathbf{r}^k$ for each iteration. This can be achieved by updating the residual **r** into the problem iteratively.

Moreover, regularised CGLS was also studied here for ill-posed problems. Generalised Tikhonov regularisation was one of the common use for regularisation. It was used in this study to apply to CGLS as follows:

$$\begin{bmatrix} \mathbf{A} \\ \gamma\mathbf{R} \end{bmatrix}\mathbf{x} = \begin{bmatrix} \mathbf{b} \\ 0 \end{bmatrix} \tag{3-21}$$

where γ is the regularization parameter, **R** is the regularization matrix, which is an identity matrix in this case.

Examples of ART, SART and CGLS calculations are given in Appendix for 2-by-2 matrix.

3.3 Motion-compensated algebraic reconstruction

A motion-compensated CBCT reconstructions using ART, SART, OS-SART and CGLS were investigated in this study. The motion-compensated technique was developed in this study by using a transformation technique the weight matrix **A** which is partitioned into submetrices to be shifted its column appropriately applied according to a motion model to each measured projection (PENGPAN et al., 2011).

This technique implements the motion compensation into a matrix **A** rather than image matrix **x**. The weight matrix $\mathbf{A} \in \Re^{M \times N}$ was partitioned by row into sub-matrices that correspond to each unique projection. The motion compensation was then applied separately for each sub-matrix, by shifting the columns within each sub-matrix according to the motion model for the relevant projection. For this reason, the motion must be estimated for each and every projection. This technique also locked the frame of reference to the moving object rather than the surrounding world.

For OS-SART, the weight matrix **A** was partitioned into B sub-matrices corresponding to each unique projection $\mathbf{A}_\beta \in \Re^{M(\beta) \times N}$, $\beta \in [1, B]$. Then, each $\mathbf{A}_\beta$ was shifted according to the motion model for the relevant projection.

It is noteworthy that the term of "correct motion compensation", the matrix **A** was compensated by applying the same amount of motion (using pixel shift methods) as applied to move the phantom for each projection. For "approximated motion compensation", the matrix **A** was shifted by the incorrect motion models. In chapter 5 and chapter 6, the experiments of the approximated motion compensation is performed by applying a motion model with additive errors to move the phantom but using the motion model with no additive errors to compensate for the motion. In chapter 7, the motion model, used to compensate for the motion, is the motion extracted from EIT images for the dual CBCT-EIT modality.

3.4 Image quality assessment

In subsequent experiments, the results were displayed as reconstructed images, error images (subtracted images between reconstructed images and a true phantom), and one-dimensional (1D) plots and were also analysed in terms of root mean square error (RMSE) of reconstructed images as described below:

3.4.1 Image row plot/ one-dimensional (1D) plots

Principally, a digital image contains a value in each pixel. A simple method to compare the images is image row plot. The image row plot is the plot running through an image at specific x, y or z axis. Therefore, the data (pixel by pixel) between two images, or more, can be compared in the same graph (BAGHAEI et al., 2004, QING-HANG et al., 2005, JOO et al., 2004).

3.4.2 Mean Square Error (MSE) or Root Mean Square Error (RMSE)

This is one of two methods commonly used to evaluate the digital images (GINDI et al., 1993, JIANG et al., 2003a, BAGHAEI et al., 2004, QING-HANG et al., 2005, ŠKERL et al., 2007, QI and CHEN, 2011). The mean square error (MSE) is the calculation of the average across all voxels of the square of the difference value between two images. The root mean square error (RMSE) is the square root of MSE.

$$MSE = \frac{\sum_{i=1}^{N} (x_i - g_i)^2}{N}, \tag{3-22}$$

for ART

$$RMSE = \sqrt{\frac{\sum_{i=1}^{N} (x_i - g_i)^2}{N}}, \tag{3-23}$$

and for SART and OS-SART

$$RMSE = \sqrt{\frac{1}{N} \frac{\sum_{i=1}^{N} (x_i - g_i)^2}{V_{ii}}}, \tag{3-24}$$

where N is the number of voxels, x_i and g_i are respectively the reconstructed and true value in the i^{th} cell.

Additionally, for demonstrating the convergence of the reconstruction, equation (3-24) is modified as follows:

$$RMSE = \sqrt{\frac{\sum_{i=1}^{N}\left(x_i^k - x_i^{k'}\right)^2}{N}} \tag{3-25}$$

where x_i^k is the reconstructed value at the k iteration and $x_i^{k'}$ is the reconstructed value at the k' iteration in the i^{th} cell.

Chapter 4
Electrical Impedance Tomography (EIT) and Motion Extraction

Electrical impedance tomography (EIT) is an imaging technique, which produces images of impedance distribution within electrically conductive objects from surface electrical measurements. Typically, the conducting electrodes are attached to the skin of the subject and small alternating currents are applied to some or all of the electrodes, then the resulting electrical potentials are measured. Bodenstein et al. reported that EIT has been introduced to critical care units for lung monitoring (BODENSTEIN et al., 2009). EIT is able to measure the conductivity of the air in lungs, which has large contrast to the other tissues in the thoracic cavity. EIT has high temporal resolution but low spatial resolution. The advantage of high temporal resolution was proposed to be used as a motion monitoring system in this study.

4.1 EIT image reconstruction

Image reconstruction by EIT can be considered as a nonlinear inverse problem, while CBCT reconstruction is linear inverse problem. An image, or solution, is obtained by repeatedly running a forward model and an inverse solver until convergence is attained. This is briefly described below. In this study, an electrical impedance tomography and diffuse optical tomography reconstruction software (EIDORS) was adapted (POLYDORIDES and LIONHEART, 2002) for the EIT image reconstruction. Motion detection software was developed in this thesis.

To generate EIT images, the forward problem needs to be solved, which can be performed using a finite element method. The forward problem is a problem of estimating the measured EIT data with given conductivity distribution. The image reconstruction problem is an inverse problem and, in attempt to solve the inverse problem, the forward modelling is needed. Under low-frequency assumptions, the full Maxwell's equations can be simplified to the complex-valued Laplace equation:

$$\nabla \cdot (\sigma^* \nabla \mathbf{u}) = 0 \tag{4-1}$$

where **u** is the complex-valued electric potential and σ* is the complex conductivity of the medium ($\sigma^* = \sigma - i\omega\varepsilon_o\varepsilon_r$, for ω is the angular frequency, ε_o and ε_r are the absolute and relative permittivity). The appropriate boundary conditions (complete electrode model) are needed to enable a representative model for the EIT measurement process. In this study, the complete electrode model was used, which took into account both the shunting effect of the electrodes and the contact impedance between the electrodes and surface of object. Utilisation of boundary condition of the EIT model includes

$$u + z_l \sigma \frac{\partial u}{\partial n} = U_l, \ \ r_x \in e_l, l = 1,2,\ldots,L \ , \tag{4-2}$$

$$\int_{e_l} \sigma \frac{\partial u}{\partial n} dS = I_l \ , \ \ r_x \in e_l, l = 1,2,\ldots,L, \tag{4-3}$$

$$\sigma \frac{\partial u}{\partial n} = 0, \ \ r_x \in \partial\Omega / \cup_l^L e_l \ , \tag{4-4}$$

where z_l is the effective contact impedance between the l^{th} electrode and the tissue, n is the outward normal to the surface electrodes, U is the complex-valued voltage, I is the complex-valued current and e_l denotes the electrode l. Here, $r_x \in \partial\Omega / \cup_l^L e_l$ indicates a point on the boundary not under the electrodes.

Due to the complex geometry, the equation (4-1) cannot be solved using analytical method. Therefore, equation (4-1) is the partial differential equation describing the physics of the EIT forward model and that is solved using boundary conditions from equations (4-2, 4-3, and 4-4) using finite element method. The equation (4-2) explains the boundary condition with contact impedance included, equation (4-3) is for total amount of current injected to excitation electrodes, and equation (4-4) is to represent the zero current for the rest of boundary area.

The different imaging mode with a Tikhonov type algorithm was used for the image reconstruction:

$$\Delta\sigma = \left(\mathbf{J}^T\mathbf{J} + \gamma\mathbf{R}\right)^{-1}\mathbf{J}^T\Delta\mathbf{Y} \tag{4-5}$$

where **R** is the regularisation matrix (identity matrix), **J** is the Jacobian matrix, γ is the regularisation parameter and $\mathbf{\Delta Y}$ is the measurement vector, which was selected empirically with test samples in experimental data.

Our 16 electrode EIT system, in a LabVIEW environment based on National Instruments (NI) cards, was used in this study. Figure 5-1 shows the imaging capability of the EIT system used in this study, $\gamma = 0.001$ was a suitable choice for the regularisation parameter here. Figure 4-1(a) demonstrates our EIT system used in this study while being images four bottles in an imaging area and figure 4-1(b) is the EIT reconstructed images of the four bottles. The imaging area is 230 mm diameter. An adjacent current pattern (HOLDER, 1993) with the electric current of 5 mA in a single frequency of 10 kHz was used.

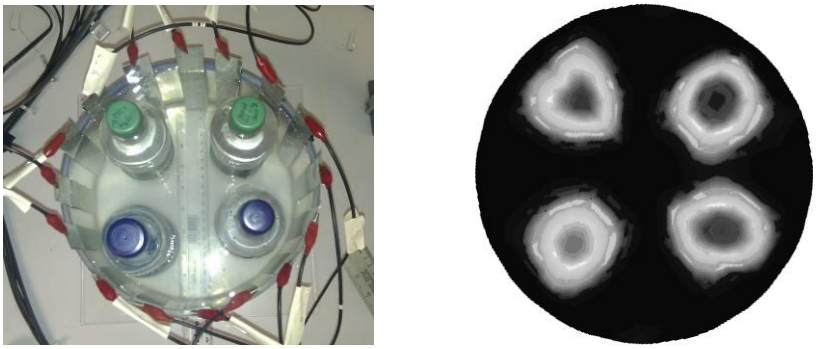

(a) (b)

Figure 4-1 An example of EIT image reconstruction for four inclusions by our system.

4.2 Motion extraction from low resolution images

Due to a high temporal resolution imaging system and an ability of producing internal human organ images, a new approach using EIT imaging, as motion monitoring system, is introduced in this thesis. EIT imaging with its high temporal resolution is able to capture dynamic images of fast moving objects. However, EIT is an imaging system that provides low spatial resolution images. Therefore, the EIT image can not capture small objects in an imaging area.

To be used as motion detection system, EIT can produce a series of images of the boundaries of large objects. The positions of the moving objects are captured by the EIT system. Then, the motion information can be measured from the displacements of the objects between two consecutive images. This motion information will be utilized by the CBCT iterative reconstruction for the motion compensation. To achieve this propose, a simple motion extraction software was developed for this study, especially for the low spatial resolution images.

A MATLAB programme was developed to identify the motion of large objects from a sequence of low spatial resolution images using a simple motion extraction technique. The technique was an image processing thresholding technique developed and used in Pengpan et al., 2011a and Terzija et al., 2010 (PENGPAN et

al., 2011, TERZIJA et al., 2010). The images were converted to binary images, using a simple thresholding technique by average values of maximum and minimum pixel values for each image. The centre of objects within a binary image was defined as centroid (the centre of mass of the object) by given the horizontal coordinate and vertical coordinate of mass. Then, the centroid was tracked for a sequence of images. This resulted in the displacement of the positions of centroids between the sequence images and the first image, then so called "EIT motion model".

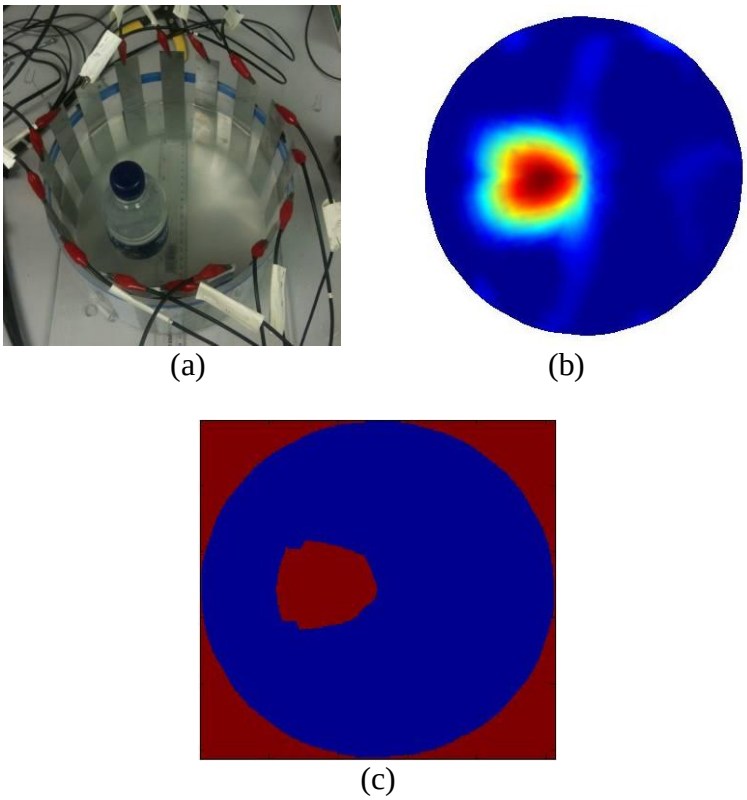

(a) (b)

(c)

Figure 4-2 (a) Position of an object in a tank phantom; (b) Conductivity distribution image of the object; and (c) Binary image of (b).

Figure 4-2(b) illustrates a low spatial resolution EIT image of a bottle placed in the imaging area as shown in figure 4-2(a). Figure 4-2(c) is the binary image of figure 4-2(b) by using the average pixel value of figure 4-2(b) as a threshold point. It is important to notice that the EIT system is not used to detect the small objects such as a tumour; it will only be used to detect the movement of the larger organs/objects (e.g. lungs).

4.3 Motion extraction testing

As noted, the EIT was proposed to be used in this study for capturing moving objects. The simple motion extraction programme was tested with simulated EIT images. Two types of movement tests were done in simulation environment, including straight line movement test and circular movement test. There was a single measurement for both experiments. A series of two-dimensional images of an object with 30 mm radius was produced for each experiment. In these simulation tests, the object was moved point-to-point discretely in the imaging area of 140 mm radius.

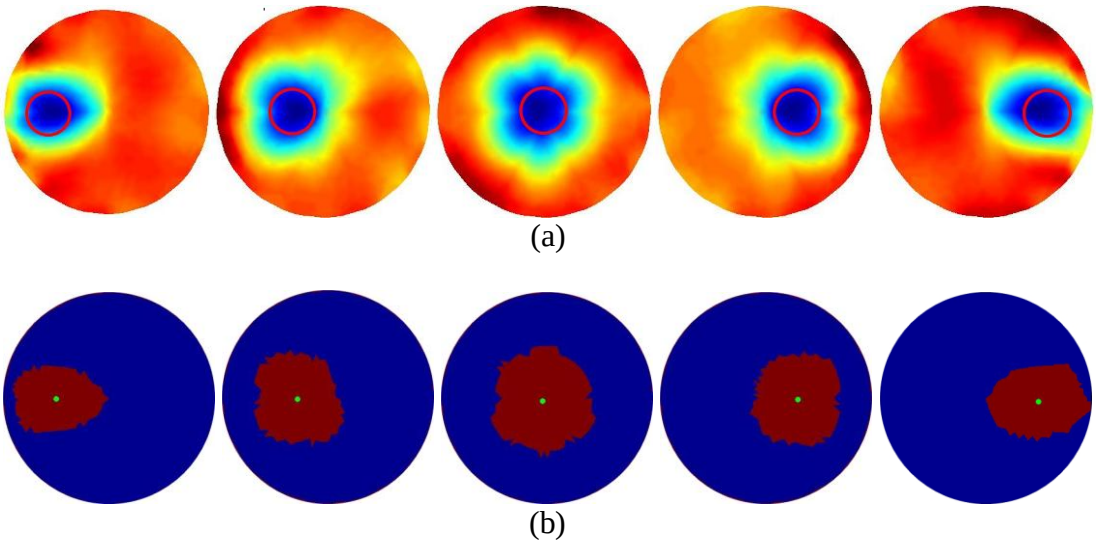

Figure 4-3 (a) A series of EIT images of an object moved in straight line movement in simulation (the red circles show the true position of the object); (b) A series of the binary images converted from (a) with the centroids.

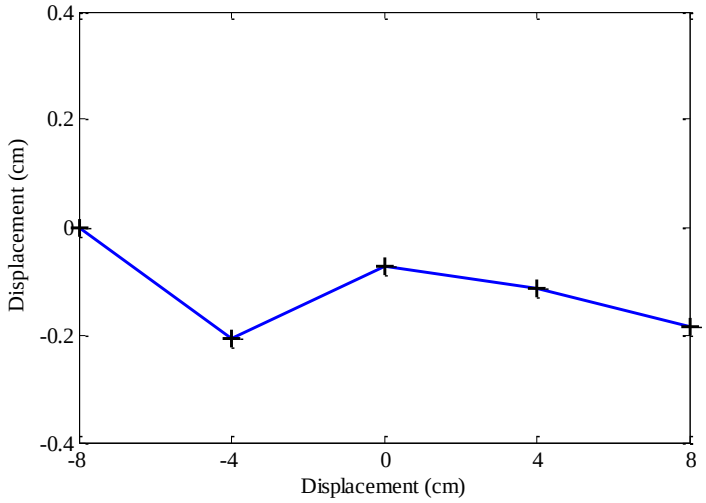

Figure 4-4 A plot of the extracted motion model of straight line movement in simulation.

The EIT images of a moving object in straight line pattern from the left to the right are shown in figure 4-3. Figure 4-4 shows the moving path of a single measurement of an object extracted from the EIT images (figure 4-3) using the simple motion extraction software developed above. A small error can be seen in the moving path which may be caused by the motion extraction programme, while determining the threshold of the pixel values and extracting the centroid of the moving object from the background in the EIT images. Due to the low resolution of EIT images, the boundaries of objects are blurred therefore with the simple thresholding technique it is difficult to determine the exact boundaries of objects. Nevertheless, this demonstrates the possibility of using this motion detection for extracting motion model from low spatial resolution EIT images. Next, the experiment of circular movement is shown.

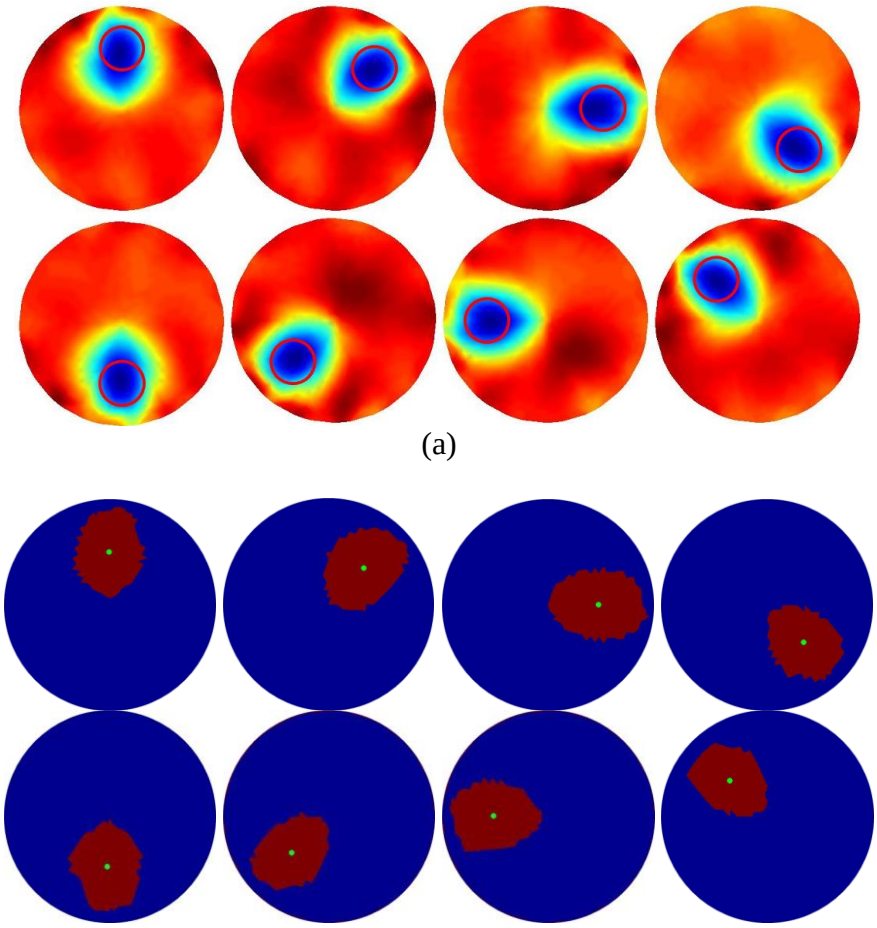

Figure 4-5 (a) A series of EIT images of an object moved in circular movement in simulation (the red circles show the true position of the object); (b) A series of the binary images converted from (a) with the centroids.

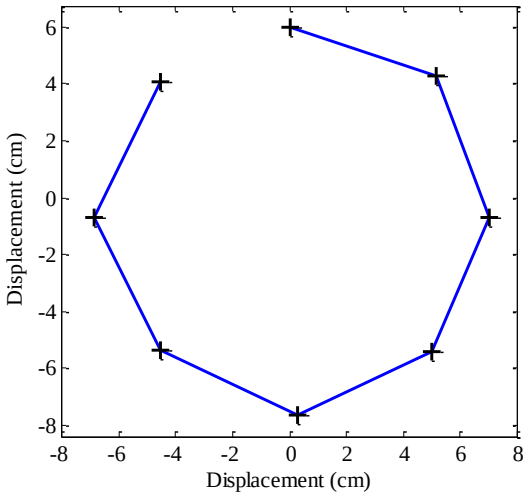

Figure 4-6 A plot of the extracted motion model of circular movement in simulation.

The results of circular movement pattern are shown in figures 4-5 and 4-6. The motion model extracted from a moving object shows the relative positions of the object in the EIT images (in figure 4-5).

The results of the motion extraction from EIT images suggest that the simple motion extraction software using the thresholding technique can be used to track the displacements of moving objects from the low spatial resolution images (5-10% of an imaging area). This motion extraction technique was also verified for motion detection in Magnetic Induction Tomography (MIT) (TERZIJA et al., 2010).

Chapter 5

Motion-Compensated ART of CBCT, Full Data

To study the proposed dual modality of motion-compensated CBCT using a motion model extracted from EIT images, the ART was first studied as a motion-compensated CBCT image reconstruction algorithm. A number of phantom studies were carried out , the results of which are presented in following sections. Due to a majority of image artefacts occurred near high contrast objects, a simple high density 3D simulated phantom ($256\times256\times256$ pixels) was used (figure 5-1). Where appropriate, relevant lines or planes are indexed using pixel coordination x,y,z $\in$ [1,256]. The size of phantom is $256\times256\times256$ mm (0.1 mm/pixel). The developed motion compensation technique is in 3D cone beam setting. For the reason of computational times of iterative methods, most of experiments here are shown in a slice (z=122) of the 3D cone beam as shown in figure 6-1(top, right).

In this experiment, The projection data were collected at every degree through 360 degrees, $B=360$, for a full data set reconstruction and each projection contained 512 measurements, $M=360\times512$. Then, the CBCT images were reconstructed by using 40 cycles with $\alpha=0.3$(equation 3-14). The parameters of the ART (e.g. the number of cycles, the rate of change of the relaxation parameter defined by α) were not optimized on a case-by-case basis; however, the results for the simulated data in section 5.1 suggested that the parameters are reasonable.

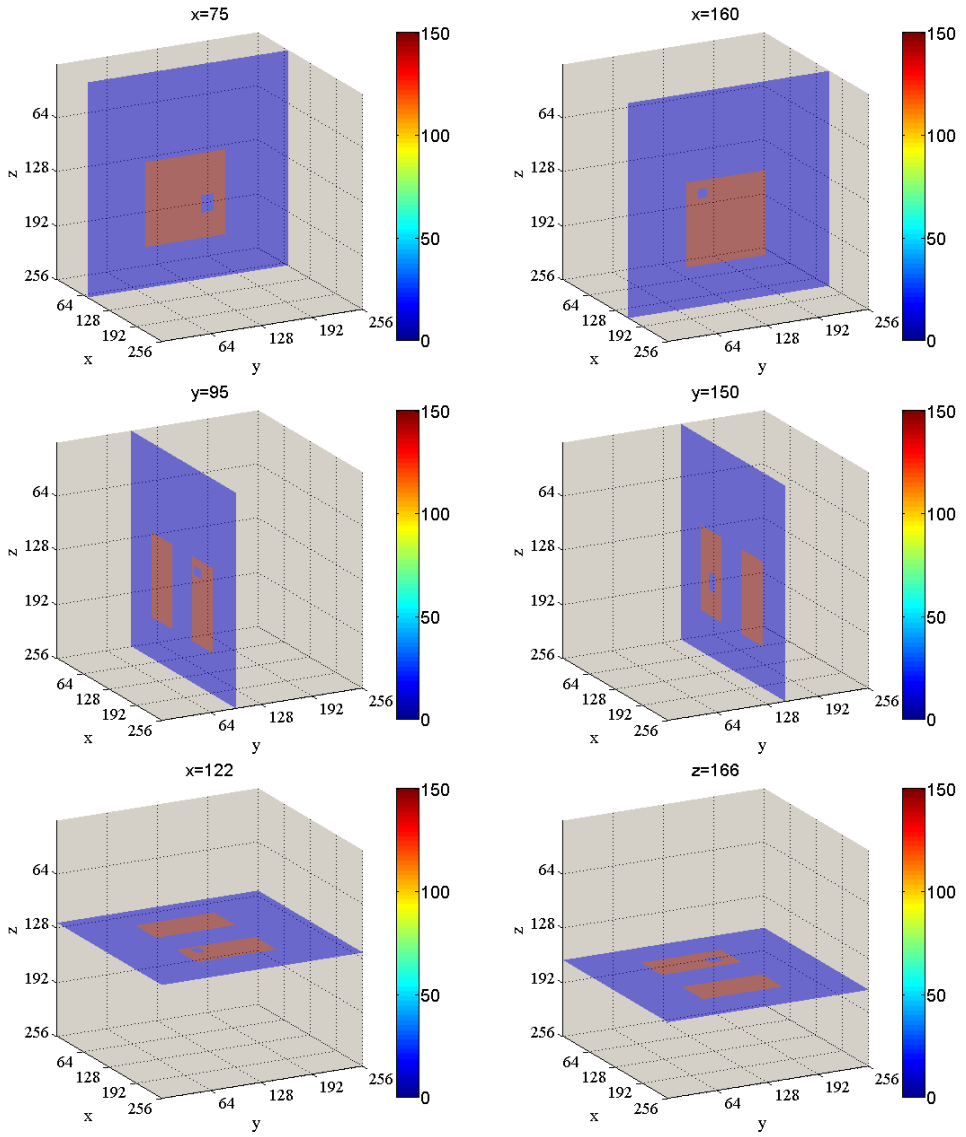

Figure 5-1 Example planes of a 3D simulated phantom.

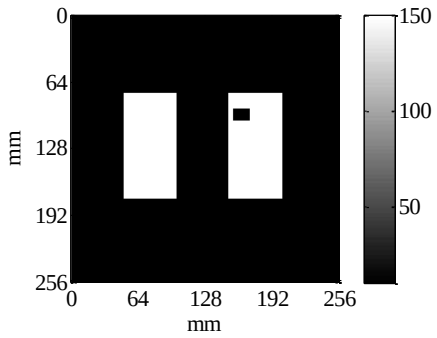

Figure 5-2 A plane of 3D phantom at z=122.

5.1 Correct motion-compensated ART

A correct motion compensation described in section 3.3 was examined here using ART algorithm with full projection data reconstruction. A moving phantom was produced by applying a simple sinusoidal motion model of 20 mm peak-to-peak amplitude (figure 5-3) to the simulated phantom (figure 5-2), when collecting projection data, in the left-right (LR) direction (x direction in figure 5-1) . This motion frequency is approximately 11-and-a-half cycles for 1 minute of full CBCT data acquisition.

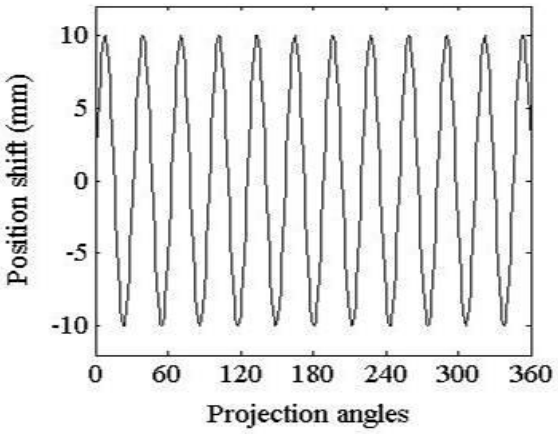

Figure 5-3 A 20 mm peak-to-peak sinusoidal motion model.

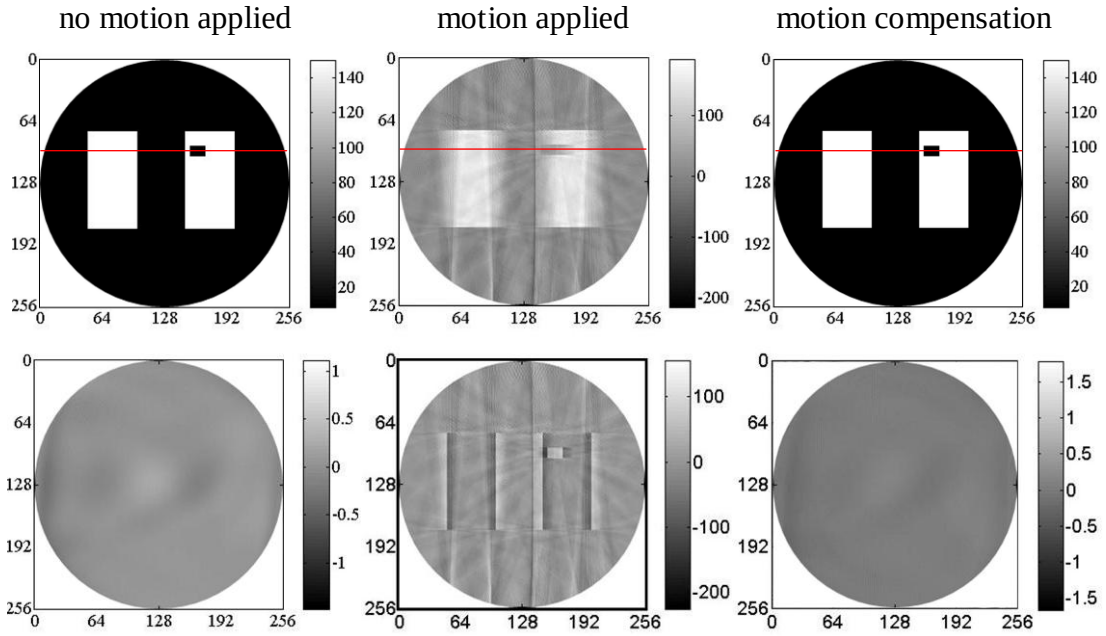

Figure 5-4 Image reconstruction when no motion applied, 20 mm of motion applied in the LR direction but no motion compensation, and motion compensation applied: top row is reconstructed images, bottom row is error images (the red lines are 1D plot in figure 5-5).

Figure 5-4 shows the results of the correct motion compensation study when motion was introduced in the LR direction. The CBCT reconstructed image when no motion is applied is shown in figure 5-4(top, left). When the motion is applied and no motion compensation is used, there is a significant blurring as shown in figure 5-4(top, middle). However when the motion is applied and motion compensation is used, figure 5-4(top, right) shows an improved ability to detect the boundaries of small objects. The bottom row of figure 5-4 shows the error images between the reconstructed images and the true phantom. It can be clearly seen an higher image error in the motion image, in particular around the edges of the phantom, and this error is significantly removed in the motion-compensated image.

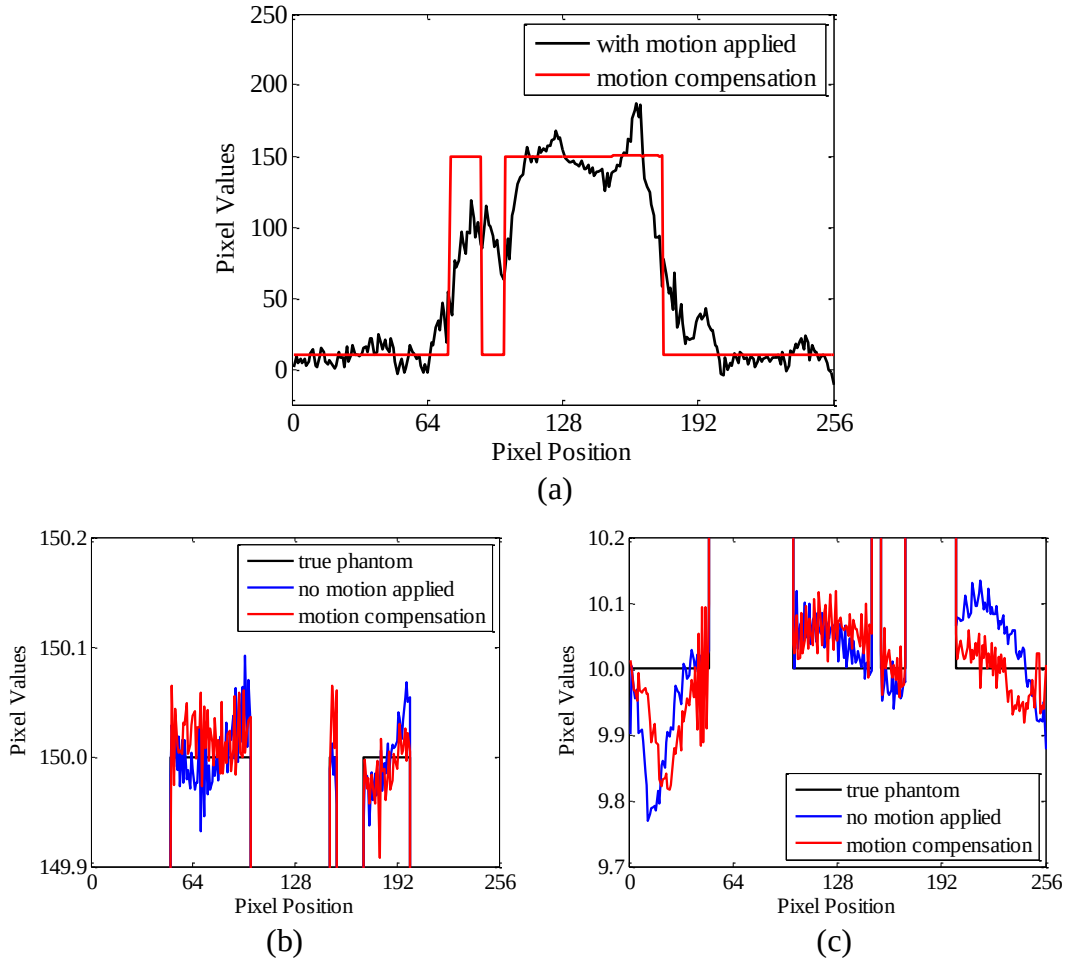

Figure 5-5 (a) Image row plots of figure 5-3 at y=94; (b)-(c) Magnification of image row plots with inclusion of the true phantom.

Profiles running through the middle of the small rectangular hole in the reconstructed images, without and with motion compensation, are plotted in figure 5-5(a). These plots confirm that the motion-compensated image shows an improvement in the edges of the phantom, which reduces the blurring artefacts that are mainly created by the motion. Figures 5-5(b) and (c) show magnification of the image row plots for the true phantom and the reconstructed image when no motion applied and when motion applied and motion compensation used. The plots illustrate that, in these two experiments, the ART has almost converged to the true phantom data; the plots also indicate the nature of those convergence errors.

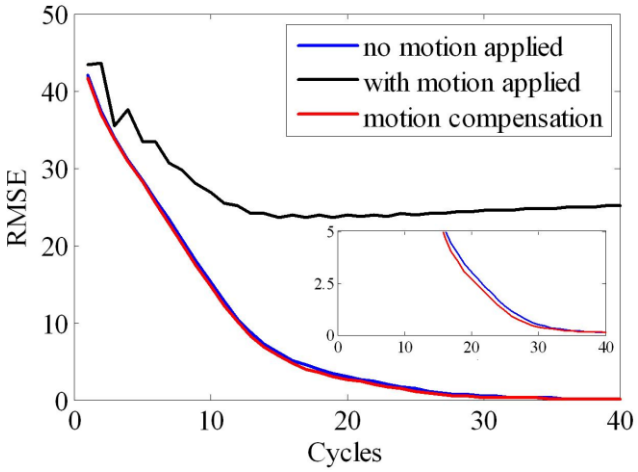

Figure 5-6 RMSE plots of CBCT reconstructed images

Figure 5-6 shows the convergences of the ART reconstruction when no motion is applied, when motion is applied but no motion compensation, and when motion is applied with motion compensation is used. The plots illustrate that the behaviour of image reconstruction, when motion is applied and motion compensation is used, shows a similar behaviour to image reconstruction, when no motion is applied. When compared with motion is applied and no motion compensation, the motion compensation reconstruction also has a quicker convergence rate, and lower image error. These results suggest that the motion-compensated ART with full data set reconstruction, using a correct motion model, can improve the blurring effect caused by motion.

However the main assumption made here was that the motion was compensated correctly, which is unlikely in real applications. Next some unknown motion errors were added into the motion model.

5.2 Approximated motion-compensated ART

The study of the motion compensation with using a correct motion model shows that motion blur artefacts can be reduced by using the developed motion compensation technique. In this experiment, the simulated phantom was moved in the up/down direction (y direction in figure 5-1) with the 20 mm peak-to-peak amplitude

sinusoidal motion (figure 5-3). Additionally, the motion model d was corrupted by noise E to give the corrupted signal d' where,

$$d' = \begin{cases} d + E, \text{if } d > 0 \\ d - E, \text{if } d \le 0 \end{cases}, \tag{5-1}$$

and,

$$E = q \times \frac{\rho}{100} \times \frac{\eta}{2}, \tag{5-2}$$

and ρ is the percentage error, η is the peak-to-peak amplitude, and q is randomly sampled from the range $q \in (0,1)$ according to a uniform distribution. The noise model therefore, in effect, preserves the zero-crossing in the original motion model to make sure that the motion model is corrupted by only random amplitude and the results are resulting from amplitude error. Here, the percentages ρ were chosen from 10% to 50%. The RMSE plots is shown in figure 5-7. The additive motion error introduces error into the reconstruction despite the motion compensation, since the motion compensation uses an incorrect model, so called "approximated motion compensation". The greater the additive error, the higher the image error.

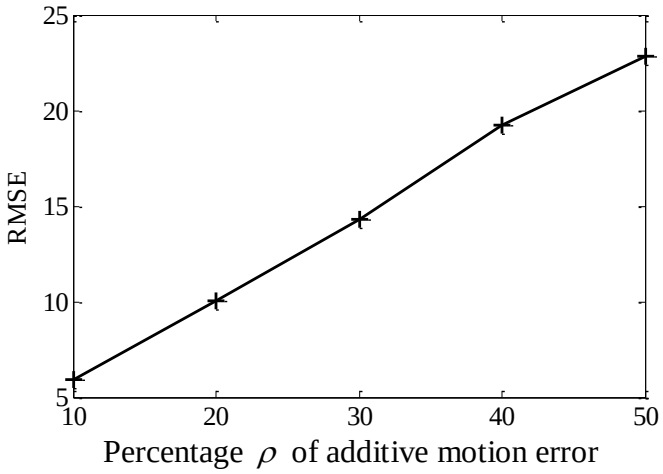

Figure 5-7 RMSE plots of CBCT reconstructions images with different percentages of additive motion error.

Figures 5-8(a) and (b) illustrate the motion compensation when using correct motion model, given motion in the up/down direction. After applying motion in the up/down direction, blurring can be seen on the reconstructed image as shown in figure 5-8(a). Figure 5-8(b) shows an improvement of motion blur artefacts when the correct motion model was used. The boundaries of a small rectangular object can be seen more clearly in the motion-compensated image than in the motion image. Figures 5-8(c) to (e) show the reconstructed image when the motion-compensated ART was used; here the pure sinusoidal motion model d is used in compensation, but the noise-corrupted signals d' with $\rho \in \{10,30,50\}$ were applied to the raw projection data. For the noise-corrupted data, additive errors were used with $\rho \in \{10,20,30,40,50\}$. An increasing in the additive motion error results in an increase in the blurring effect. For reconstructed images (figures 5-8(c) to (e)), the motion-compensated images with 10% and 30% motion error show an improvement in the sharpness of the boundaries, compared to the uncompensated image, but not with 50%. The error images of images when motion is applied, motion applied and correct motion compensation is used and motion applied and approximated motion compensation is used are shown in figure 5-9. The error image of 10% error added (figure 5-9(c)) has shaper edges than the error images of 30% (figure 5-9(d)) and 50% error (figure 5-9(e)) added. This confirm that higher motion errors results in higher motion artefacts remaining after the compensation. Hence the motion compensation is beneficial even with a less accurate estimation of the motion, but the performance degrades when the motion model become more inaccurate. The image row plots running thought x=162 shown in figure 5-10 confirm this results.

In summary, the study of the approximated motion compensation suggests that the performance of this motion compensation technique depends on the accuracy of motion estimation and some errors in the motion estimation are tolerable. This amplitude error study in motion compensation is not such a problem which is well known form standard motion sorted FDK in clinical practice. However, other type errors would be investigated in the next chapter.

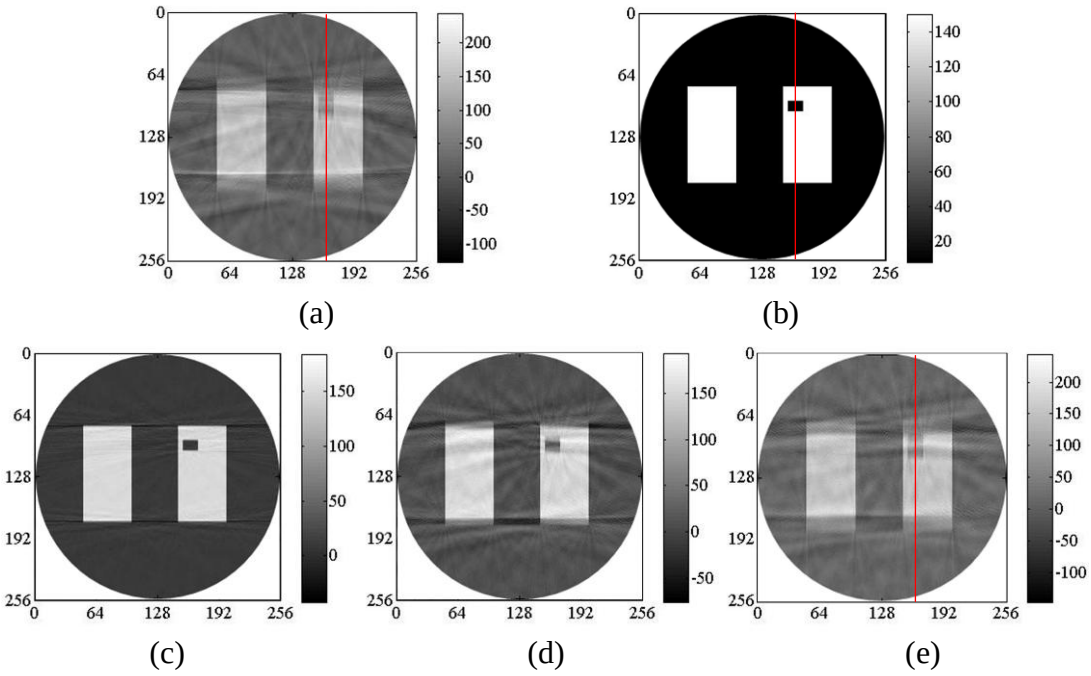

Figure 5-8 Image reconstruction of the simulated phantom when (a) 20 mm of up/down motion applied, (b) correct motion compensation applied, (c) approximated motion compensation applied after 10% motion error added, (d) motion compensation applied after 30% motion error added, (e) motion compensation applied after 50% motion error added (the red lines are 1D plot in figure 5-10).

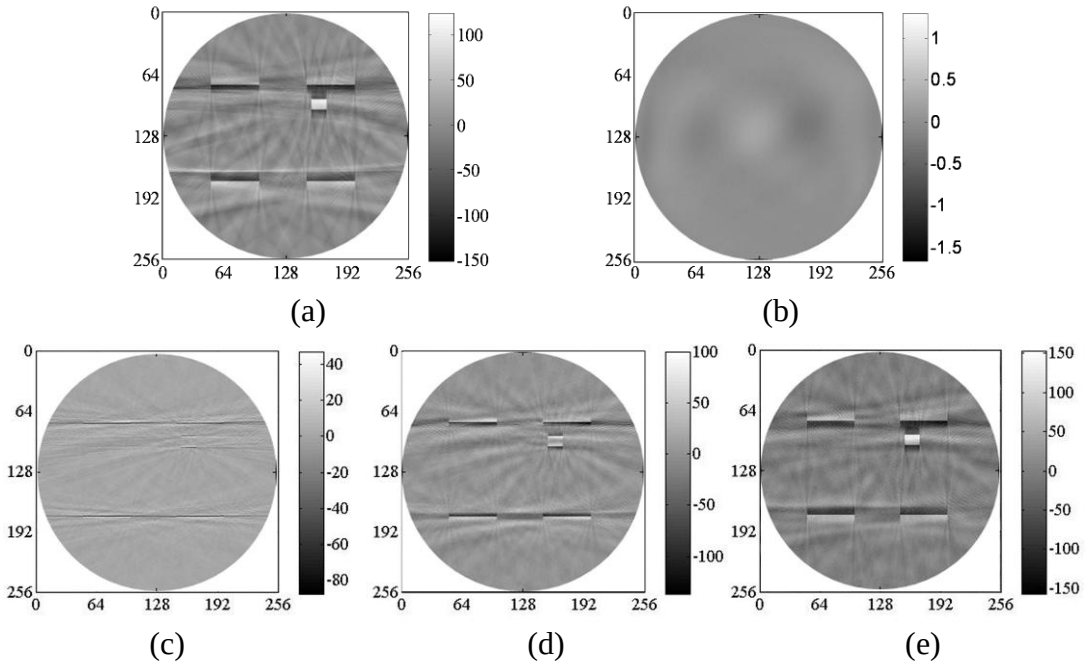

Figure 5-9 Error images of figure 5-8.

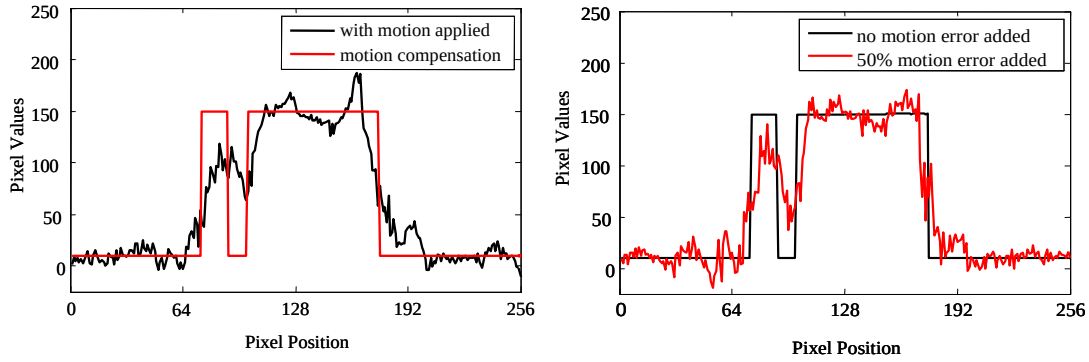

(a) (b)

Figure 5-10 Image row plots at x=162 (a) for motion image and correct motion-compensated image, (b) for correct motion-compensated image and approximated motion-compensated image after 50% additive motion error.

5.3 Conclusions

The ART is a simple algebraic iterative reconstruction method which allows modifying between each iteration. These results were collected from the experiments of the full data set reconstructions of the motion-compensated ART comparing among no motion applied, when motion applied but no motion compensation, and when motion applied and the correct motion compensation applied. Moreover, the approximated motion compensation was also investigated for studying the feasibility of the motion compensation technique. The simulated experimental results indicated that the motion-compensated ART with full data reconstruction showed the ability to reduce blurring artefacts due to motions from the reconstructed images especially for the correct motion compensation. However, for the approximated motion compensation, the performance of the motion compensation technique depended on the accuracy of motion estimation. The blurring artefacts were noticeably seen in the reconstructed images with high motion error.

Chapter 6
Motion-Compensated ART, SART, OS-SART and CGLS with Limited Data

The results from chapter 5 suggested that motion artefacts could be reduced by using the motion compensation technique developed in this study. Additionally, the patient's radiation dose receiving from an imaging system is often concerned. To reduce the radiation dose to patients, reconstructions with limited data have been investigated. Image reconstruction techniques using limited data acquisition have been investigated by many researchers (ANDERSEN, 1989, CHLEWICKI et al., 2001, SUBBARAO et al., 1997). Chlewicki et al., 2001 showed that SART gave better results than FDK when limited data was used. From a practical view, acquisition time is also decreased, when the limited data reconstruction is used.

Therefore, a combinatorial technique of the motion compensation with the limited data reconstruction would be interesting, and needs to be further investigated. In this chapter, the study aim was to perform a combinatorial reconstruction using motion-compensated CBCT and limited data reconstruction, in the context of ART, SART, OS-SART and CGLS.

The simple simulated phantom generated in chapter 5 was also used in this study. Ninety individual projections were generated, evenly distributed through 360°, i.e. one-fourth of a full set of 360 projection data. Each projection contained 512 measurements. Hence, $N = 256^2$, $M = 90 \times 512$ and $B = 90$. The experiments were

arranged as follows. In theory, α value in equation (3-14) forces the convergence rate of the reconstruction. Then to determine an optimal α value, the performances of ART, SART, and OS-SART with limited data reconstruction were investigated in the first experiment by varying the α values. It is noted that OS-SART used one projection in each block; this was suboptimal since blocks were not well-balanced. In an attempt to account for real experimental situation, consistent and inconsistent cases were investigated. The inconsistent case was created by corrupted the right hand side of the equation (3-1), **Ax**=**b**, with an error. This error is often called an inconsistency term. Next, the motion compensations with limited data using a correct motion model were studied. Finally, the approximated motion compensations were investigated by applying a motion model including of three types of error (amplitude error, phase error, and random additive Gaussian error). It is noted that the first experiment was performed in only ART, SART and OS-SART, but not for CGLS. The definition of RMSE for ART is equation (3-23), and for SART and OS-SART is in equation (3-24). The results were divided into 2 sections: the results of ART, SART and OS-SART reconstructions, and the results of CGLS reconstruction.

6.1 ART, SART and OS-SART

6.1.1 ART, SART and OS-SART reconstructions when no motion applied

Firstly, CBCT reconstruction of a static phantom, using ART; SART; and OS-SART, with different α values was studied. For each experiment, methods were run for 100 cycles with $\alpha \in \{0.01, 0.1, 0.5\}$. The results are shown in figures 6-1, 6-2 and 6-3. The RMSE plots (figure 6-1) demonstrate that the reconstruction with $\alpha = 0.01$ provides the smallest error for all ART, SART and OS-SART. Though there is little variation in the final RMSE value for ART under different α values. For ART, an increase in the α values, the convergence is quicker. In contrast, in SART and OS-SART, with the increasing of the α value, the convergence is slower. Moreover, after the 30^{th} cycle, ART keeps steady in RMSE, but SART and OS-SART are still be updating. Hence, for this simple problem, if using ART, 30 cycles seems to give

the adequacy; however SART and OS-SART need at least 100 cycles. From the plots, the convergence behaviour for SART and OS-SART are similar.

The reconstructed images are shown in figure 6-2, it can be clearly seen that, an increase in α value results in an increase in the blurring effect for all ART, SART, and OS-SART. The reconstructed images using SART and OS-SART with $\alpha = 0.5$ show less sharpness of the boundaries, but not with $\alpha = 0.5$ for ART. Hence at the same value of α, the experiments suggest that ART provides sharper boundaries than SART and OS-SART. To easily demonstrate reconstruction errors, the error images (figure 6-3) are produced by subtracting the reconstructed images (figure 6-2) with the true phantom. The ART reconstructions show less image errors when compared with SART and OS-SART for all α values and $\alpha = 0.01$ provides better edges than $\alpha = 0.1$ and $\alpha = 0.5$.

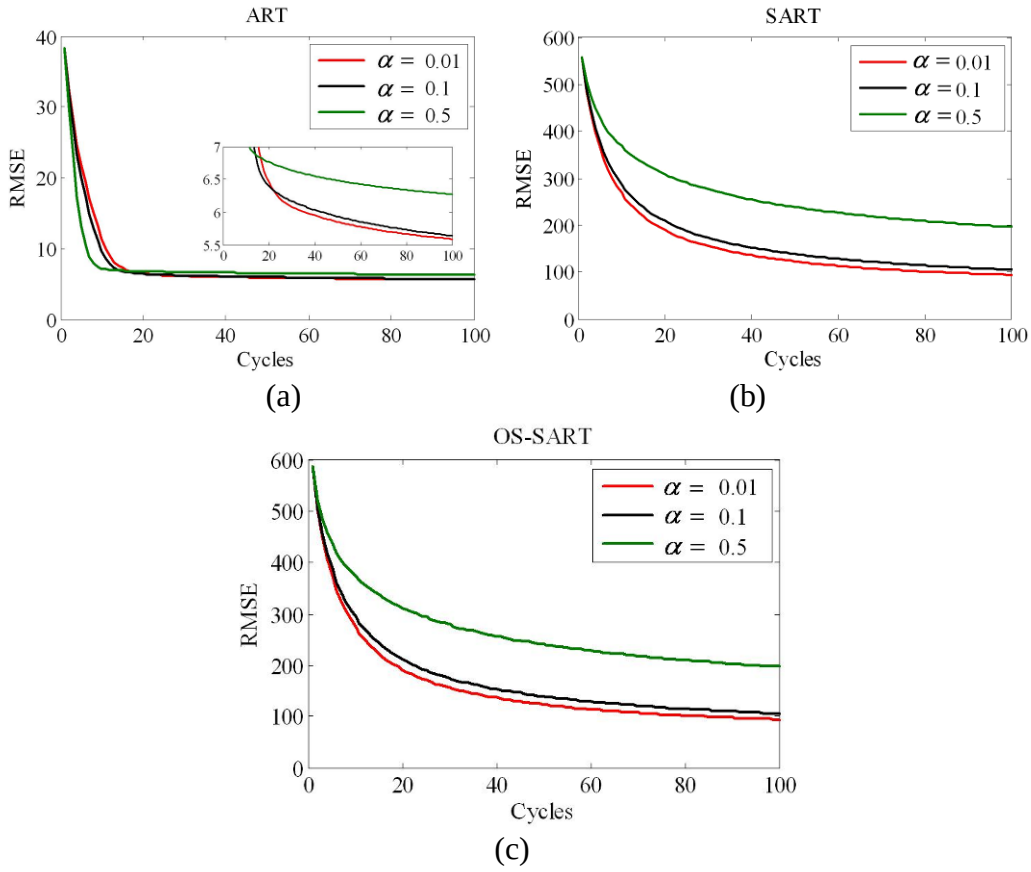

Figure 6-1 RMSE plots of the simulated phantom using (a) ART, (b) SART, and (c) OS-SART with $\alpha \in \{0.01, 0.1, 0.5\}$.

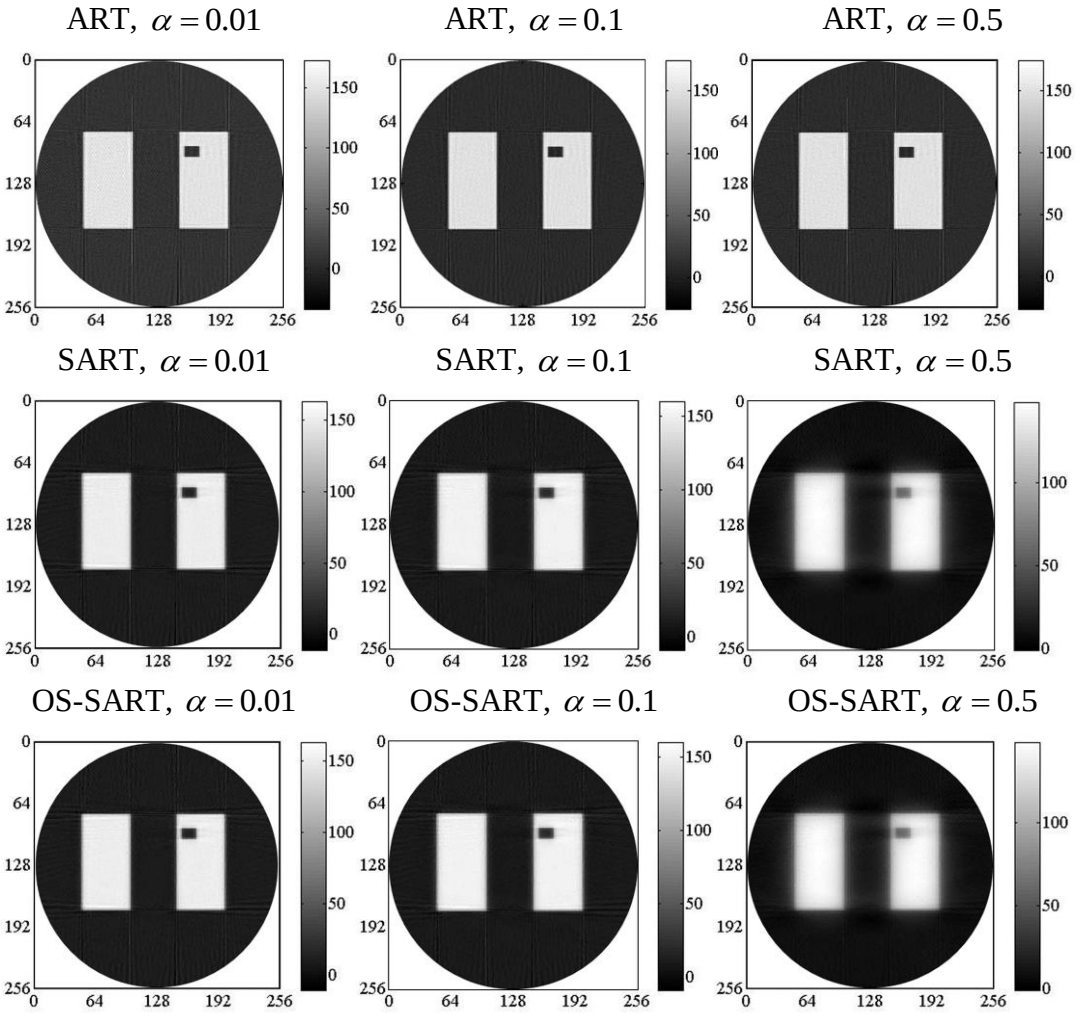

Figure 6-2 CBCT reconstructed images of the simulated phantom using ART, SART and OS-SART with $\alpha = \{0.01, 0.1, 0.5\}$ after the 100th cycle.

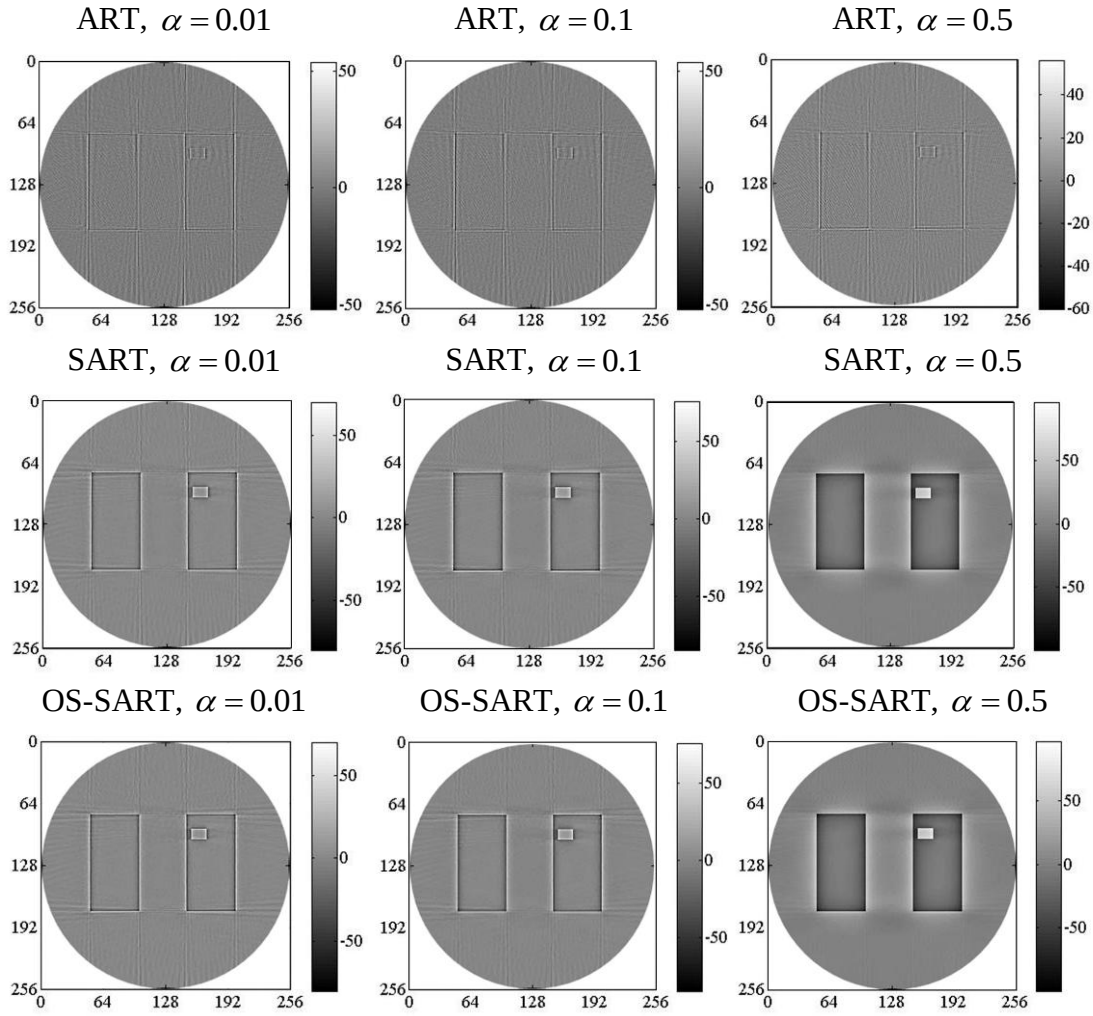

Figure 6-3 Error images of figure 6-2.

Among ART, SART, and OS-SART, ART is able to produce sharper edges; however ART yields ray-path artefacts.

6.1.2 ART, SART and OS-SART reconstructions for consistent and inconsistent cases

Next, the reconstructions of consistent and inconsistent cases were examined. According to the real clinical cases, most of the cases are inconsistent problems. The simulated phantom (figure 5-2) was implemented for the consistency study. For the inconsistent cases, random additive Gaussian noise was added separately to each projection, where the standard deviation was set to 5% of the standard deviation of the data within each projection. Each method was used for 100 cycles and $\alpha = 0.01$.

The RMSE plots are shown in figures 6-4 and the reconstructed images (top row) and error images (bottom row) are shown in figures 6-5 for ART, SART, and OS-SART, respectively. It is noted that the results for the consistent case were taken from section 6.1.1 with $\alpha = 0.01$. For the inconsistent case, the plots show ART diverges after about the 10^{th} cycle but not for SART and OS-SART. After the 100^{th} cycles, it can be seen in the reconstructed images shown in figures 6-5 that SART and OS-SART produce lower image noise than ART. These results are confirmed by error images (figure 6-5:bottom row) that ART produces higher noise than SART and OS-SART, then the blurring edges cannot be seen in error image of ART reconstruction.

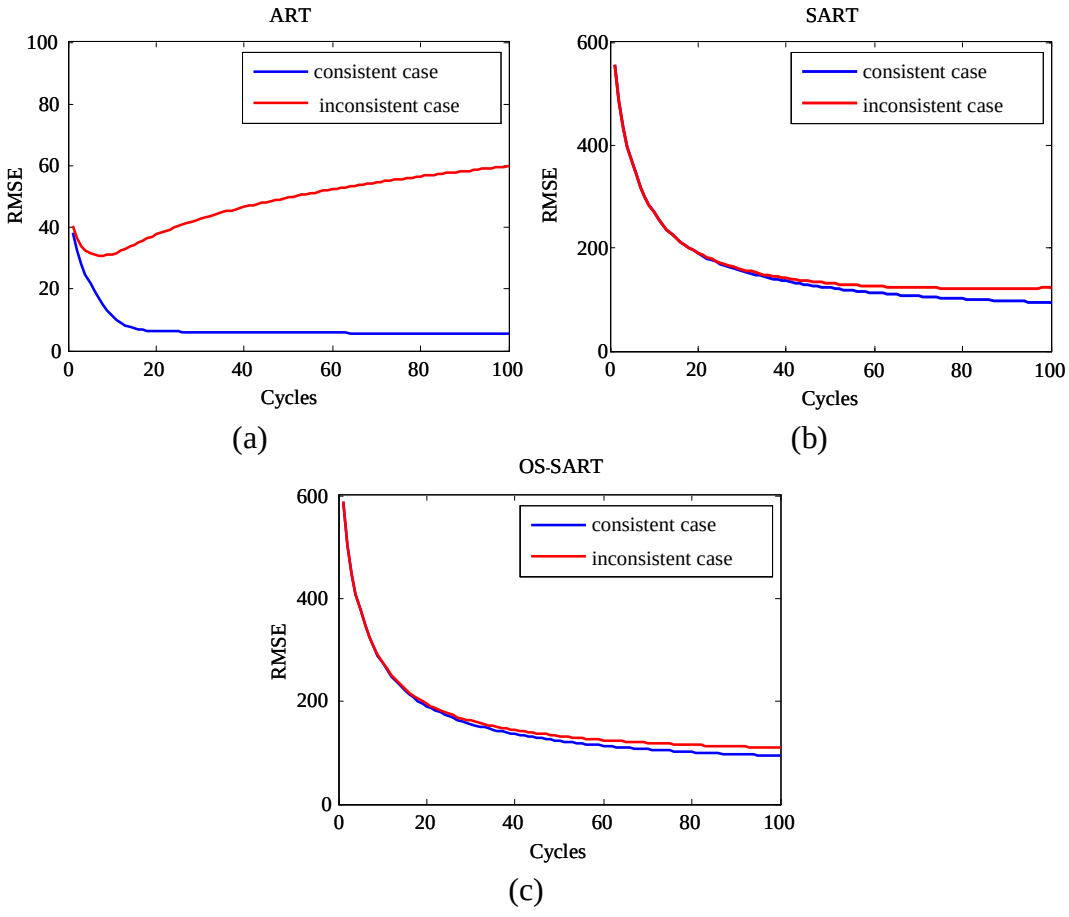

Figure 6-4 RMSE plots of consistent and inconsistent cases using (a) ART, (b) SART, and (c) OS-SART with $\alpha = 0.01$and 100 cycles.

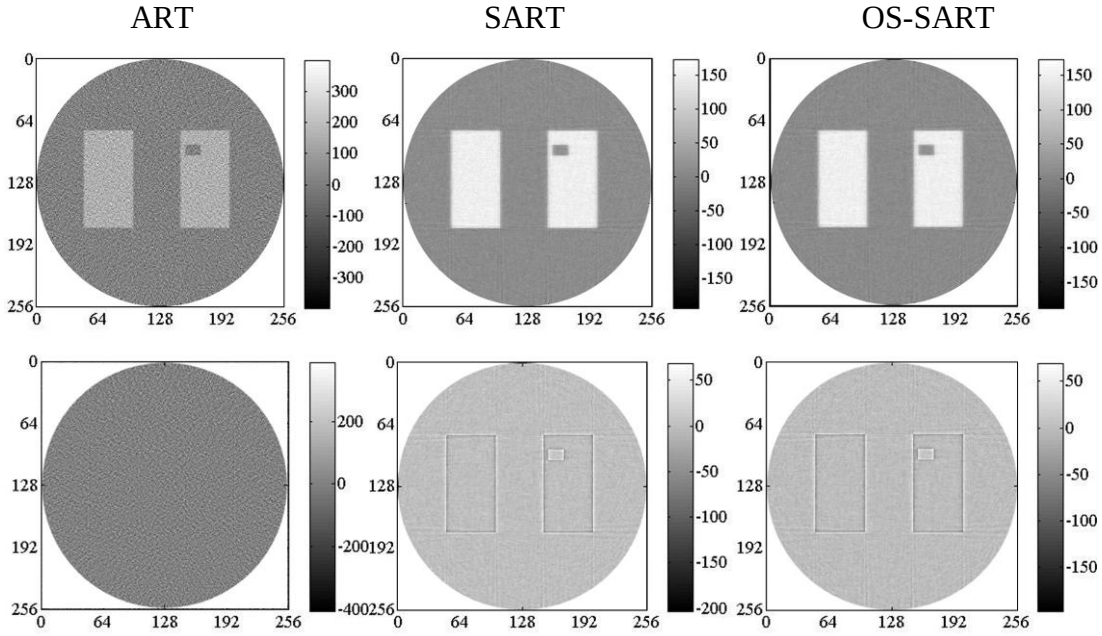

Figure 6-5 CBCT reconstruction after the 100th cycle for inconsistent case using ART, SART, and OS-SART ($\alpha = 0.01$): top row is reconstructed images, bottom row is error images.

The study of the inconsistent problem shows that ART diverges after a few cycles, but not for SART and OS-SART. ART also produces higher image noise than SART and OS-SART. This suggests that SART and OS-SART may be more robust than ART to inconsistency in equation (3-1), hence probably to inconsistencies due to motion.

6.1.3 ART, SART and OS-SART reconstructions for a moving object

Next, the image reconstruction for a moving object was studied, when the 20 mm peak-to-peak amplitude motion model (figure 5-3) was applied to the phantom in the up/down direction. The motion model was sinusoidal model as shown in figure 6-3. The RMSE plots of the reconstructed images for a moving object are shown in figure 6-6; figure 6-6(a) for ART with $\alpha = 0.01$, and $\alpha = 0.3$, and figure 6-6(b) for SART with $\alpha = 0.01$ and OS-SART with $\alpha = 0.01$. The RMSE plots of ART diverge after a few cycles, while the plots of SART and OS-SART do not diverge within 100 cycles. Figure 6-6 shows the comparison between the reconstruction images at each cycle and the reconstruction image at the 100th cycle. This plots confirm that while,

ART reconstructions diverge after a few cycles compared to the true image, the reconstructions still keep updating. The reconstructed images, in figures 6-7(a) to (d), confirm that if data is corrupted by motion, images obtained using ART are very poor. Figure 6-8 shows error images between the reconstructed image and the true phantom. It can be seen blurring around edges in SART and OS-SART, while not for ART. On the other hand, ART is almost corrupted by noise which is higher than SART and OS-SART. It can be assumed that ART is more sensitive to motion than SART and OS-SART. This supports the suggestion in section 6.1.2. However, the motion artefacts can still be observed in SART and OS-SART images, motivating the need of motion compensation.

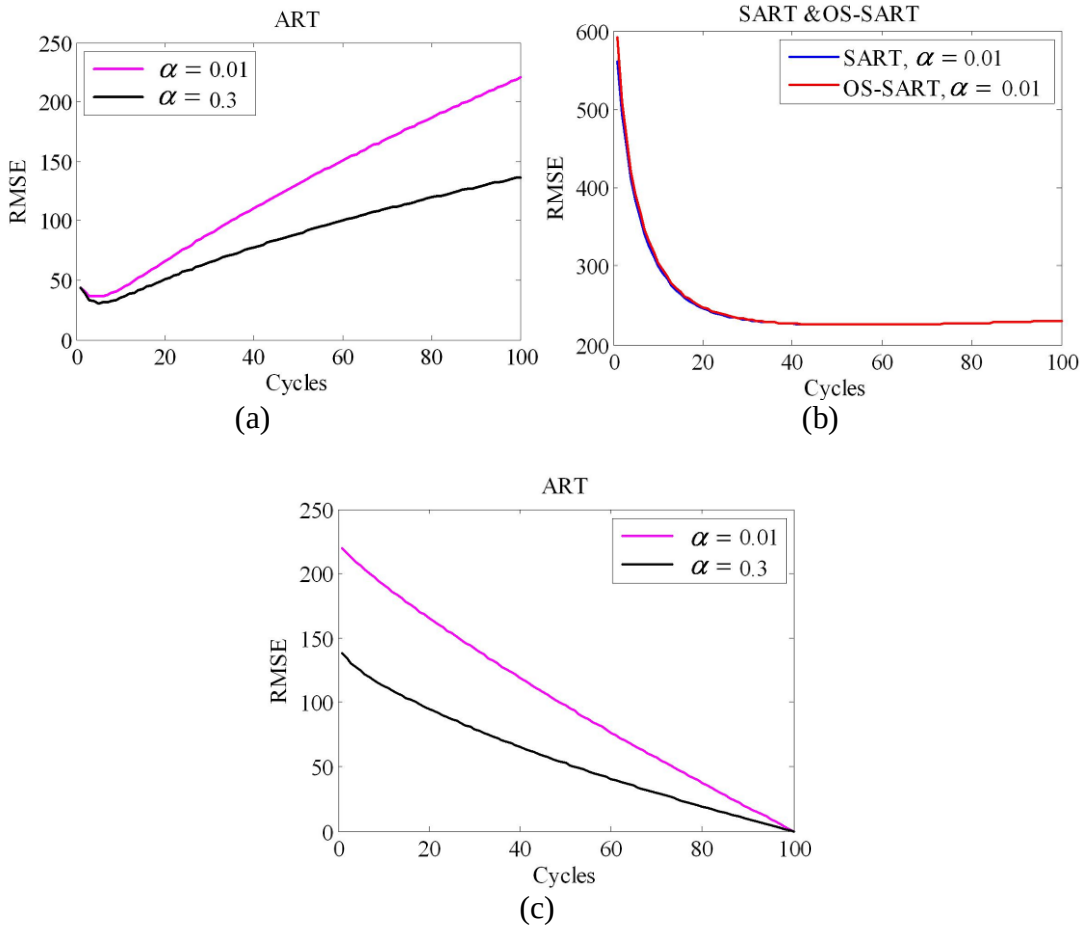

Figure 6-6 RMSE plots of the simulated phantom using (a) ART with $\alpha = \{0.01, 0.3\}$, and (b) SART and OS-SART with $\alpha = 0.01$; (c) RMSE plots of ART compared with reconstructed image after the 100th cycle.

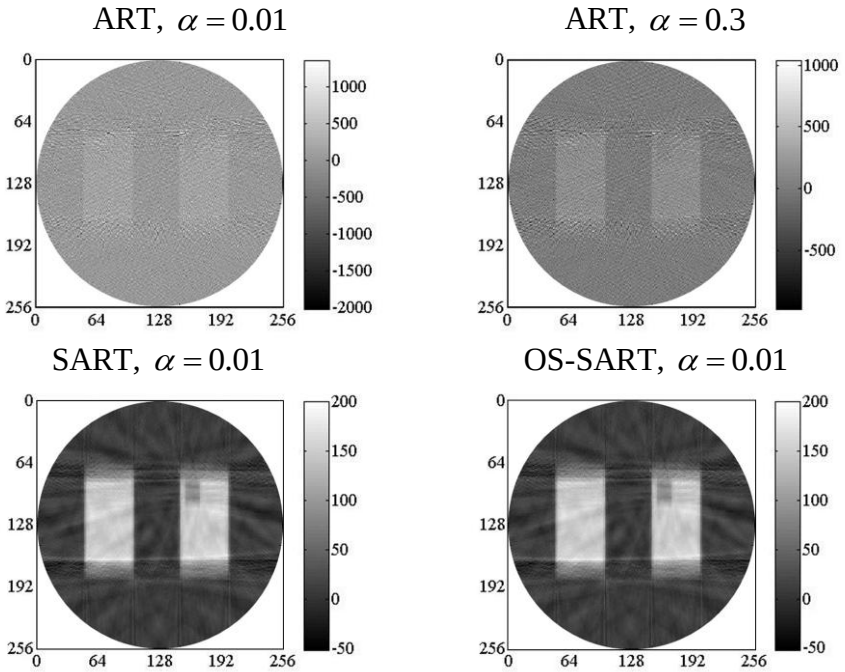

Figure 6-7 CBCT reconstructed images after the 100th cycle using (a) ART with $\alpha = 0.01$, (b) ART with $\alpha = 0.3$, (c) SART with $\alpha = 0.01$, and (d) OS-SART with $\alpha = 0.01$.

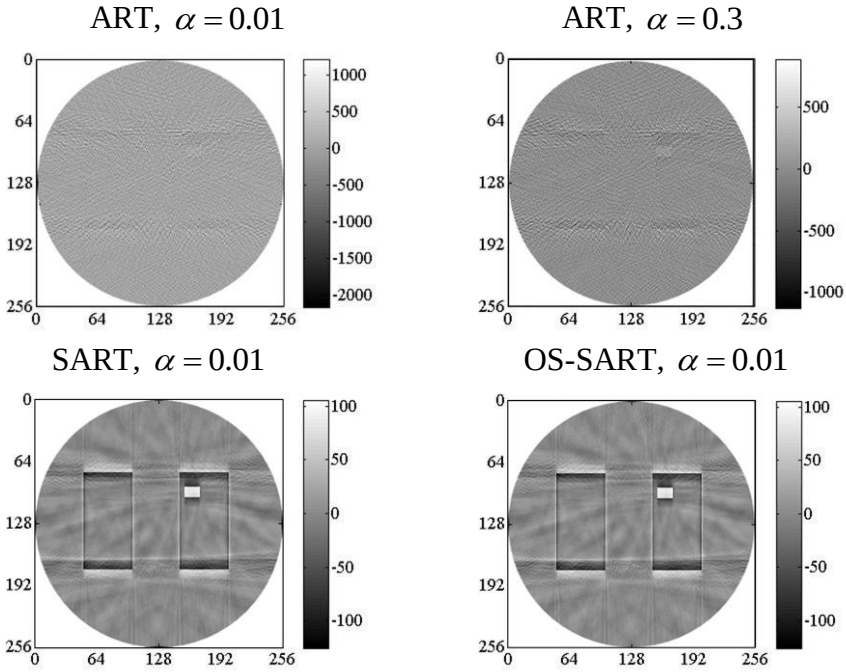

Figure 6-8 Error images of figure 6-7.

6.1.4 Correct motion compensation using ART, SART and OS-SART

The motion compensation was next investigated for ART, SART and OS-SART. The motion model illustrated in figure 5-3 was applied to the phantom for the up/down direction when collecting the projection data. The same motion model was used to compensate for the up/down motion. Hence, the correct motion compensation was studied in this experiment. The results are shown in figure 6-9, 6-10, and 6-11.

The RMSE plots of ART, SART and OS-SART with $\alpha = 0.01$ are shown in figures 6-9(a) to (c), respectively when no motion is applied, when motion is applied but no motion compensation, and when motion is applied with motion compensation is used. These indicate that the convergences of the motion compensation for all ART, SART and OS-SART almost recover to the reconstructions when no motion is applied. The reconstructed images of the motion compensation for ART, SART, and OS-SART are shown in figure 6-10. It can be seen that the motion-compensated ART, after both the 30^{th} cycle and the 100^{th} cycle, produces less blurring artefacts than the motion-compensated SART and OS-SART. Nevertheless, the sharpness of the boundaries of motion-compensated images, after the 100^{th} cycle for ART, SART, and OS-SART, is improved when compared to the uncompensated images in figure 6-7. The convergence of the motion-compensated ART (figure 6-9(a)) shows limited improvement after the 20^{th} cycle. This suggests that in case of using the motion-compensated ART for this problem, 30 cycles can be used to keep the reconstruction time. This is confirmed by the reconstructed images in figure 6-10. Error images of SART and OS-SART (figure 6-11) shows remaining edge blurring while ART shows lesser.

Of the correct motion-compensated techniques, ART provides a reconstructed image with sharper edges than SART and OS-SART. However, the performances of the correct motion compensation for SART and OS-SART were satisfactory. As the reconstructions of SART and OS-SART are very similar, in the next section, only ART with 30 cycles and SART with 100 cycles were used to investigate the effects

of including motion errors into the motion model for an approximated motion compensation study.

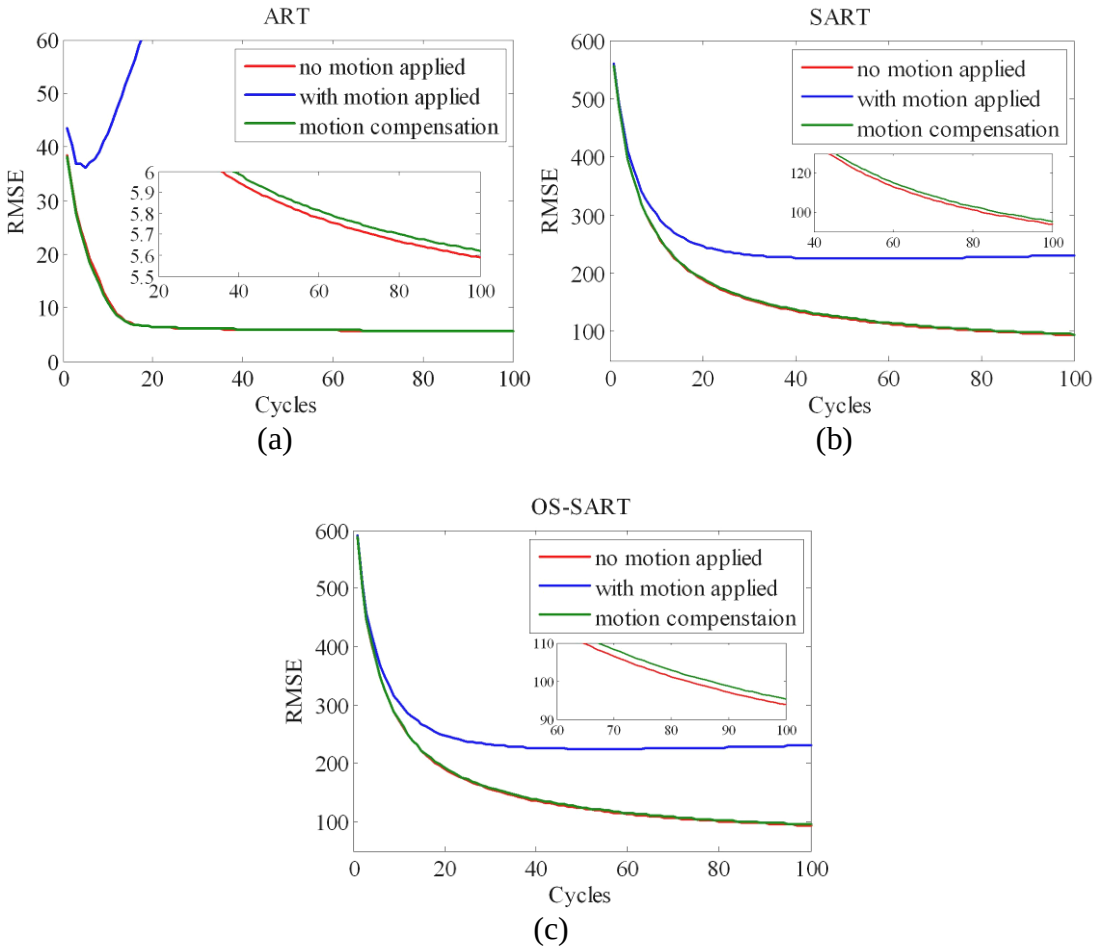

Figure 6-9 RMSE plots of motion-compensated images using (a) ART, (b) SART and (c) OS-SART.

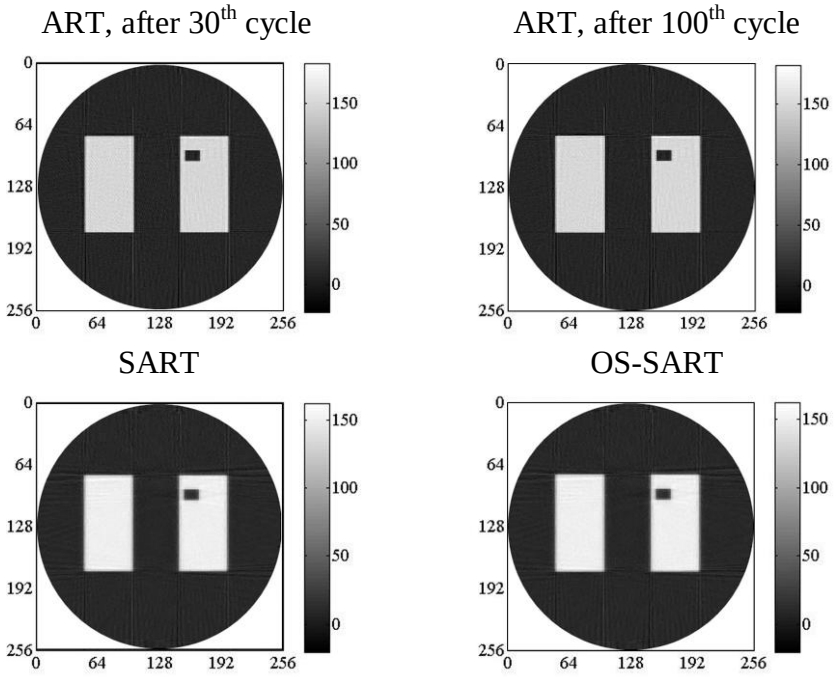

Figure 6-10 Motion-compensated images using ART after the 30th cycle, ART, (c) SART and OS-SART after the 100th cycle ($\alpha = 0.01$).

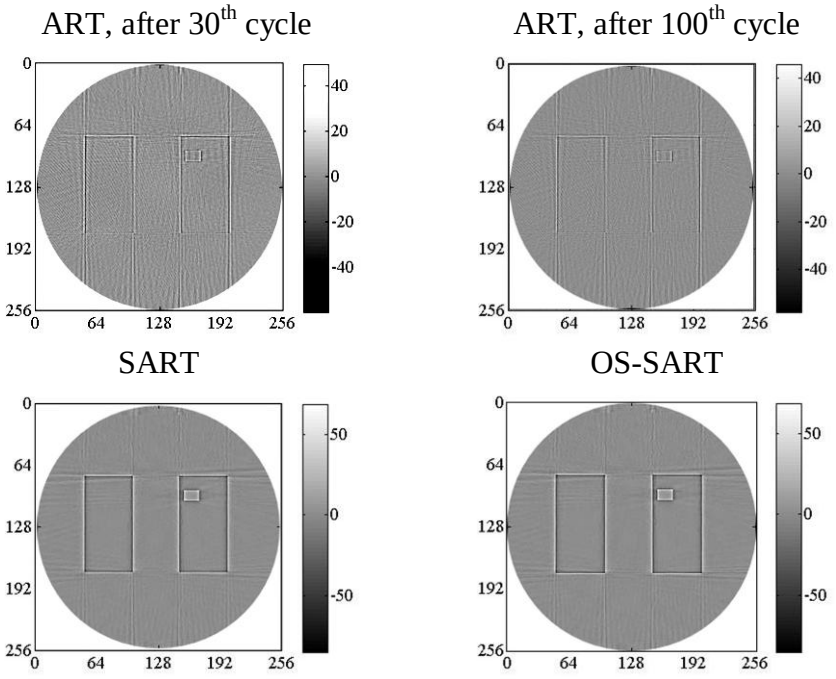

Figure 6-11 Error images of figure 6-10

6.1.5 Approximated motion compensation using ART and SART

This is the study of the motion compensation with error introduced into motion model. An erroneous motion model was used to move the phantom, when collecting projection data, but the true motion model was used in the motion compensation during iterative reconstruction. This simulates real-world problems, where it is difficult to estimate the actual motion model. Three types of motion error were used in this study: amplitude error, random additive Gaussian error, and phase error.

6.1.5.1 Amplitude error

The amplitude of the motion model, applied when collecting projection data, was varied by 5%, 10%, 15% and 20% of the 20 mm peak-to-peak amplitude of the original sinusoidal motion model. This is a systematic amplitude error. Examples are given in figure 6-12. The results are shown in figures 6-13, 6-14, 6-15, and 6-16Figures 6-13(a) and (b) illustrate the RMSE plots of the approximated motion compensation with amplitude error for ART and SART, respectively. As the cycle index of the motion-compensated ART was increasing, the RMSE eventually starts to diverge. The reconstructed images and error images for the motion compensation with different amounts of amplitude error are shown in figure 6-14 for ART, and 6-15 for SART. The figures indicate that, with the same amount of the amplitude error, ART produces higher level of noise than SART. While it can be clearly seen blurring edges in SART rather than in ART. In contrast, the blurring edges in the error image of SART is not noticeable in the 1D plots of ART and SART with 10% amplitude error added (figure 6-16) and the edges of ART and SART are not significantly different, but ART still shows higher noise. The tolerance to the amplitude error for the motion-compensated SART seems to be better than that in the motion-compensated ART.

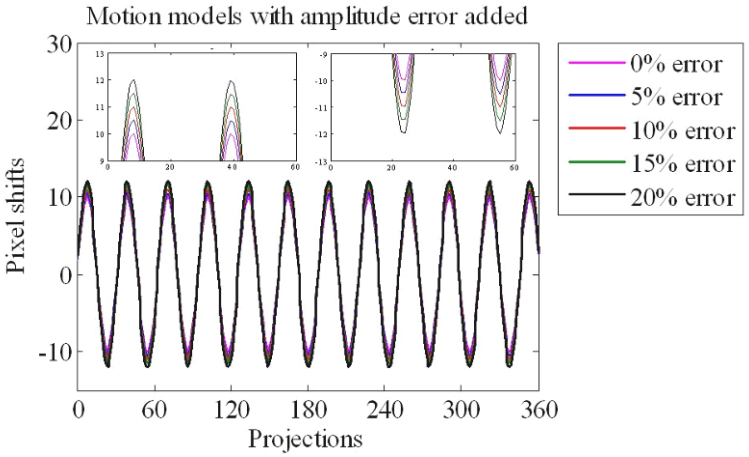

Figure 6-12 Motion models with different percentages of amplitude motion error.

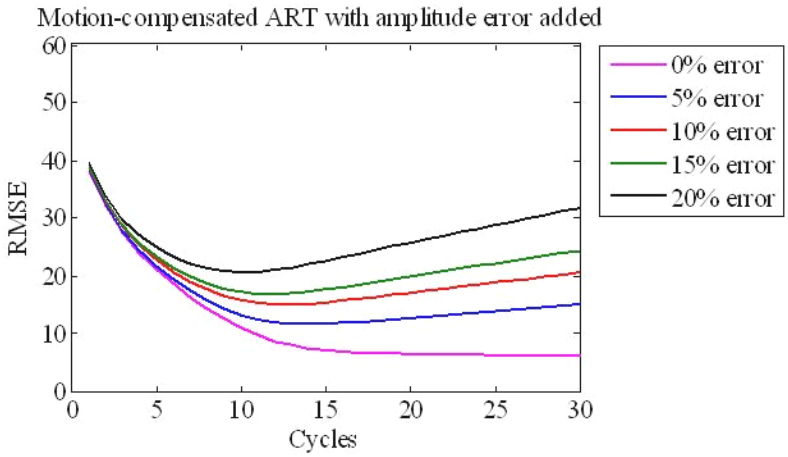

(a)

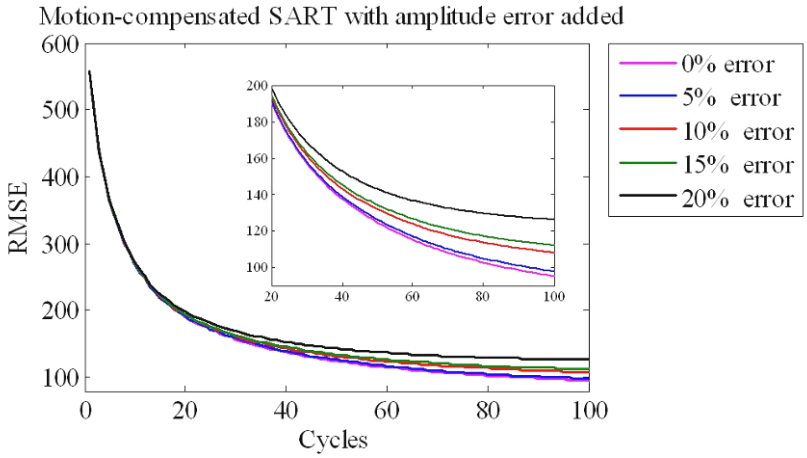

(b)

Figure 6-13 RMSE plots of the motion-compensated images using (a) ART, and (b) SART.

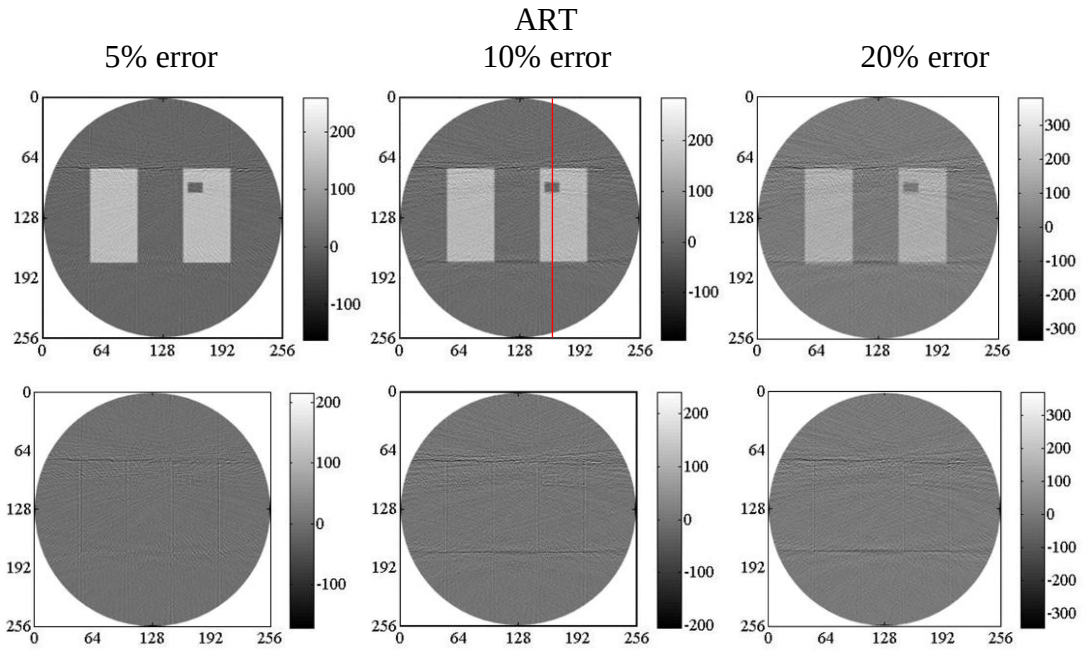

Figure 6-14 Motion compensation using ART with different percentages of amplitude error: top row is reconstructed images, bottom row is error images (the red line is 1D plot in figure 6-16).

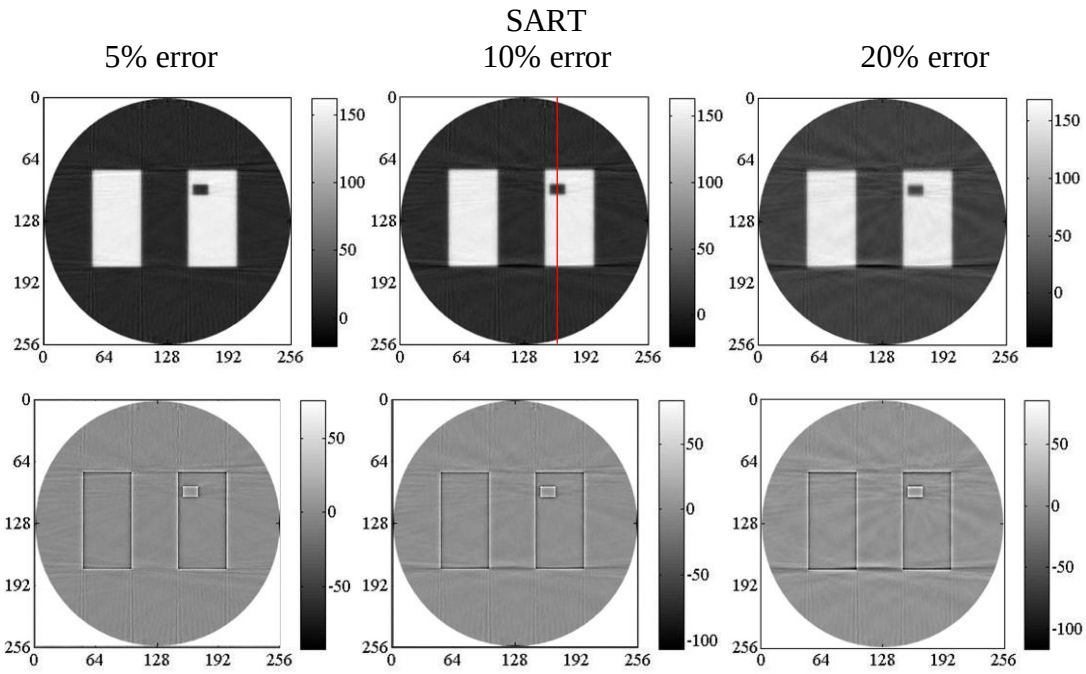

Figure 6-15 Motion compensation using SART with different percentages of amplitude error: top row is reconstructed images, bottom row is error images (the red line is 1D plot in figure 6-16).

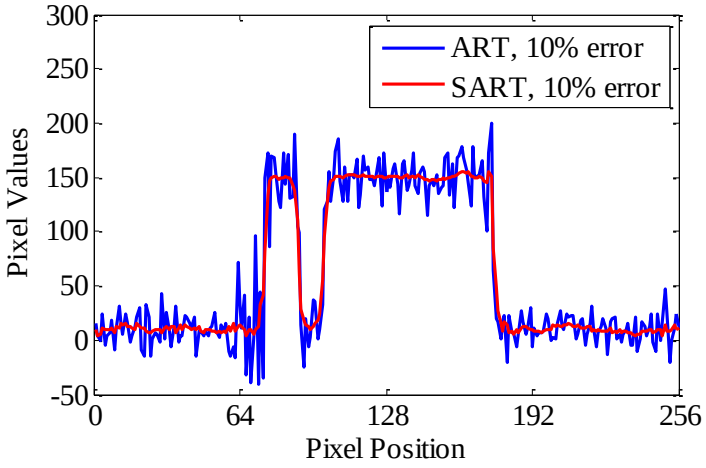

Figure 6-16 Image row plots of motion-compensated ART and SART (x=164) with 10% of amplitude error added.

6.1.5.2 Random additive Gaussian noise error

The studies of the motion compensation with the amplitude error indicated that ART produces higher level of noise than SART at the same level of motion error. The next common error type, which was examined, was random additive Gaussian error, so-called "white Gaussian noise".

The 20 mm peak-to-peak amplitude motion was corrupted by random additive Gaussian noise with standard deviation set of 5%, 10%, 15% and 20% of the 20 mm peak-to-peak amplitude of the original motion model. Figure 6-17(a) shows the motion model with various percentages of random additive Gaussian noise. The RMSE plots of the approximated motion-compensated ART and SART, when using the uncorrupted motion model, are shown in figures 6-18(a) and 6-18 b) respectively. Figures 6-19 and 6-20 shows the reconstructed images and error image of the approximated motion compensation using ART and SART. The reconstructed images of ART show higher level of noise than the reconstructed images of SART reconstruction for all level of motion error. On the other hand, the blurring artefacts can be obviously seen in error images of SART. Nevertheless, this blurring artefacts cannot be distinguished in 1D plots (figure 6-21). In comparison to the results of the amplitude (section 6.1.4), random additive Gaussian error produces a higher RMSE

than for amplitude error, at the same level of the percentage error, for ART but not for SART.

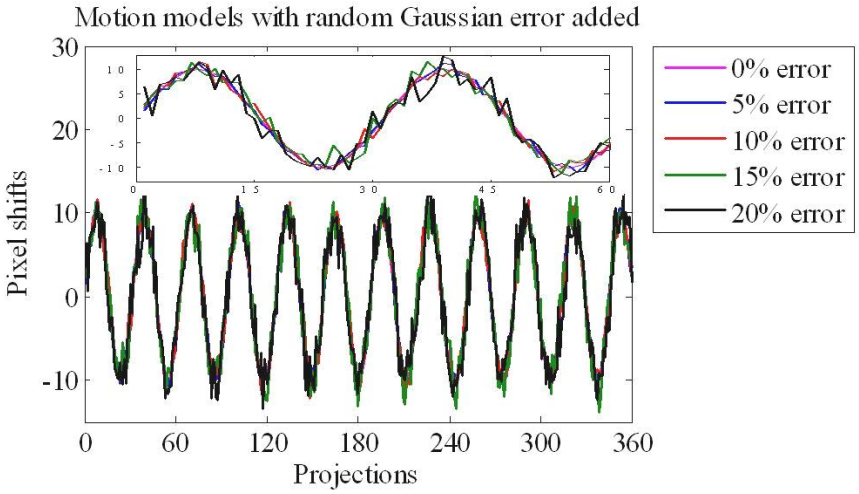

Figure 6-17 Motion models with different percentages of random additive Gaussian error.

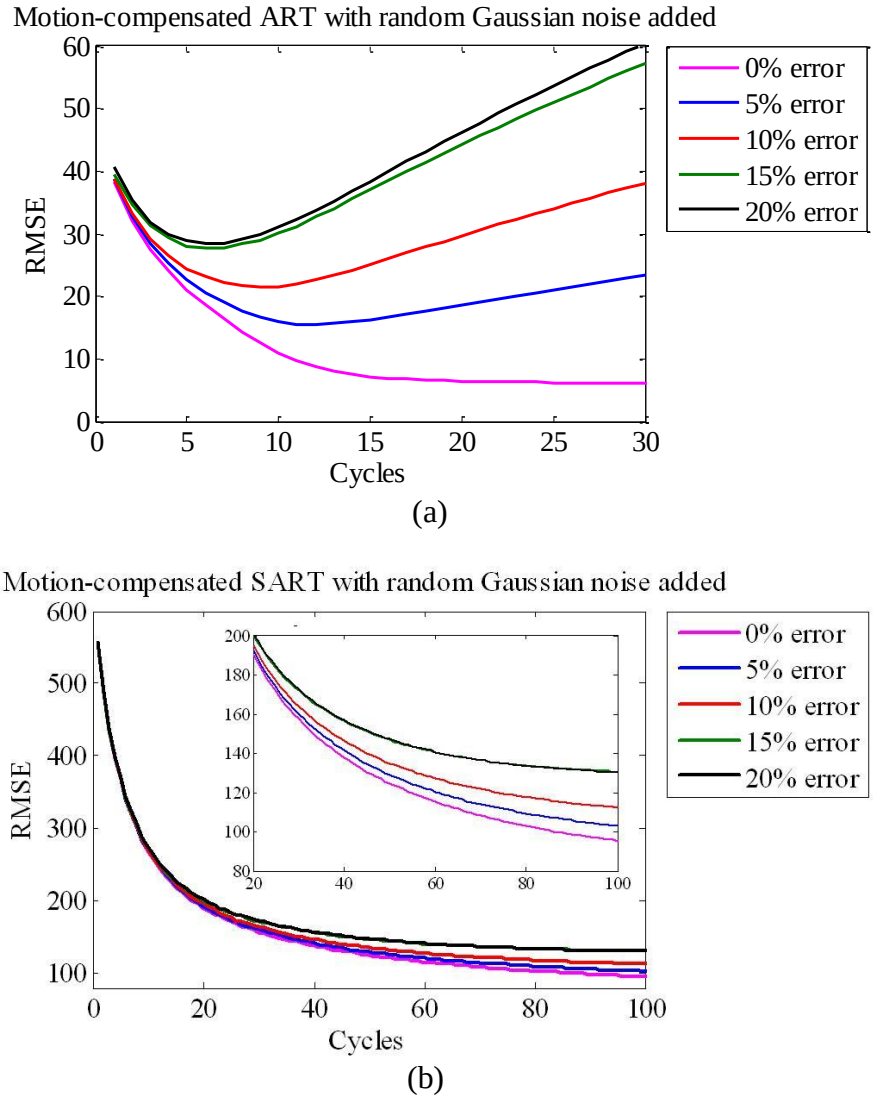

Figure 6-18 RMSE plots of motion-compensated images using (a) ART and (b) SART.

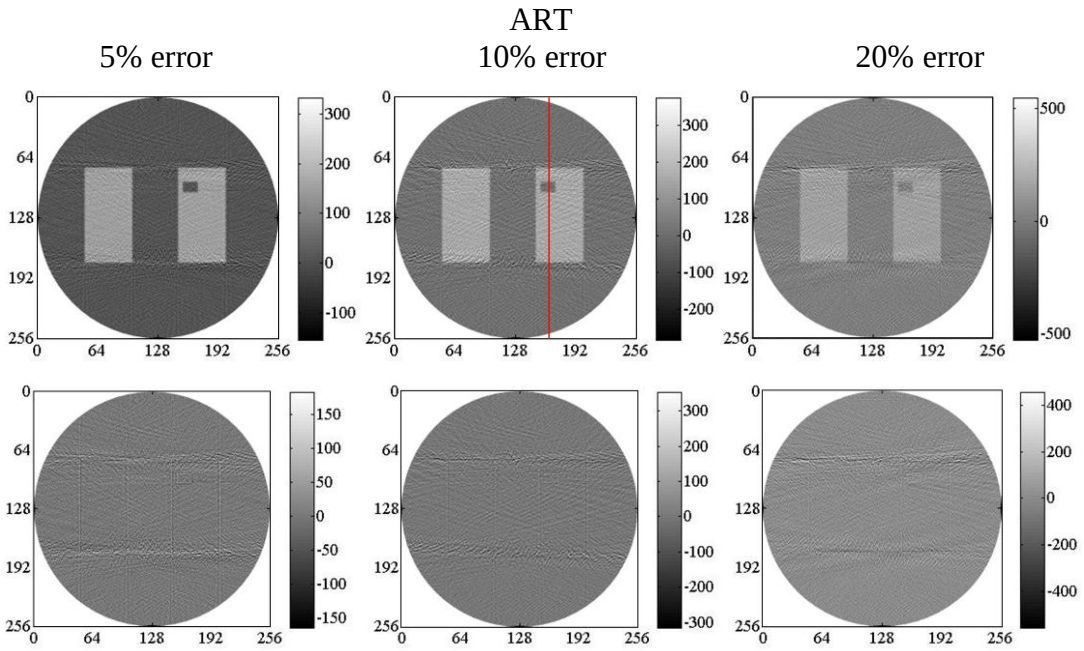

Figure 6-19 Motion compensation using ART with different percentages of random additive Gaussian error: top row is reconstructed images, bottom row is error images (the red line is 1D plot in figure 6-21).

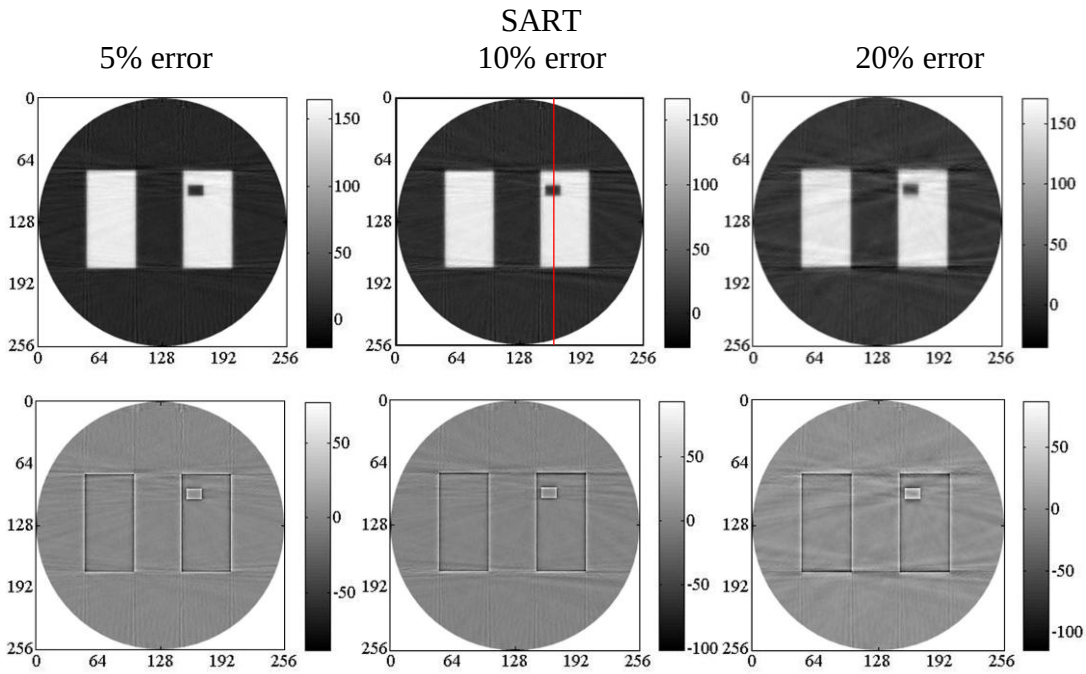

Figure 6-20 Motion compensation using SART with different percentages of random additive Gaussian error: top row is reconstructed images, bottom row is error images (the red line is 1D plot in figure 6-21).

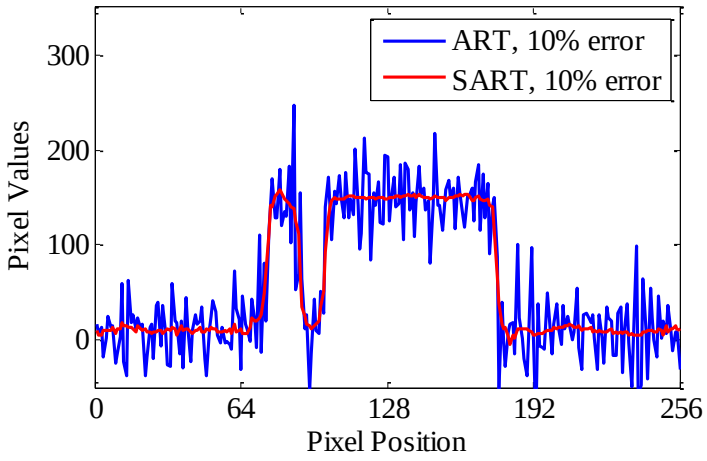

Figure 6-21 Image row plots of motion-compensated ART and SART (x=164) with 10% of random additive Gaussian error added.

6.1.5.3 Phase error

The motion model with phase error was produced in particular from 2% to 20% (stepped by 2%) of a complete cycle of the original motion model (figure 5-3). The resulting motion models, with different phase errors, are shown in figure 6-22. Figures 6-23(a) and (b) are the RMSE plots of the approximated motion-compensated ART and SART under different phase errors. The reconstructed images, using the approximated motion compensation, are shown in figure 6-24 for ART and figure 6-25 for SART. It can be seen in the reconstructed images of the motion phase error study that, at the same level of percentage error, ART seems to be more sensitive to phase error than SART by showing higher image noise artefacts. At 20% of phase error added, the reconstructed images of both ART and SART show almost corrupted by the motion. This implies that the motion compensation has limited efficiency to recover the motion artefacts, when the estimated motion is not accurate in the phase. Figure 6-26 is an example of 1D plot running through reconstructed images of ART and SART at 10% phase error added. It is difficult to distinguish the edges of objects by these plots. However, ART and SART show the same general trends; the higher the percentage of phase error, the greater the resulting image error.

The amplitude error study and the random additive Gaussian error study show that an increasing in the phase error leads to an increase in the RMSE, blurring effect and image noise at the end of the updates for both ART and SART. In the comparison to the studies of the amplitude error and the random additive Gaussian error, at the same level of error, the phase error produces higher RMSE than the study of the amplitude and the study of the for both ART and SART.

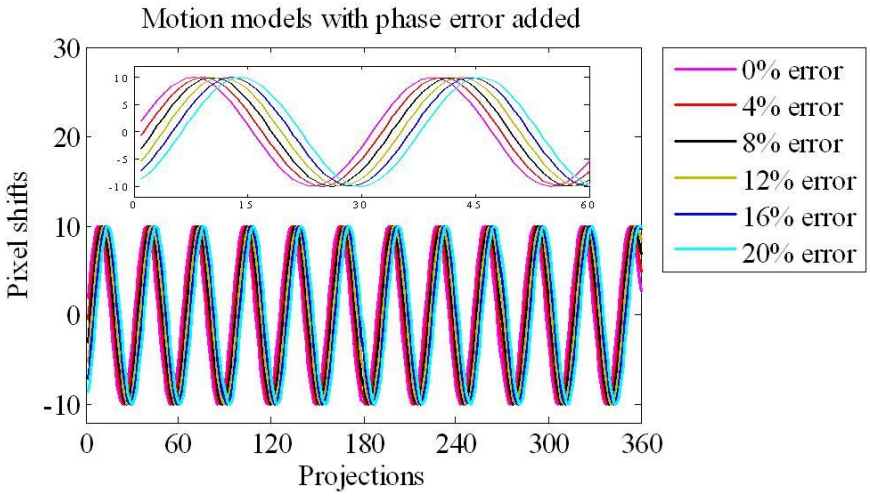

Figure 6-22 Motion models with different percentages of phase error.

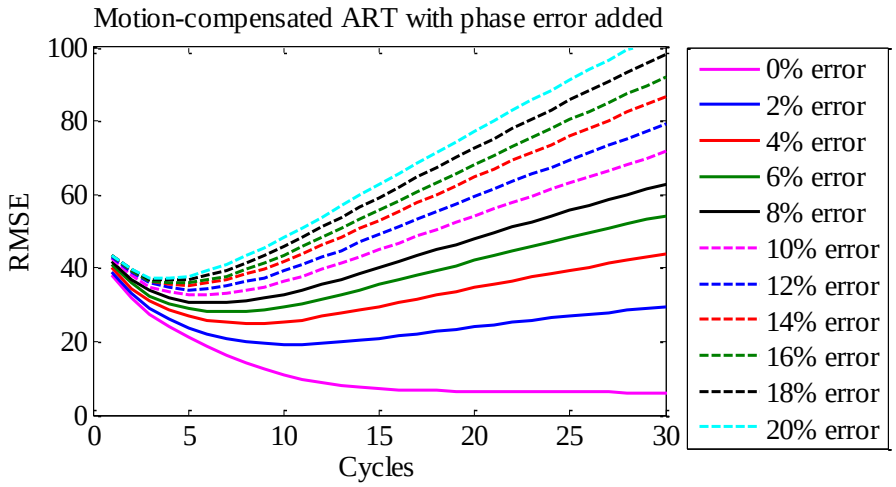

(a)

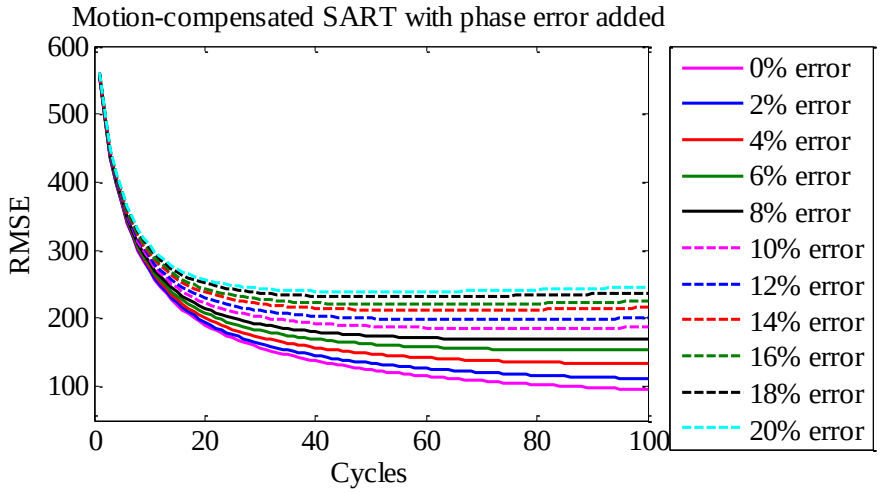

(b)

Figure 6-23 RMSE plots of motion-compensated images using (a) ART and (b) SART.

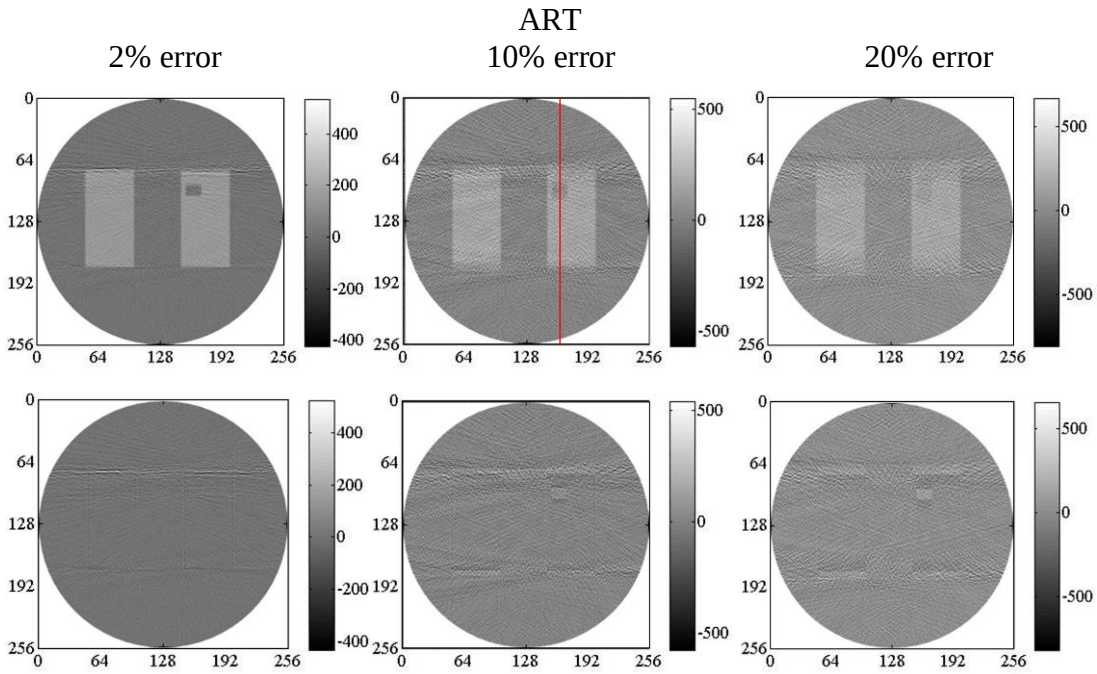

Figure 6-24 Motion compensation using ART with different percentages of motion phase error: top row is reconstructed images, bottom row is error images (the red line is 1D plot in figure 6-26).

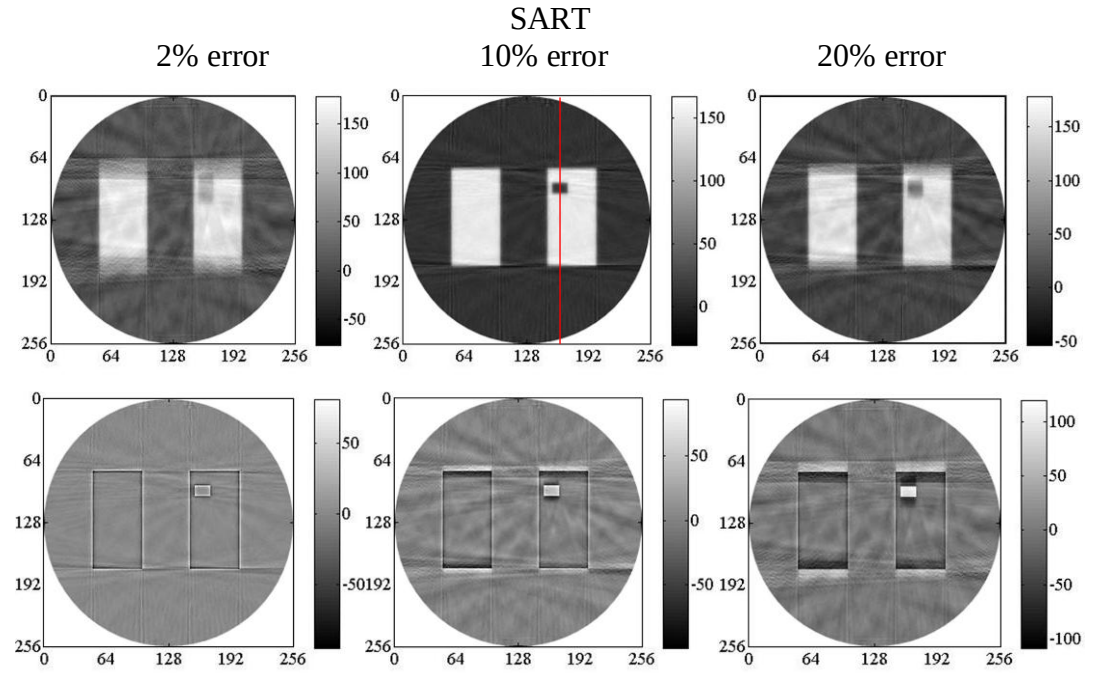

Figure 6-25 Motion compensation using SART with different percentages of motion phase error: top row is reconstructed images, bottom row is error images (the red line is 1D plot in figure 6-26).

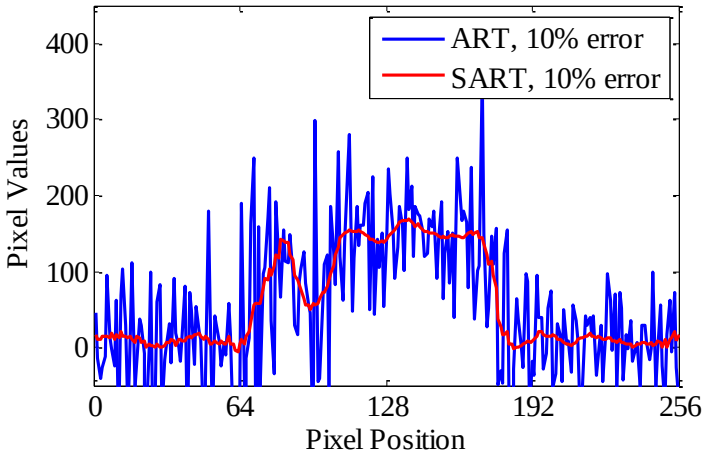

Figure 6-26 Image row plots of motion-compensated ART and SART (x=164) with 10% of phase error added.

6.1.6 Summary

Among the 3 types of motion errors, the approximated motion compensation was more sensitive to phase error than amplitude or random additive Gaussian error. Moreover, these results suggest that motion-compensated SART has a greater capability to compensate for motion than motion-compensated ART, even with a less accurate motion model applied during compensation. Of course, it is expected that the performance of the motion compensation technique will degrade as the motion model becomes more inaccurate. However, it is important to note that there is more than one method to compensate for motion, and the results presented here are applicable to our specific method as described in section 3.3.

6.1.7 Three-dimensional study

A 3D simulated phantom (figure 5-1) with ($256\times256\times256$) pixels was used in this experiment. Where appropriate, relevant lines or planes are indexed using pixel coordination x,y,z $\in$ [1,256]. To reconstruct this phantom, the correct motion-compensated SART with one-fourth data set reconstruction was used for 100 cycles and $\alpha = 0.01$. The 20 mm peak-to-peak amplitude motion model (figure 5-3) was applied to the phantom in the z direction (SI direction in the real situation) and the projection data collected. Then the correct motion model was used for motion

compensation during the iterative reconstruction. Slices of the true image and the motion-compensated image are shown in figures 6-27(a) and (b), and image row plots running through the middle of the small rectangular hole is shown in figure 6-27(c). Ray-path artefacts can be seen in the motion-compensated image in figure 6-27(b), especially aligned with certain of the boundary edges. This might be due to high contrast between objects and background. The image row plots show that the correct motion-compensated SART almost converges to the true phantom. However, the noise can also be seen on the plots.

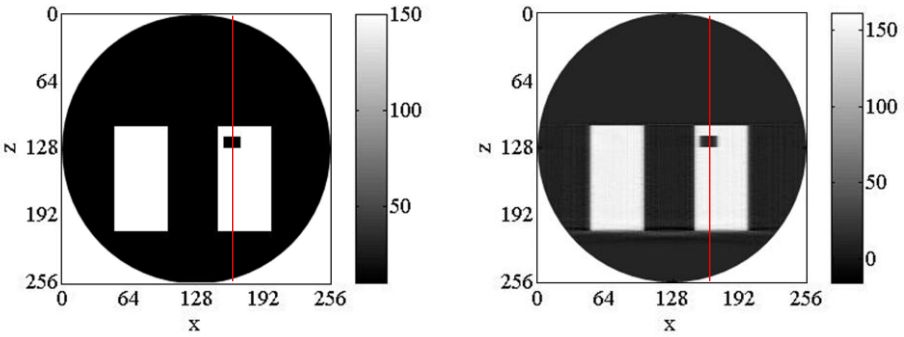

(a) (b)

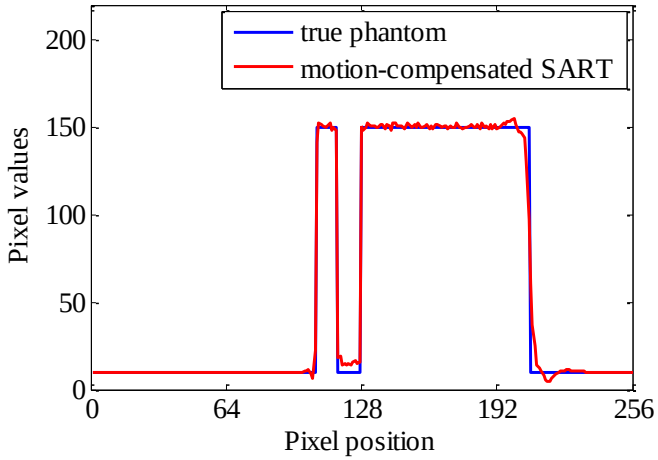

(c)

Figure 6-27 (a) Reconstructed image using SART in the plane at y=95 for the true phantom, and (b) motion-compensated image in the plane at y=95 for the moving phantom; (c) Image row plots of (a) and (b) at (x=162, y=95).

6.2 CGLS reconstruction

Reconstructions using the CGLS algorithm for the motion-compensated CBCT were investigated in this study. The first experiment was the reconstruction of consistent and inconsistent cases. Then, regularised CGLS for the inconsistent case, the correct motion compensation and the approximated motion compensation were later established.

6.2.1 CGLS reconstructions for consistent and inconsistent cases

To test the performance of the CGLS algorithm for reconstructing the CBCT images, CGLS reconstruction for the consistent case was first evaluated. The inconsistent data used in section 6.1.2 was examined for the CGLS reconstruction.

The results of the CBCT reconstruction using the CGLS algorithm for the consistent case and inconsistent case are shown in figure 6-28, 6-29, and 6-30. Figure 6-28 shows the RMSE plots for both cases. For the CGLS reconstruction, the behaviour of bulk cases and inconsistency were similar, for the first few iterations. After about the 12^{th} iteration, the reconstruction of the consistent case remains steady, but, for the inconsistent case, the reconstruction after the 8^{th} iteration has diverged. The reconstructed images at the 1^{st} and the 12^{th} iteration of the consistent case are shown in figures 6-29(a) and (b); and the reconstructed images at the 1^{st} and the 12^{th} iteration of the inconsistent case are shown in figures 6-29(c) and (d), respectively. These results clearly show the limited improvement of the CGLS reconstructions for the consistent case after the 12^{th} iteration, which remain steady. Error images of these images are shown in figure 6-30. The inconsistent case produces higher noise than then consistent case, then the blurring edges can be visible in the consistent case more clearly than the inconsistent case.

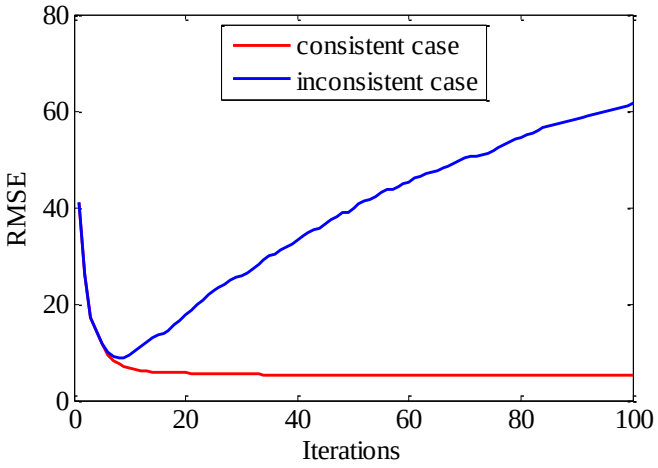

Figure 6-28 RMSE plots using CGLS reconstructions for consistent case and inconsistent case.

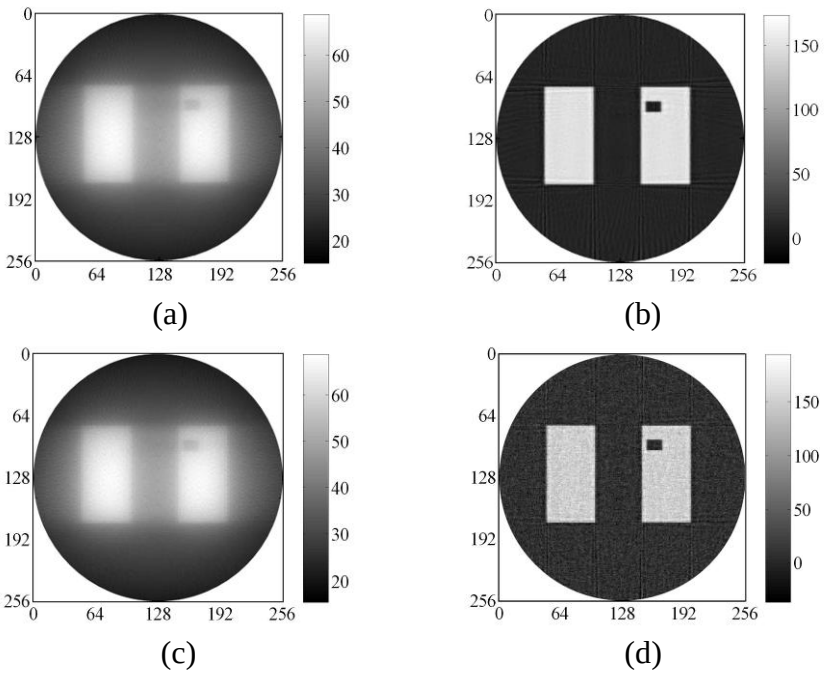

Figure 6-29 Reconstructed images at (a) the 1st iteration of consistent case, (b) the 12th iteration of consistent case, (c) the 1st iteration of inconsistent case and (d) the 12th iteration of inconsistent case.

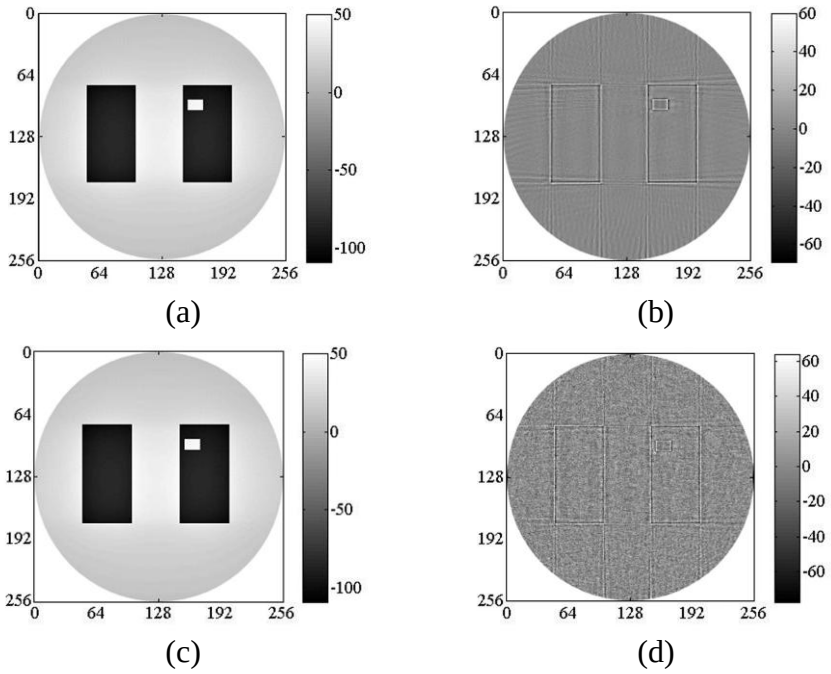

Figure 6-30 Error images of figure 6-29.

6.2.2 Regularised CGLS for inconsistent case

Due to the divergence after a few iteration of the inconsistent case reconstruction, the regularised CGLS was examined in this study. The variation of regularisation parameter γ was also investigated. The inconsistent case from in section 6.1.2 was used.

Figure 6-31 shows RMSE plots of unregularised CGLS and regularised CGLS with different values of the regularisation parameter γ. The RMSE plots show that the appropriate γ value can reduce the divergence effects of CGLS reconstruction for the inconsistent case. The reconstructed images, after the 12^{th} iteration, and error images with various γ values are shown in figure 6-32. In this study, γ =10 gives the best convergence compared to unregularisation and regularisation with γ={1, 100}. However, errors at the edges of the error image for γ =10 can be noticeable. In conclusion, the regularisation with an optimal regularisation parameter has a feasibility to keep the convergence of CGLS reconstruction for inconsistent case steadily after the 12^{th} iteration. However, in this study the 12^{th} iteration was chosen for the motion-compensated CGLS in order to keep the computational time minimal.

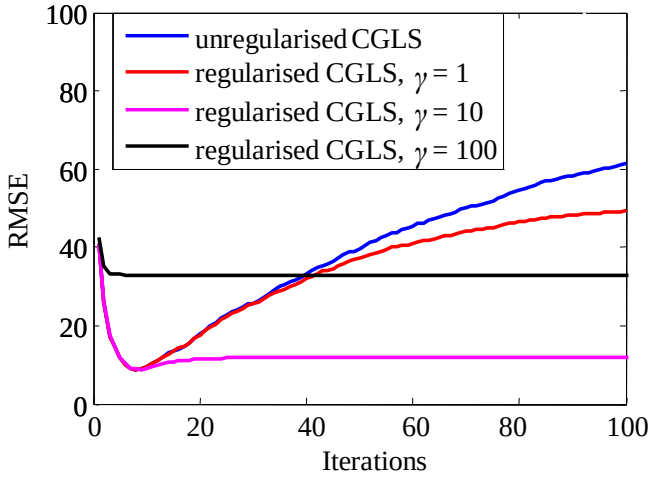

Figure 6-31 RMSE plots using unregularised CGLS and regularised CGLS with $\gamma \in \{1, 10, 100\}$.

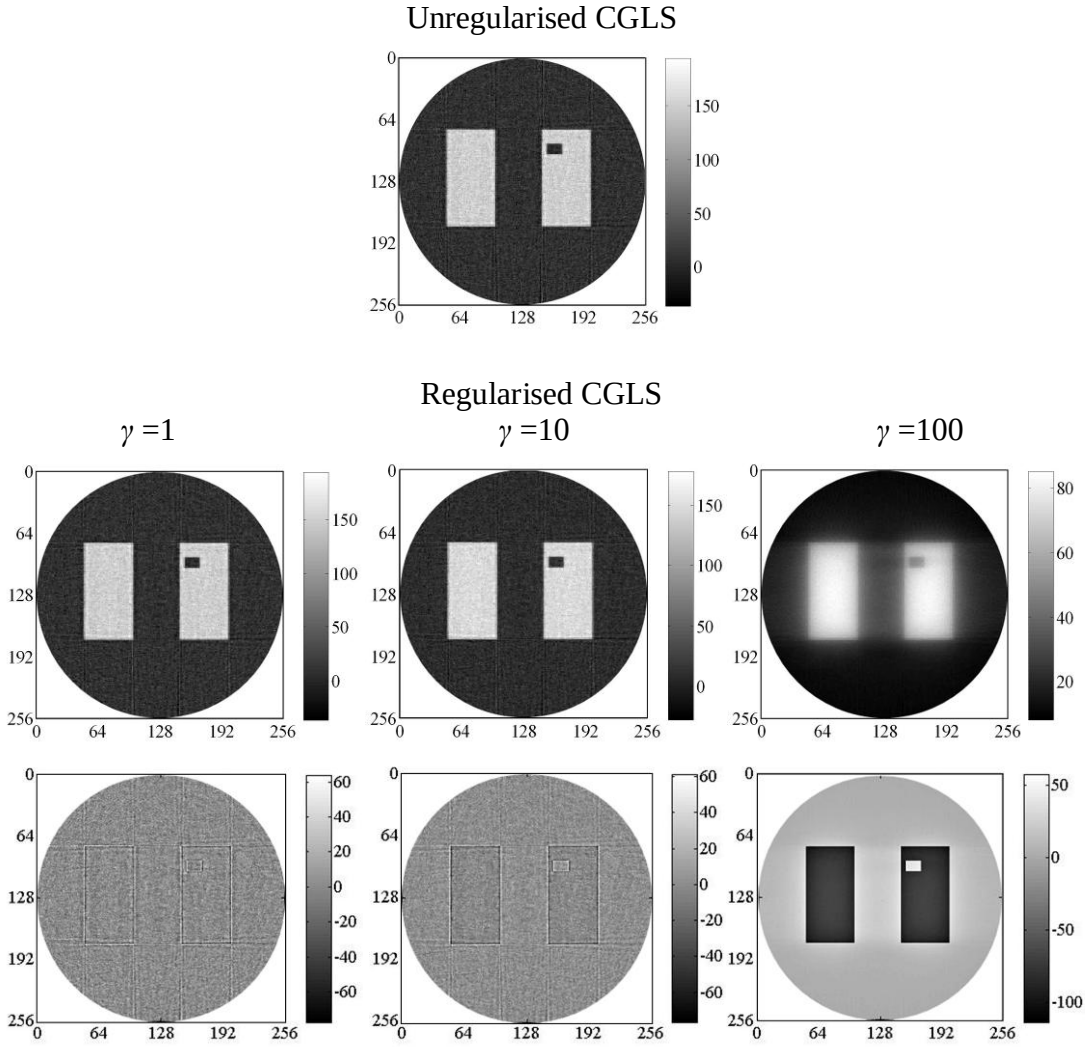

Figure 6-32 Reconstructions of unregularised CGLS, regularised CGLS with $\gamma = \{1,10,100\}$: top row is reconstructed images, bottom row is error images.

6.2.3 Correct motion compensation using CGLS

For the correct motion-compensated CGLS, a moving phantom was created by shifting the simulated phantom with the 20 mm peak-to-peak amplitude of the sinusoidal model (figure 5-3) in the up/down direction. The same motion model was also used for the motion compensation.

The RMSE plots of the reconstructed images when no motion is applied, when motion is applied but no motion compensation, and motion is applied with motion compensation is used are shown in figure 6-33. The plot of the motion-compensated

CGLS, using the correct motion model, shows the recovery to the image reconstruction when no motion is applied. When the motion is applied into data acquisition process, the reconstructed image shows motion blur artefacts, which can be easily seen in figure 6-34. The motion-compensated image shows an improvement in blurring artefacts due to motion. The results here suggest that the motion-compensated CGLS has capability to accommodate with motion blur artefacts in CBCT image reconstruction.

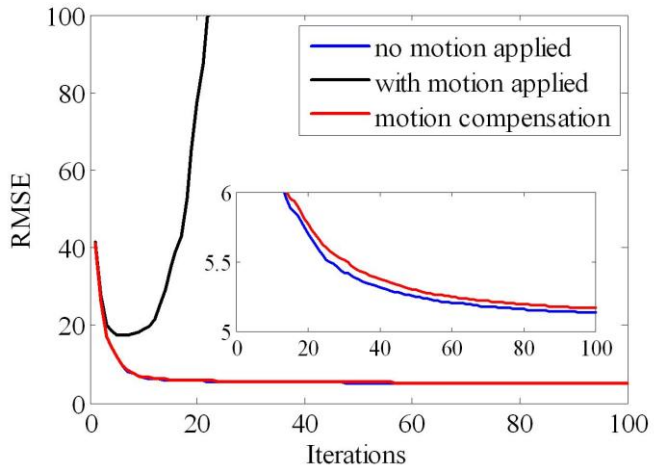

Figure 6-33 RMSE plots using correct motion-compensated CGLS.

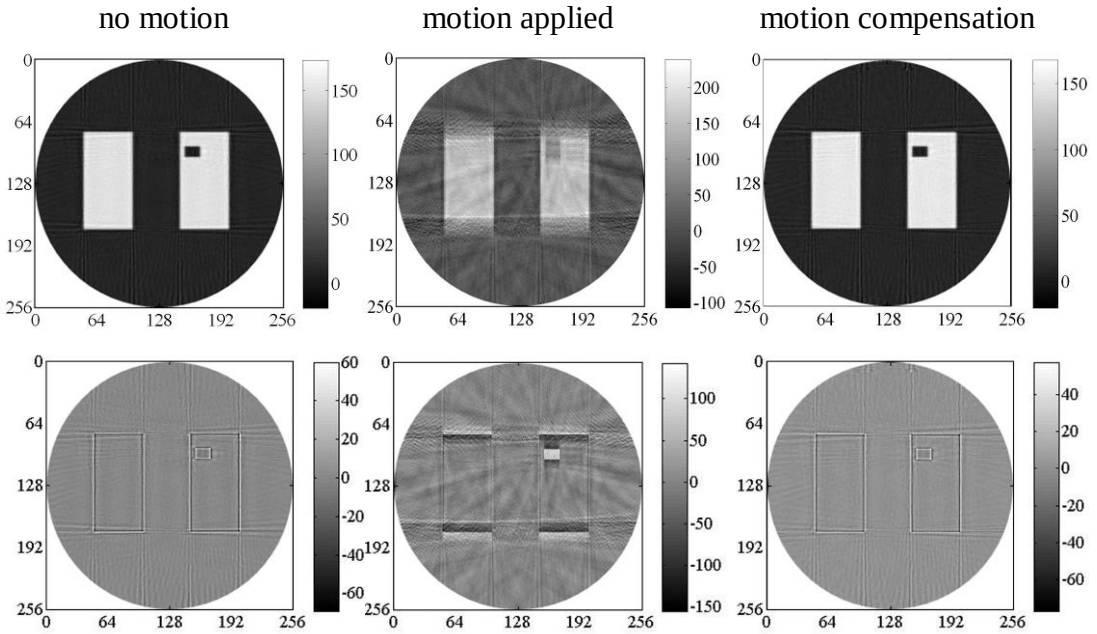

Figure 6-34 CGLS reconstructions when no motion applied, motion applied but no motion compensation applied, and motion compensation applied: top row is reconstructed images, bottom row is error images.

6.2.4 Approximated motion-compensation using CGLS

The approximated motion-compensated CGLS, when the motion with motion errors is applied, was subsequently investigated. Three types of motion errors (amplitude error, Gaussian error, and phase error) with different percentages of error were added into the 20 mm peak-to-peak amplitude of the sinusoidal model. For amplitude error, 5%, 10%, 15% and 20% of the 20 mm peak-to-peak amplitude of the motion model were applied. Next, the motion models with random additive Gaussian noises were created by adding Gaussian noise with the standard deviation set to 5%, 10%, 15% and 20% of the 20 mm peak-to-peak amplitude of the motion model. Finally, phase errors were generated by using the range of 2% to 20% with 2% interval of a complete cycle of the motion model. The motion models with various types and percentages of error are the same as in section 6.1.5. These motion models with errors were used to shift the phantom when collecting projection data.

Figure 6-35 shows the RMSE plots of the reconstructed images when motion error applied and the approximated motion-compensated CGLS is used. Figure 6-36 shows

the motion-compensated images after the 12^{th} iteration when no motion error is added and when various types of motion errors with 20% of the motion model added. The RMSE plots show that an increasing in percentages of the motion error results in an increased RMSE for all types of error. Phase shifting produces higher artefacts to the motion-compensated CGLS when compared to amplitude and Gaussian error. This can be seen in the reconstructed images shown in figure 6-36. Figure 6-37 is error images between the figure 6-36 and the true phantom. These error images confirm that the phase error produce higher image noise and also higher remaining artefacts after compensating when compare with the amplitude error and the random additive Gaussian at the same level of error. These results and the results obtained from the approximated motion-compensation for ART and SART in section 6.1.5 suggest that the motion compensation technique developed in this study is more delicate to the phase error than to the amplitude error and the random additive Gaussian error.

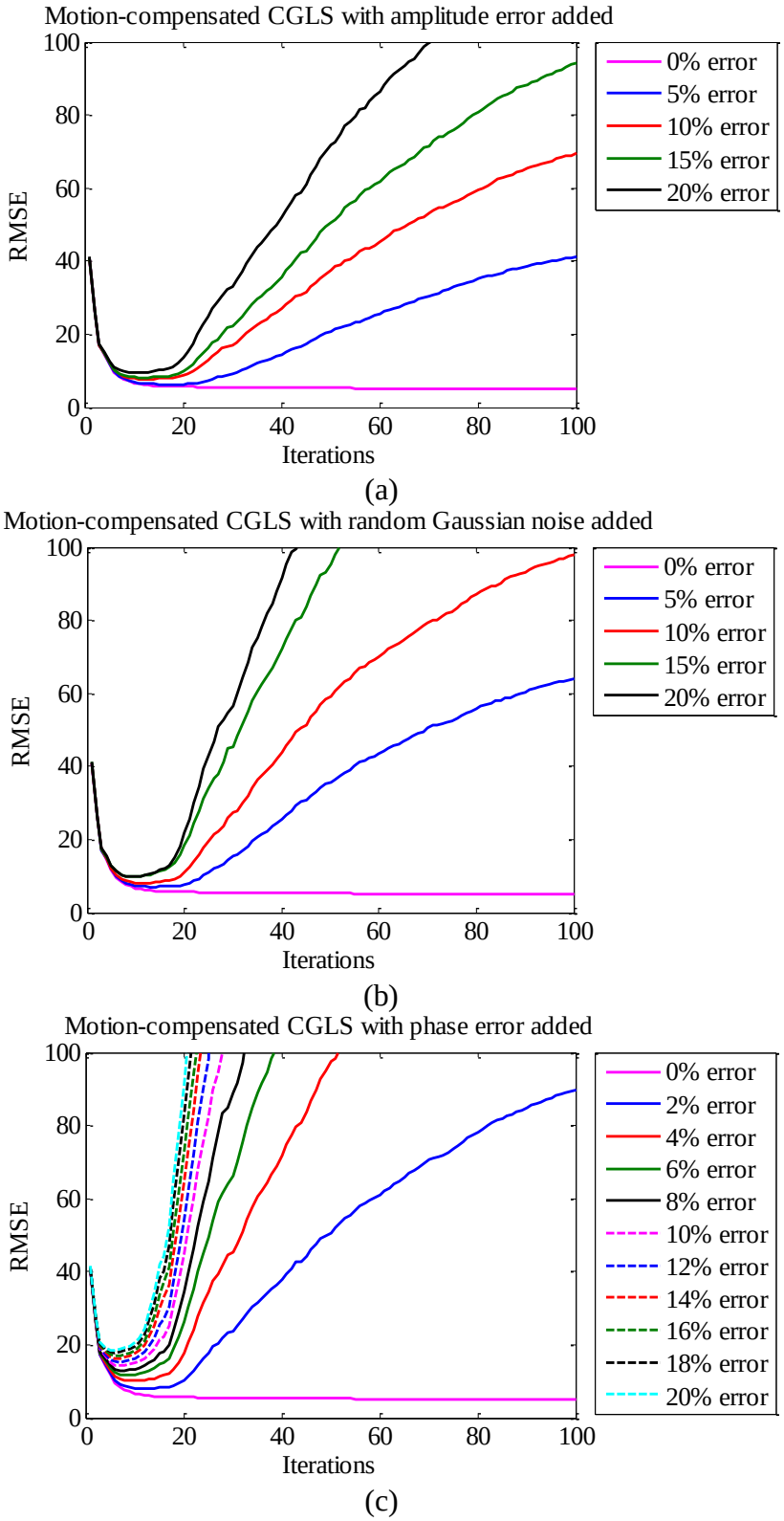

Figure 6-35 RMSE plots of approximated motion-compensated images when different percentages error added for (a) amplitude error (b) random additive Gaussian error, and (c) phase error.

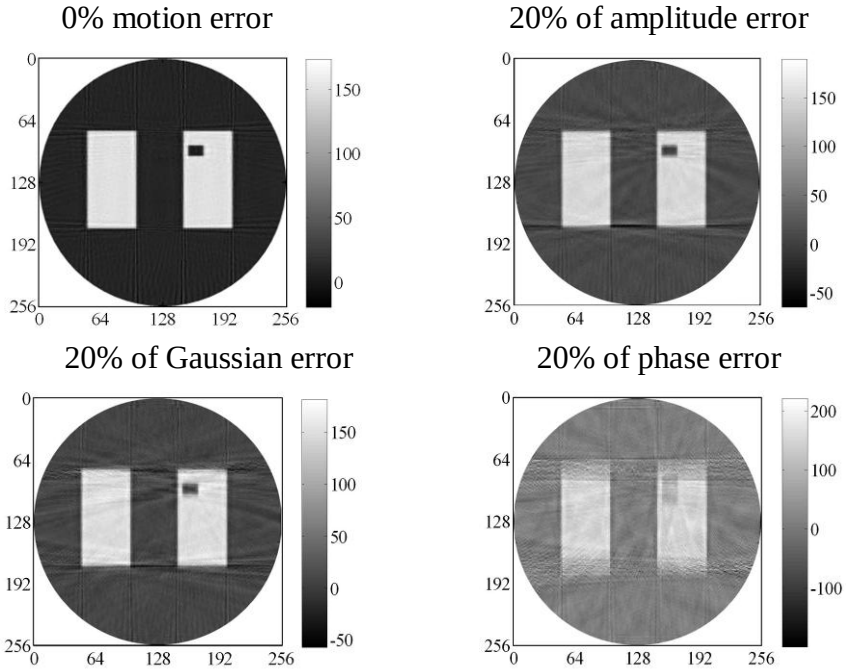

Figure 6-36 Reconstructed images of 0% motion error, 20% of amplitude error, 20% of Gaussian error, and 20% of phase error.

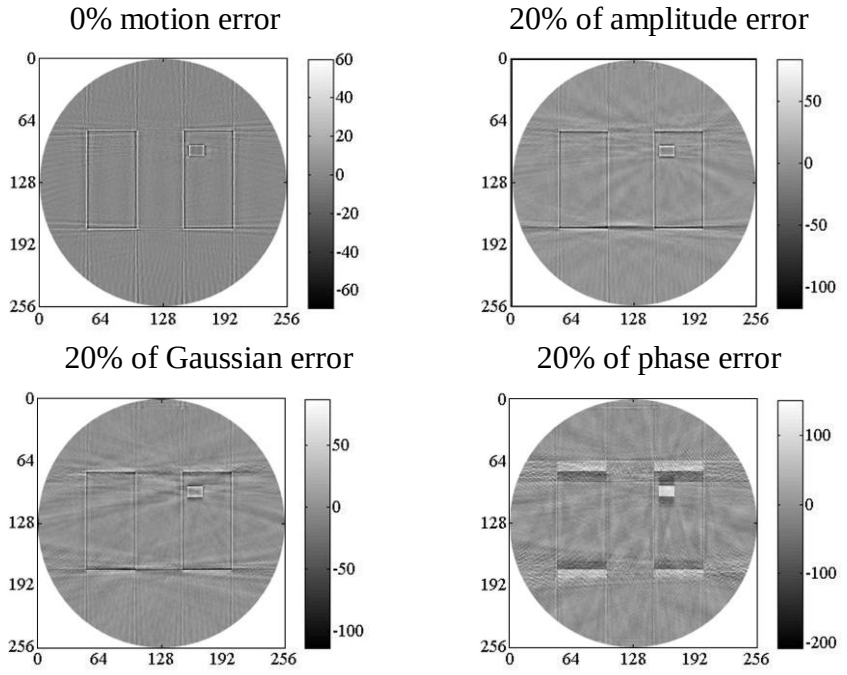

Figure 6-37 Error images of figure 6-36

6.3 Discussion

In medical imaging, there is a lot of interest in limited data reconstruction, since this allows a reduction in the radiation dose to patients. The iterative algebraic reconstruction techniques such as ART, SART, and OS-SART, are known to be suitable. Moreover, the CGLS technique has been recently introduced to CBCT reconstruction. However, motion artefacts are still problematic in practice. Thus, the CBCT reconstruction with limited data was investigated using the motion-compensated ART, SART, OS-SART, and CGLS. The experiments showed the feasibility of the motion compensation to reduce blurring artefacts caused by motion, especially for the correct motion compensation. The approximated motion-compensated ART, SART, and CGLS were also studied to investigate the performance, when various types of error were applied to the motion model when collecting projection measurements, but not during reconstruction. The results suggest that the motion-compensated ART is more sensitive to such motion error than the motion-compensated SART or CGLS by producing higher noise. In general, the motion-compensated reconstruction algorithms were more sensitive to phase error than to amplitude error or random additive Gaussian error. For motion compensation in medical applications, the results here suggested that the accuracy of respiratory phase detection may be more important than the accuracy of respiratory amplitude detection.

Moreover, this chapter also presents the motion-compensated CBCT with limited data using CGLS reconstruction algorithm. The CGLS is a superior iterative method compared to Kaczmarz's type methods (ART, SIRT, and SART), in terms of the speed of convergence, is well suited for high performance computations, and possibility of including the regularisation and a priori knowledge in image reconstruction process. The results of the motion-compensated CGLS suggested that this algorithm can improve blurring artefacts on reconstructed images.

6.4 Conclusions

To verify the motion compensation technique developed in this study combined with the limited data reconstruction, a set of simulated experiments were carried out. The motion-compensated ART, SART, OS-SART and CGLS with one-fourth data reconstruction were examined for the consistent and inconsistent case, the correct motion compensation, and the approximated motion compensation (amplitude error, random additive Gaussian error, and phase error added into the motion model for moving the phantom).

The results of the consistent and inconsistent cases showed similarity for ART and CGLS which the RMSE plots for the inconsistent case diverged after few cycles for ART and few iterations for CGLS but not for the consistent reconstruction. Compared with SART and OS-SART, the reconstruction of CGLS kept iteratively updating for few cycles, and then the convergences kept steadily through 100 cycles.

The correct motion compensation experiment for all ART, SART, OS-SART and CGLS suggested that the developed motion compensation technique has a performance to account for the motion artefacts in CBCT reconstruction. The convergences showed the recovery to the static phantom reconstructions.

The approximated motion compensation experiments indicated that the accuracy of motion estimation is an important factor for the motion compensation. Among three types of error, the phase error produced the blurring artefacts on the motion-compensated image rather than the amplitude error and the random additive Gaussian error. Moreover, the results suggested that the motion-compensated ART produces higher level of noise than the motion-compensated SART and CGLS.

It can be concluded that the developed motion-compensation technique has a capability to reduce the blurring artefacts on the CBCT images. The performance of the motion compensation technique depends on the accuracy of the motion estimation particularly for motion's phase accuracy. To achieve the aim of this study,

a combination of the motion-compensated CBCT using the motion model extracted from EIT images was investigated in the next chapter.

Chapter 7
Dual Modality CBCT and EIT

A main objective of this study was to combine two imaging systems of the EIT and the CBCT, to take an advantage of the high temporal resolution of EIT and the high spatial resolution of CBCT for the purpose of motion compensation. The proposed study used a dual modality: the EIT system that can be developed by patient specific model, and the motion-compensated CBCT that is taking the motion information from the EIT system.

7.1 Motion-compensated ART with full data reconstructions using motion model extracted from EIT images

7.1.1 Motion extraction from EIT images

A phantom, consisting of two spherical objects of 25 mm radius, was produced and moved by 40 mm peak-to-peak amplitude of motion in the up/down direction while being imaged by the EIT system in a simulation environment. A 16 electrode EIT system including four planes of eight electrodes was modelled with an adjacent current pattern. The contact impedance z_l was 0.004, the background electrical conductivity was 1 S/m and the spherical inclusions have conductivity of 0.1 S/m. The assumption was that the full EIT image can be generated for each projection of the CBCT data. Figure 7-1 shows the EIT images at different times, when the spheres were in different locations. The first EIT image in the sequence was used as a reference for motion data and the motion was tracked in subsequent images. The

motion model extracted from the EIT images is shown in figure7-2, where it is compared to the true motion model. The true motion model generated for the CBCT phantom was sinusoidal model with a 40 mm peak-to-peak amplitude. When comparing the true motion model and the motion model extracted from the EIT images over approximately 11-and-a-half cycles, the root mean square difference was about 1.42 mm, and the maximum absolute difference was 3.62 mm. The motion model extracted from the EIT images was then used in motion compensation for CBCT reconstruction.

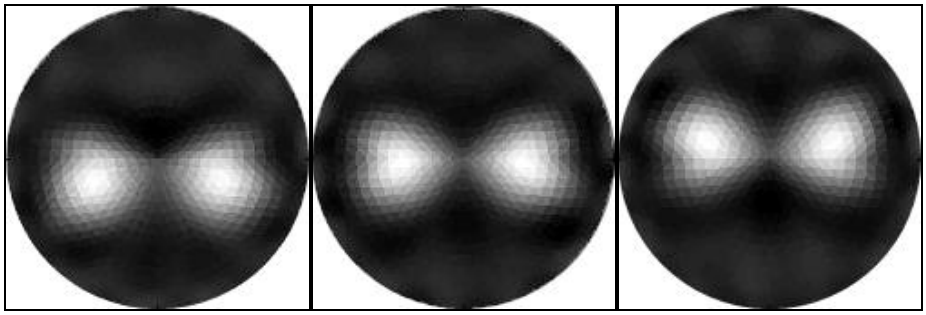

(a) (b) (c)

Figure 7-1 EIT images of spherical objects at (a) the lowest position, (b) the original position and (c) the highest position.

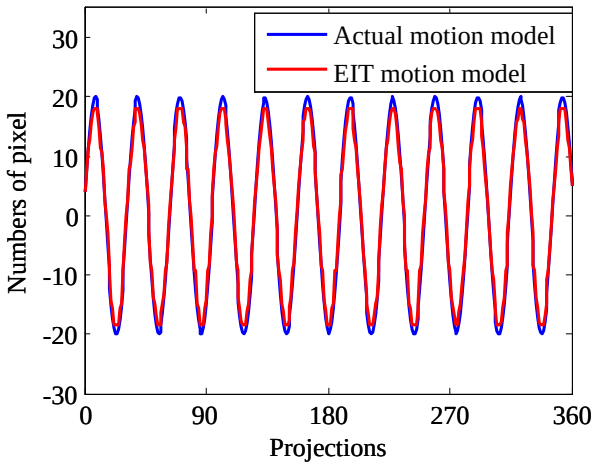

Figure 7-2 Actual motion model and motion model extracted from EIT.

7.1.2 Motion-compensated ART using EIT motion model: simulation study

The phantom with two spherical objects was also used for the CBCT reconstruction. The phantom was moved by a 40 mm peak-to-peak sinusoidal motion model in the up/down direction. The projection data were collected over 360 degrees for the full data set reconstruction. The motion-compensated ART with 40 cycles and $\alpha = 0.3$ were used in this experiment.

The RMSE plots of motion-compensated ART when EIT motion model is used are shown in figure 7-3. From these plots, the reconstruction when motion is applied shows higher image error than when no motion is applied and when motion is applied with motion compensation is used.

The top row of figure 7-4 is the CBCT images of two spheres when no motion is applied, when motion is applied, and when motion is applied with motion compensation is used. The motion-compensated image is produced through using the motion extracted from the EIT images. The error images are shown in the bottom row of figure 7-4. It can be seen that image blur is clearly reduced in the image with the motion compensation, compared with the uncompensated image. The boundaries of spherical objects on the motion-compensated image are sharper than the boundaries of those in the uncompensated image. The image row plots for CBCT images through the centre of the left sphere (x = 68) are shown in figure 7-5. The plot of the motion-compensated CBCT image has a sharper edge than the plot of the uncompensated image and it is closer to the CBCT image obtained when no motion is applied. This shows the feasibility of reducing the motion blurring effect by using the motion model extracted from the EIT image to the motion-compensated CBCT.

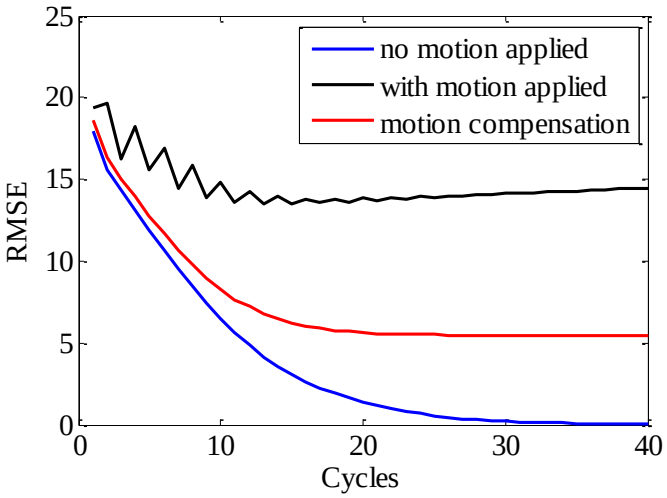

Figure 7-3 RMSE plots of motion-compensated ART when EIT motion model is used.

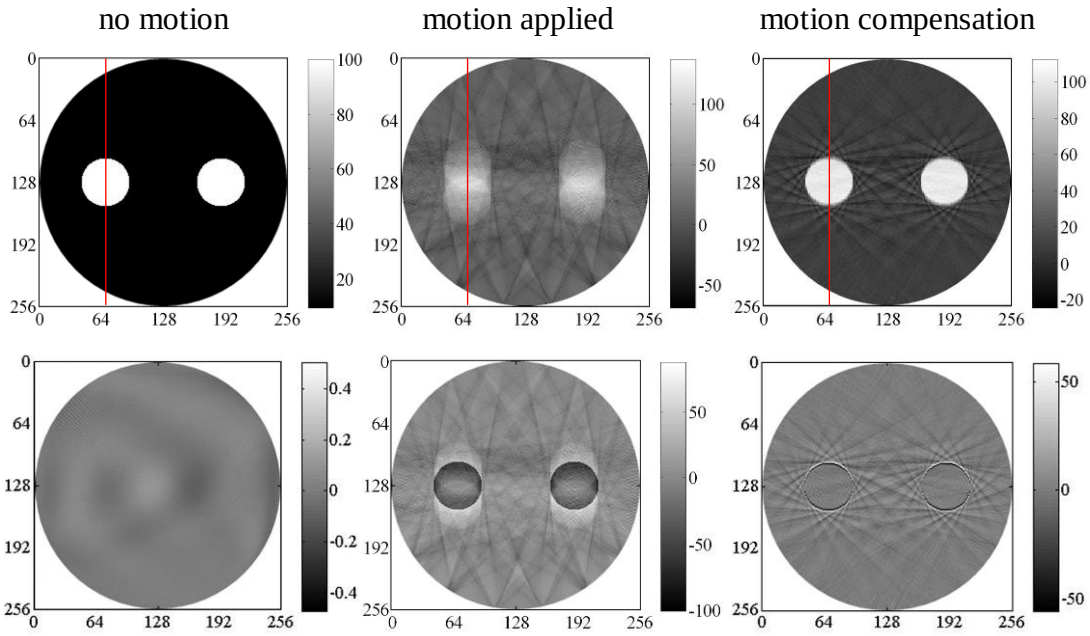

Figure 7-4 Full dataset, ART reconstructions of two spheres when no motion appiled, 40 mm of motion applied in the up/down direction but no motion compensation, and approximated motion compensation using EIT motion model applied: top row is reconstructed images, bottom row is error images (the red lines are 1D plot in figure 7-5).

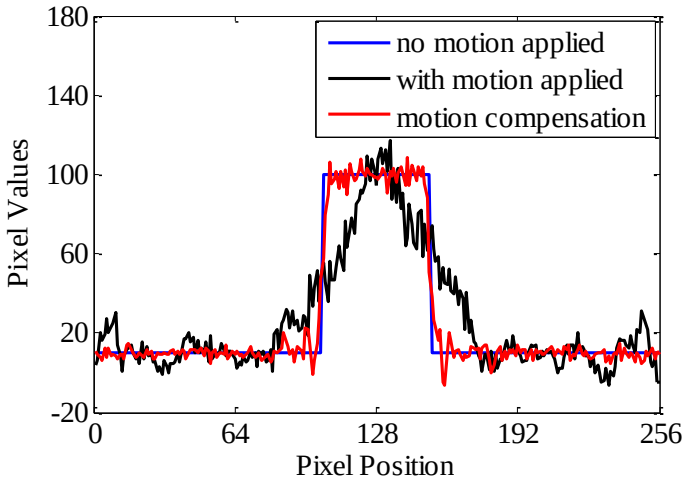

Figure 7-5 Image row plots of reconstructed images (figure 7-4: top row) at the centre of the left sphere (x=68).

The image row plots of the motion compensation all show improved edge sharpness on the motion-compensated image using the EIT motion model. However ray-path artefacts are still visible in the reconstruction in figure 7-4; this is probably an artefact of the ART algorithm.

7.1.3 Motion-compensated ART using EIT motion model: experimental/simulation study

To demonstrate the concept of the proposed CBCT-EIT system, the 16 electrode EIT system built in a LabVIEW environment based on National Instruments (NI) cards with the regularisation parameter $\gamma = 0.001$ was used. A 25 mm radius cylindrical object was moved in the up/down direction within an EIT imaging area (figure 7-6). The cylindrical object was moved in 10 mm increments, first to give 20 mm displacement, then 60 mm displacement. These experiments were all performed in a 2D imaging mode.

The simple motion extraction technique, as described in section 4.2, was used to extract the object's motion from experimental EIT images. The CBCT projection data were generated by a computer model, which incorporated the observed motion. The observed motion was recorded with measurements during the experiment.

However, the motion used in the motion compensation algorithm was extracted from the sequence of EIT images.

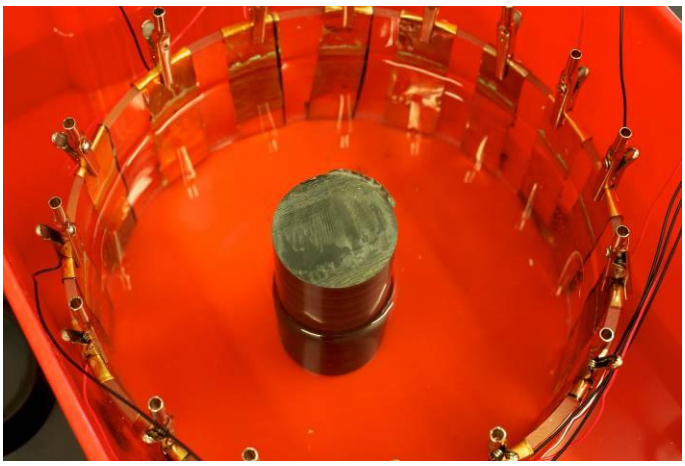

Figure 7-6 EIT phantom with a tank of 230 mm diameter

First, a 20 mm displacement was applied. Example images of a sequence of the EIT reconstructions, which were used for the motion compensation, are shown in figure 7-7. Figure 7-8 is the RMSE plots of the reconstruction when no motion is applied, when motion is applied, and when motion is applied with motion compensation is used.

The different CBCT reconstructions are shown in top row of figures 7-9 for no motion is applied, when motion is applied, and when motion is applied with motion compensation is used. The bottom row of figure 7-9 is error images resulting from subtracting the reconstructed images from the true phantom. Figure 7-10 shows image row plots running through the centre of the object of figures 7-9 (top row) at x=128.

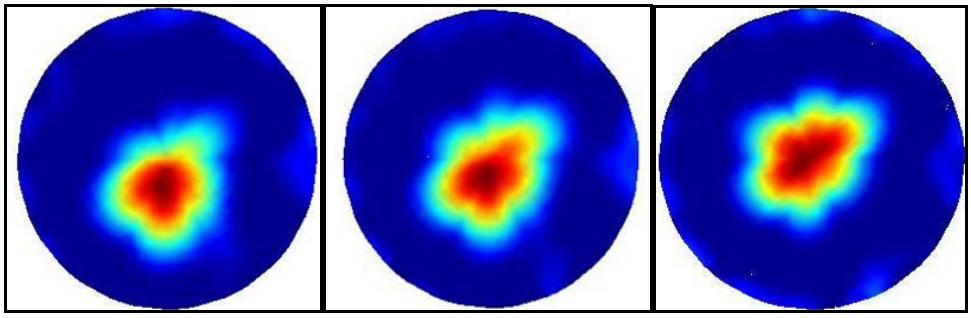

(a) (b) (c)

Figure 7-7 EIT images of 20 mm movement captured at (a) the lowest position, (b) the middle position and (c) highest position.

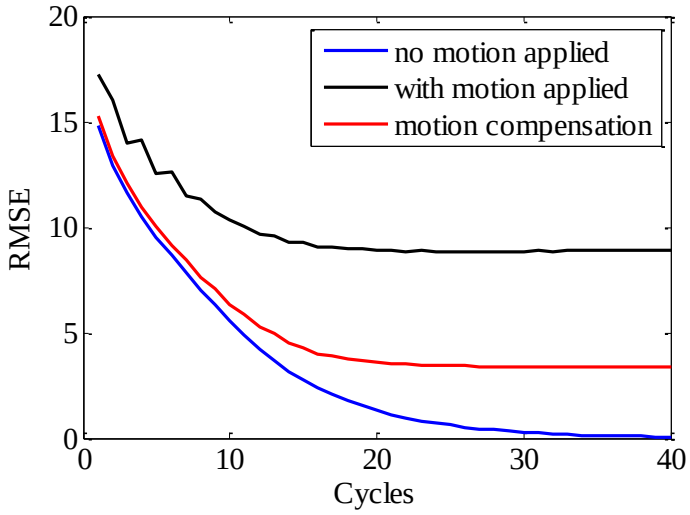

Figure 7-8 RMSE plots of motion-compensated ART when EIT motion model is used: experimental EIT study for 20 mm motion.

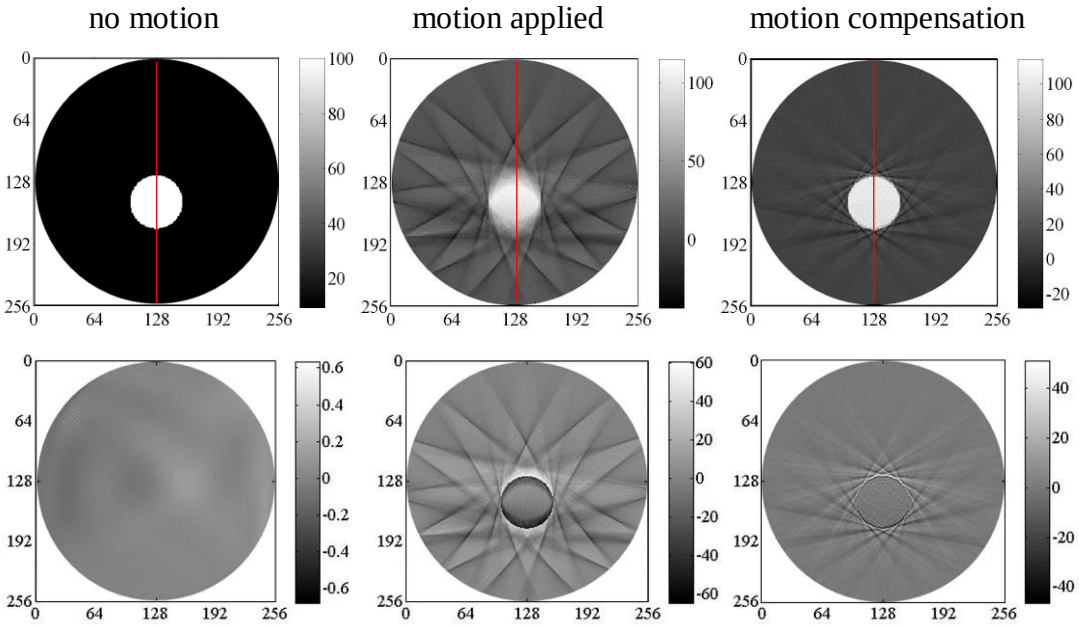

Figure 7-9 Full dataset, ART reconstructions when no motion appiled, 20 mm of motion applied in the up/down direction but no motion compensation, and approximated motion compensation using EIT motion model applied: top row is reconstructed images, bottom row is error images (the red lines are 1D plot in figure 7-10).

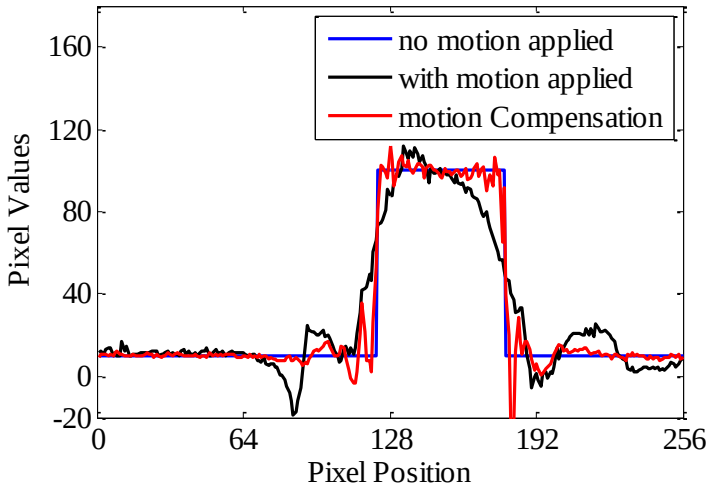

Figure 7-10 Image row plots of motion-compensated images (figure 7-9: top row) at the centre of the object (x=128).

Next, the experiment was repeated with 60 mm displacement. The results are given in figures 7-11, 7-12, and 7-13. These results show that the blurring artefacts, due to small amounts of motion, can be removed by implementing motion compensation

using the EIT motion model. However this becomes more difficult with larger motions.

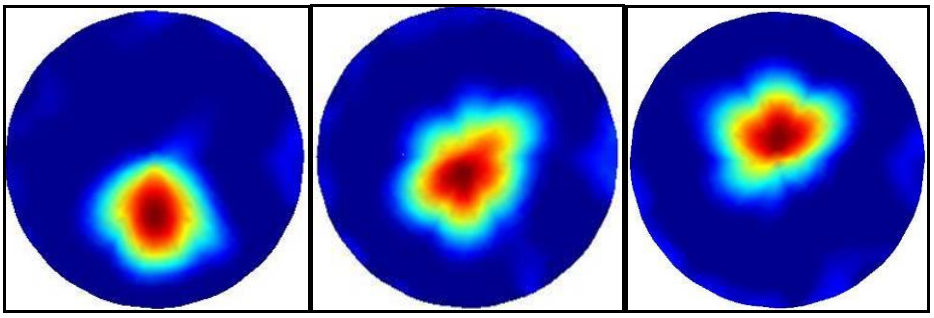

(a) (b) (c)

Figure 7-11 EIT images of 60 mm movement captured at (a) the lowest position, (b) the middle position and (c) highest position.

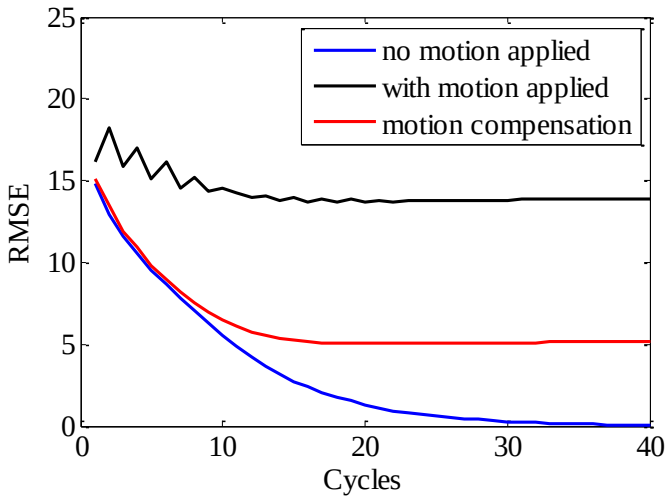

Figure 7-12 RMSE plots of motion-compensated ART when EIT motion model is used: experimental EIT study for 60 mm motion.

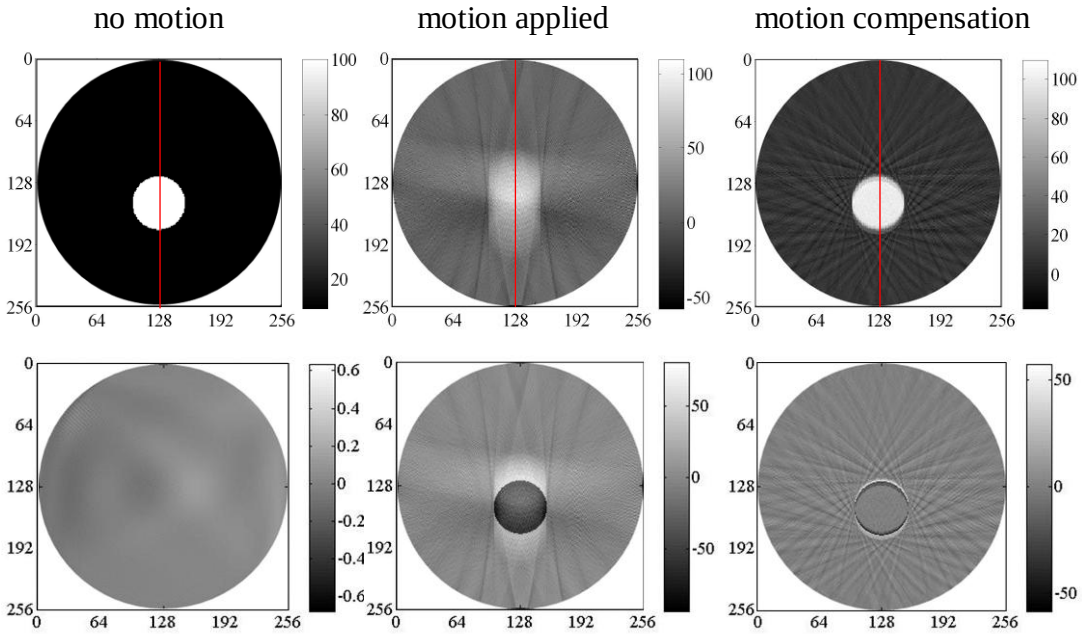

Figure 7-13 Full dataset, ART reconstructions when no motion appiled, 60 mm of motion applied in the up/down direction but no motion compensation, and approximated motion compensation using EIT motion model applied: top row is reconstructed images, bottom row is error images (the red lines are 1D plot in figure 7-14).

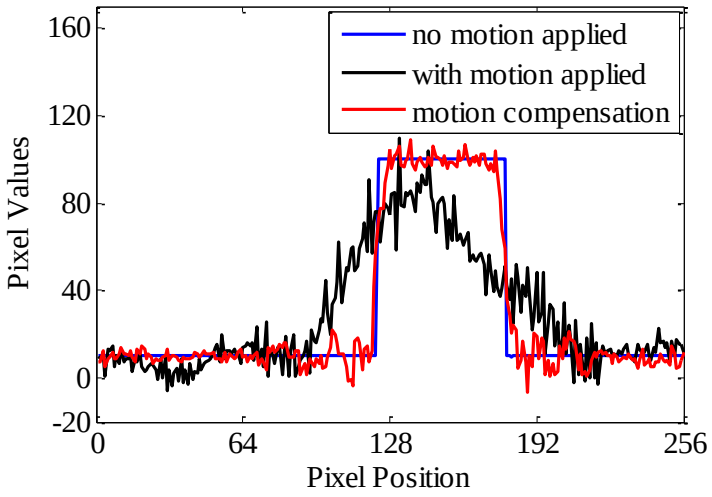

Figure 7-14 Image row plots of reconstructed images (figure 7-13: top row) at the centre of the object (x=128).

The results of 20 mm and 60 mm movements indicate that the motion-compensated ART using motion model extracted from EIT images can improve the blurring artefacts, but the efficiency of the compensation depends on the accuracy of the motion estimation.

7.2 Motion-compensated CGLS with limited data reconstructions using motion model extracted from EIT images

Next, the study of the motion-compensated CGLS with the experimental EIT motion model is demonstrated. The simulated phantom with 25 mm radius and EIT system used in section 7.1.3 was also used in this study. The experiments were experimental/simulation studies. The motion-compensated CGLS with 12 iterations and one-fourth data reconstruction, using motion model extracted from the EIT images, was investigated in the following experiments. This study was divided into 3 experiments: motion-compensated CGLS for the 20 mm up/down motion, motion-compensated CGLS for the 60 mm up/down motion and motion-compensated CGLS for the 40 mm left/right motion.

The results of motion-compensated CGLS using EIT motion model for the up/down movement are shown in section 7.2.1 for 20 mm displacement and section 7.2.2 for 60 mm displacement. Section 7.2.3 shows the results of motion-compensated CGLS using EIT motion model for the left/right direction with 40 mm displacement.

7.2.1 Motion-compensated CGLS for 20 mm motion model in the up/down direction

For the 20 mm up/down displacement, the RMSE plots are shown in figure 7-15, the reconstructed images after the 12^{th} iteration are shown in figure 7-16, and the image row plots at the object's centre (x=128) are shown in figure 7-17. It can be seen that motion image (figure 7-16) is corrupted by motion. The motion compensation using EIT motion model has lower image error than motion applied. However, after compensating, the motion artefacts cannot be completely removed which can be seen

in error image of the motion compensation comparing to the error image of the no motion. Furthermore, figure 7-16 also shows the approximated motion-compensated image using motion model extracted from the EIT images. The image row plots also support the results of reconstructed images and the RMSE plots.

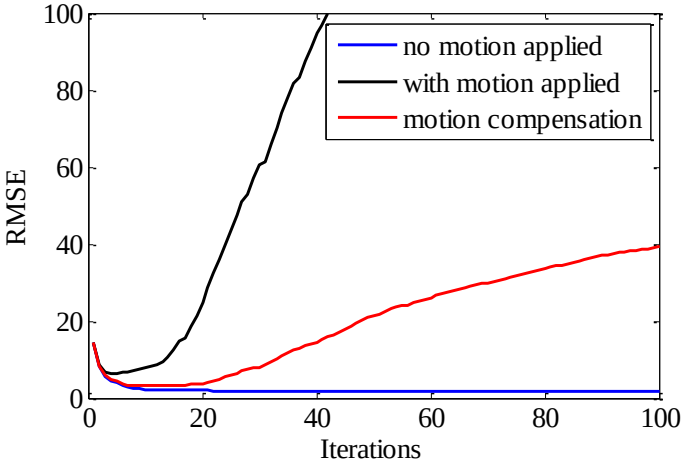

Figure 7-15 RMSE plots of motion-compensated CGLS when EIT motion model is used: experimental EIT study for 20 mm up/down motion.

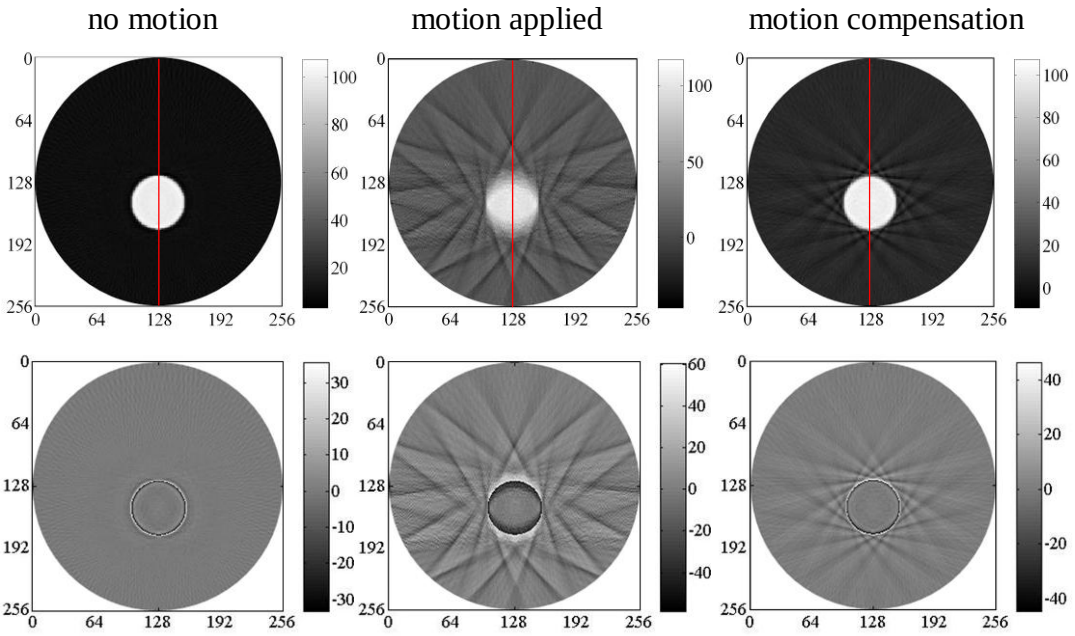

Figure 7-16 Limited dataset, CGLS reconstructions when no motion appiled, 20 mm of motion applied in the up/down direction but no motion compensation, and approximated motion compensation using EIT motion model applied: top row is reconstructed images, bottom row is error images (the red lines are 1D plot in figure 7-17).

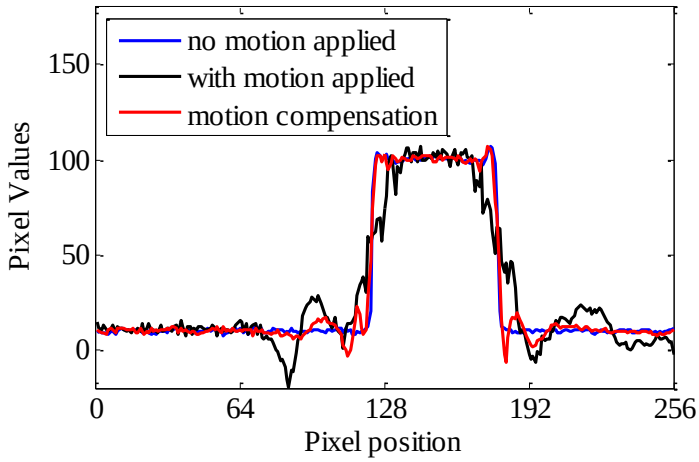

Figure 7-17 Image row plots of reconstructed images (figure 7-16: top row) at the centre of the object (x=128).

7.2.2 Motion-compensated CGLS for 60 mm motion model in the up/down direction

The results of the 60 mm up/down displacement motion compensation are shown in figures 7-18, 7-19, and 7-20. The reconstructed images and error images when no motion applied, when motion applied but no motion compensation, and when motion applied and the motion compensation using the EIT motion model used are given in figure 7-19. Figures 7-18 and 7-20 show the RMSE plots and the image row plots of reconstructed images. It can be seen that the motion-compensated image, using the EIT motion model of 60 mm, shows higher image noise than the motion-compensated image using EIT motion model of 20 mm.

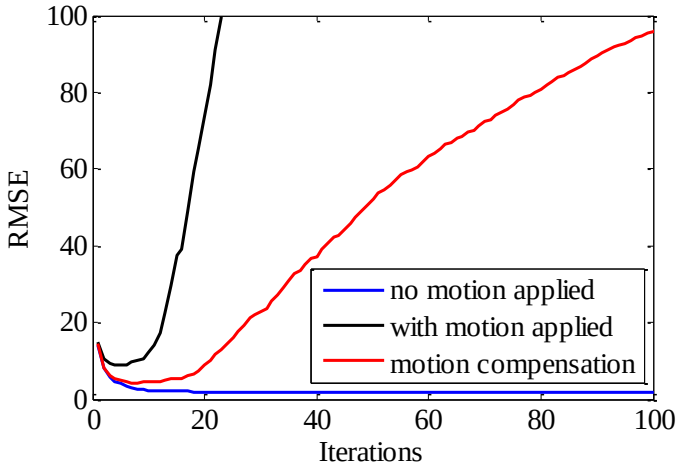

Figure 7-18 RMSE plots of motion-compensated CGLS when EIT motion model is used: experimental EIT study for 60 mm up/down motion.

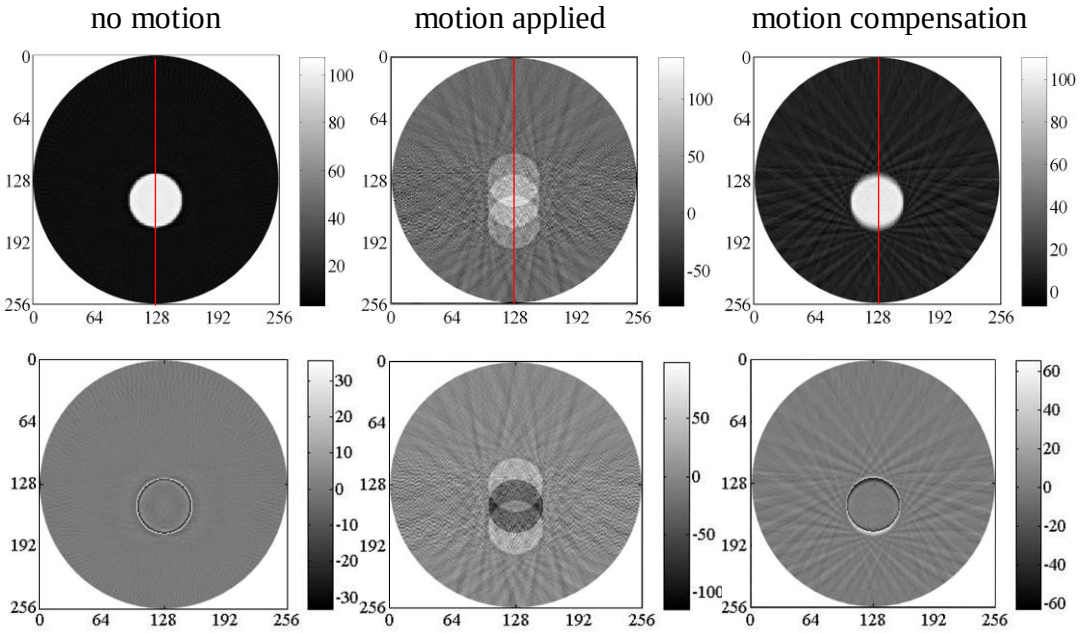

Figure 7-19 Limited dataset, CGLS reconstructions when no motion appiled, 60 mm of motion applied in the up/down direction but no motion compensation, and approximated motion compensation using EIT motion model applied: top row is reconstructed images, bottom row is error images (the red lines are 1D plot in figure 7-20).

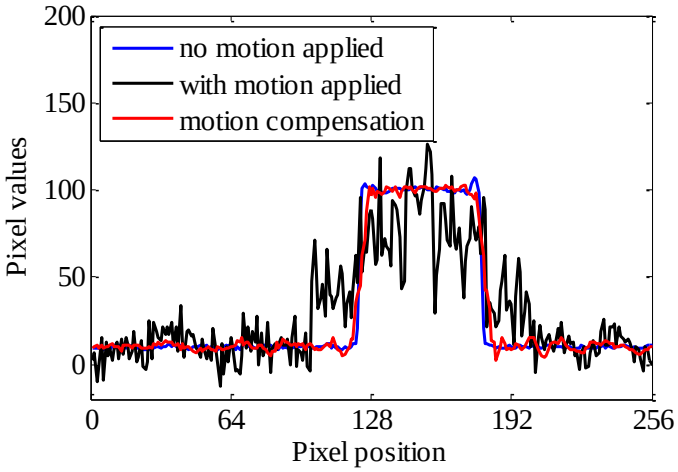

Figure 7-20 Image row plots of reconstructed images (figure 7-19: top row) at the centre of the object (x=128).

7.2.3 Motion-compensated CGLS for 40 mm motion model in the left/right direction

Figures 7-21, 7-22, and 7-23 show the results of CGLS reconstructions with the 40 mm peak-to-peak amplitude of the left/right movement. Figure 7-22(top, left) is a reconstructed image with no motion is applied. The motion blur effects are noticeable in the CBCT reconstructed image in figure 7-22(top, middle). Figure 7-22(top, right) is the motion-compensated CGLS images after the 12^{th} iteration using the motion model extracted from the EIT images. The RMSE plots (figures 7-21) show high image error when large motion model is applied. In addition, the motion compensation, using the EIT motion model, can reduce the motion blur artefacts on the CGLS image reconstruction. Image row plots running through the centre of the object in figures 7-22 (top) are shown in figure 7-23. The boundaries of the object, in motion compensated images, are sharper than those of motion applied image.

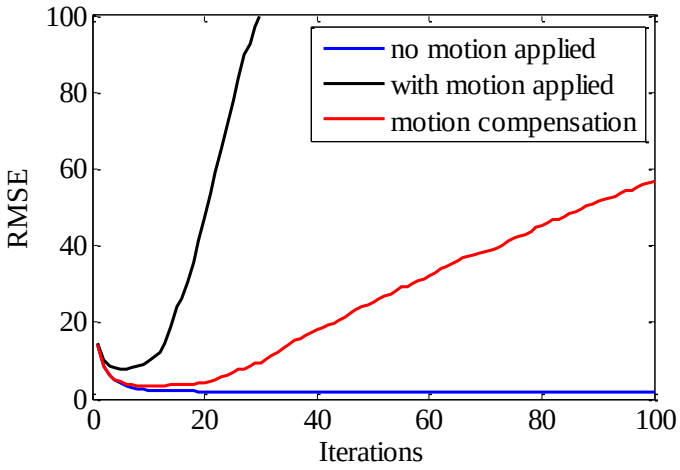

Figure 7-21 RMSE plots of motion-compensated CGLS when EIT motion model is used: experimental EIT study for 40 mm left/right motion.

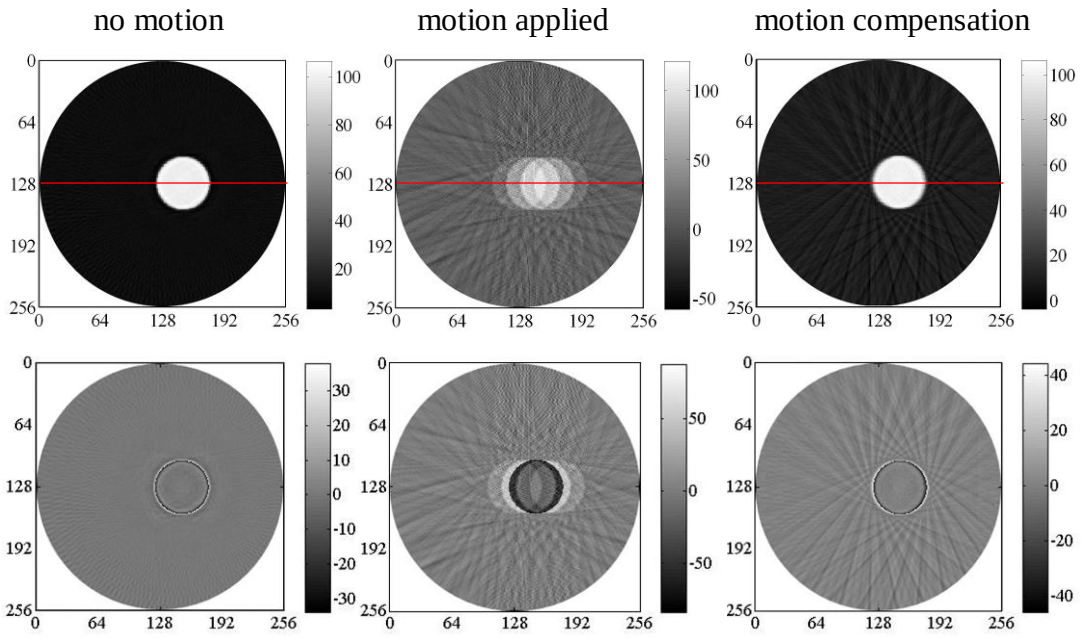

Figure 7-22 Limited dataset, CGLS reconstructions when no motion appiled, 40 mm of motion applied in the left/right direction but no motion compensation, and approximated motion compensation using EIT motion model applied: top row is reconstructed images, bottom row is error images (the red lines are 1D plot in figure 7-23).

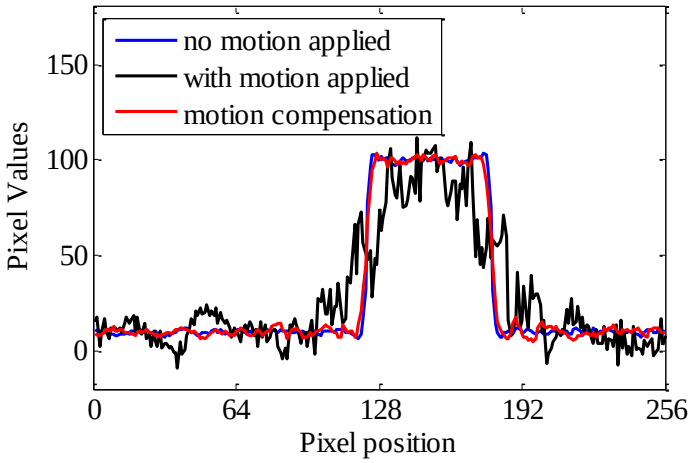

Figure 7-23 Image row plots of reconstructed images (figure 7-22: top row) at the centre of the object (y=128).

7.3 Discussions

The combination of the motion-compensated CBCT and the EIT system was the aim of this study. An advantage of high temporal resolution for the EIT imaging was the capable of capturing the fast moving objects. These EIT images were analysed for motion information extraction. The results of motion compensation using motion information extracted from EIT images integrated with an iterative algorithm of ART and CBCT were demonstrated in this chapter. The fact that the EIT provides an internal image of an object makes this modality attractive, in comparison to the other alternative techniques based on estimating motions from respiratory models. The information about the motion of internal structures was extracted from the low spatial resolution EIT images and used in the CBCT image reconstruction through an iterative algorithm applied to CBCT. The motion-compensated ART with full data reconstruction was firstly investigated for the dual modality of CBCT-EIT. Then, to reduce the computational time of ART and to reduce the patient's radiation dose, the CGLS was interesting for the motion compensation with limited data reconstruction (one-fourth data in this study) using the EIT motion model.

Both results from ART and CGLS experiments suggested that the motion model extracted from the EIT images could be used to compensate for the motion artefact in

the CBCT image reconstruction by using the developed motion compensation. However, the partial motion artefacts can be seen on the motion-compensated images. It can be seen in the experiments for the motion-compensated CGLS, that comparing among the motion-compensated images using the EIT motion model for various amounts of the motion, the motion artefacts for the 20 mm displacement experiment were lower than those for the 40 mm and 60 mm displacements. This implied that the efficiency of removing motion artefacts may depend on the accuracy of motion detection technique i.e. larger amount of the motion resulted in higher blurring effect on the motion-compensated images. Nevertheless, the motion artefacts were mostly recovered when the correct motion compensation was used for both ART and CGLS. This suggested that the motion compensation technique has the potential to compensate for the motion artefacts but the performance of the motion compensation may depend on the accuracy of motion estimation.

7.4 Conclusions

The dual modality of the CBCT-EIT was studied here by using the motion-compensated ART with full data reconstruction and the motion-compensated CGLS with one-fourth data reconstruction. The results illustrated that the motion extracted from the EIT images can be applied into the motion-compensated CBCT technique. Additionally, the motion compensation using the EIT motion model an improvement in motion artefacts for the CBCT reconstruction. However, when less accurate motion, is used to compensate in the CBCT reconstruction, the trend of motion blurring artefacts increased.

Chapter 8
Conclusions and Future Works

Radiotherapy is a primary tool for the treatment of cancers. The CBCT is commonly used to verify the treatment areas, before performing the treatment sessions. The quality of therapeutic images acquired by the CBCT is typically degraded by respiratory movement, especially for images of the thoracic and abdominal parts. Removing of the respiration-induced artefact is a challenging issue of the CBCT imaging, to achieve high accuracy of radiation treatment. Moreover, in medical imaging, there is a lot of interest in limited data reconstruction since this allows a reduction in the radiation dose to patients. The iterative reconstruction algorithm is suitable for motion compensation and limited data imaging.

The main aim of this study is to develop a dual modality of the motion-compensated CBCT reconstruction using a motion model extracted from the EIT images. This study gained the advantage of high temporal resolution of the EIT imaging system for capturing images of a moving object, and then extracting the motion model from those EIT images. This motion model was applied into the motion compensation technique, which was developed in this study. To achieve the aim, firstly, the motion compensation technique was developed and evaluated. Then, applying the motion model extracted from the EIT images to the motion compensation technique were investigated for the dual modality purpose.

In this study, the motion compensation technique through iterative algorithms was developed by using a shifting technique of the weight matrix for the relevant

projection. The evaluation of this motion compensation technique was performed using both the correct motion model and the approximated motion model. The motion compensation with full data set reconstruction using the ART algorithm and the motion compensation with one-fourth data set reconstruction using ART, SART, OS-SART and CGLS were investigated. The results showed the capability of the developed motion compensation to reduce blurring artefacts caused by motion. The motion-compensated images showed an improvement of the blurring artefacts, when compared with the uncompensated images for both full data and limited data experiments. It can be obviously seen in the image row plots that the object's boundaries of the motion-compensated images are sharper than those of the uncompensated images. In addition, the study of the approximated motion compensation (inaccurate motion model) using ART and SART for the limited data reconstruction suggested that the motion-compensated ART produces higher noise to such motion errors than the motion-compensated SART, while the blurring edges can be noticeable in SART. In general, the motion-compensated reconstruction algorithms are more sensitive to phase error than to amplitude error or random Gaussian error. The results suggested that, for the motion compensation in medical applications, the accuracy of phase respiratory detection may be more important than the accuracy of amplitude respiratory detection. Studies using patient data and real respiratory models should be investigated in future.

The motion-compensated CBCT using the EIT motion model for full data reconstruction of ART and limited data reconstruction of CGLS were also demonstrated. The experiments showed the motion extracted from the EIT images can be used in the motion compensation developed in this study. The resulting images confirmed that the motion-compensated CBCT using the EIT motion model has a capability to reduce the motion-induced artefacts for the CBCT reconstructions using the iterative algorithms.

However, there are numbers of limitations of this study. One of them is that the results showed in this study were achieved from the studies of simple simulated phantoms with the synthetic motion data and the experimental EIT data. For the

purpose of the clinical uses, studies using clinical patients' data with real respiratory movement in patients still need to be further researches. It is worth noticing the challenges involved in clinical investigation compared to our experimental outcomes. Then, the motion extraction software developed in this study used thresholding technique to locate the centre of objects for a sequence images. The results illustrated that this simple motion extraction programme produced a small error, which may be a result from tracking the object's centre, instead of tracking whole object's position. Moreover, the respiration-induced motion not only involves with the displacements of organs but also relates to the expansion of organs that cannot be detected by this motion extraction programme effectively. Therefore, more sophisticate motion extraction technique would be useful for achieving high accuracy of the motion model.

For the image reconstruction assessment, the RMSE plot can show the trend of the reconstruction error when the cycle index or iteration number was increased. However, the RMSE is not the best method to show the quality of the reconstructed images. Because it sums errors over the whole picture, does not provide the information about image distortions which are most visible in CBCT. Thus, the RMSE should be evaluated with other image assessment methods which, in this study, reconstructed images, error images and image row plot were used. Next, this is the study of evaluation of the motion compensation technique which applied into the different iterative reconstruction algorithms. In this thesis the simulated phantom models are used as a reference for comparisons.

In CGLS experiment, Tikhonov regularisation with various regularisation parameters was tested for an inconsistent case with limited data reconstruction. This showed the benefit of the regularisation for improving the divergence of the reconstruction. However, the error of reconstruction was higher than the consistent image. More advanced types of regularization, such as total variation regularization, will be an interesting extension to this work.

The computational time is one of the most important issues for the volumetric CBCT imaging reconstruction i.e. one-fourth data reconstruction of CGLS is about 2 hours. Reducing the imaging reconstruction time is challenging. There are some techniques might be useful for this issue such as a parallel computation technique or a graphics processing unit (GPU) computing. There are opportunities in further study using high performance computing devices of the proposed iterative methods.

These were preliminary results in the CBCT-EIT combination using simulation and experimental data. Further validation using the *in vivo* lung EIT images is needed. There were promising results for the *in vivo* imaging of human lungs using EIT techniques (BORSIC et al., 2010), which should strengthen the feasibility of the method proposed in this study. It is important to note that the EIT only provides information about the movement of the larger organs (e.g. lungs) and does not capture more detailed structures. Theoretical and experimental results in this study showed the potential of the proposed dual modality imaging for improving image motion blur.

Publications

Journal papers:

1) Pengpan, T., Smith, N. D., Qiu, W., Yao, A., Mitchell, C. N. and Soleimani, M., 2011. A motion-compensated cone-beam CT using electrical impedance tomography imaging. *Physiological Measurement*, 32 (1), pp. 19-34.

2) Pengpan, T., Mitchell , C.N. and Soleimani, M., 2010. A dual modality of cone beam CT and electrical impedance tomography for lung imaging. *Journal of Physics: Conference Series*, 224 (1), 012026.

3) Pengpan T, Qiu W, Smith ND, Soleimani M, 2012, Cone-beam CT using motion-compensated algebraic reconstruction methods with limited data. *Computer Methods and Programs in Biomedicine*, 105(3), pp.246-56.

4) Pengpan T, Soleimani M, Electrical Impedance Tomography Guided Motion-Compensated Cone Beam CT Using A Conjugate Gradient Least Squares Algorithm, Submitted for Computer Methods and Programs in Biomedicine.

5) Qiu W, Pengpan T, Smith ND and Soleimani M, Evaluating iterative algebraic algorithms in terms of convergence and image quality for cone beam CT, Submitted to Computer Methods and Programs in Biomedicine.

Conference papers:

6) Pengpan, T., Mitchell, C. N. and Soleimani, M., 2010. Compensating for motion artefacts in x-ray CT using electrical impedance tomography data. *In*: *6th World Congress on Industrial Process Tomography (WCIPT6)*, 6-9 September 2010, Beijing, China.

7) Pengpan , T. and Soleimani, M., 2010. Data fusion of combined high spatial resolution x-ray CT and high temporal resolution electrical impedance tomography imaging. *In*: *SIAM Conference on Imaging Science (SIAG-IS) (IS10)*, 12-14 April 2011, Chicago, USA.

8) Terzija, N., Pengpan, T., Peyton, A., Yin, W. and Soleimani, M., 2010. Extraction of motion information from electromagnetic induction tomography for flow imaging. *In*: *6th World Congress on Industrial Process Tomography (WCIPT6)*, 6-9 September 2010, Beijing, China.

Bibliography

AIRD, E. G. A. & CONWAY, J.,2002. CT simulation for radiotherapy treatment planning. *British Journal of Radiology,* 75**,** pp. 937-949.

ANDERSEN, A. H. & KAK, A. C.,1984. Simultaneous algebraic reconstruction technique (SART): a superior implementation of the ART algorithm. *Ultrasonic imaging,* 6**,** pp. 81-94.

ANTONUK, L. E.,2002. Electronic portal imaging devices: a review and historical perspective of contemporary technologies and research. *Physics in Medicine and Biology,* 47**,** pp. R31.

ANTONUK, L. E., EL-MOHRI, Y., HUANG, W., JEE, K. W., SIEWERDSEN, J. H., MAOLINBAY, M., SCARPINE, V. E., SANDLER, H. & YORKSTON, J.,1998. Initial performance evaluation of an indirect-detection, active matrix flat-panel imager (AMFPI) prototype for megavoltage imaging. *International journal of radiation oncology, biology, physics,* 42**,** pp. 437-454.

AOKI, Y., AKANUMA, A., KARASAWA, K., SAKATA, K., NAKAGAWA, K., MUTA, N., ONOGI, Y. & IIO, M.,1987. An integrated radiotherapy treatment system and its clinical application. *Radiation medicine,* 5**,** pp. 131-141.

BIKKER, I., LEONHARDT, S., REIS MIRANDA, D., BAKKER, J. & GOMMERS, D.,2010. Bedside measurement of changes in lung impedance to monitor alveolar ventilation in dependent and non-dependent parts by electrical impedance tomography during a positive end-expiratory pressure trial in mechanically ventilated intensive care unit patients. *Critical Care,* 14**,** pp. R100.

BODENSTEIN, M., DAVID, M. & MARKSTALLER, K.,2009. Principles of electrical impedance tomography and its clinical application. *Critical Care Medicine,* 37**,** pp. 713-724

BORSIC, A., GRAHAM, B. M., ADLER, A. & LIONHEART, W.,2010. In Vivo Impedance Imaging With Total Variation Regularization. *IEEE Transactions on Medical Imaging,* 29**,** pp. 44-54.

BUZUG, T. M.,2008. *Computed tomography : from photon statistics to modern cone-beam CT.* Heidelberg: Springer.

CHEN, G., SHARP, G. & MORI, S.,2009. A review of image-guided radiotherapy. *Radiological Physics and Technology,* 2**,** pp. 1-12.

CHLEWICKI, W., BADEA, C. & PALLIKARAKIS, N.,2001. Cone based 3D reconstruction: A FDK-SART comparison for limited number of projections. *MEDICON,* June**,** pp. 12-15.

DAWSON, L. A. & JAFFRAY, D. A.,2007. Advances in Image-Guided Radiation Therapy. *Journal of Clinical Oncology,* 25**,** pp. 938-946.

EDIC, P. M., SAULNIER, G. J., NEWELL, J. C. & ISAACSON, D.,1995. A real-time electrical impedance tomograph. *IEEE Transactions on Biomedical Engineering,* 42**,** pp. 849-859.

EKBERG, L., HOLMBERG, O., WITTGREN, L., BJELKENGREN, G. R. & LANDBERG, T.,1998. What margins should be added to the clinical target volume in radiotherapy treatment planning for lung cancer? *Radiotherapy and Oncology,* 48**,** pp. 71-77.

FARR, R. F. & ALLISY-ROBERTS, P. J.,1998. *Physics for medical imaging.* Edinburgh: W. B. Saunders.

FELDKAMP, L. A., DAVIS, L. C. & KRESS, J. W.,1984. Practical cone-beam algorithm. *Journal of the Optical Society of America A,* Vol. 1, **,** pp. 612-619.

GE, W. & MING, J.,2004. Ordered-subset simultaneous algebraic reconstruction techniques (OS-SART). *Journal of X-ray Science and Technology,* 12**,** pp. 169-177.

GORDON, R., BENDER, R. & HERMAN, G. T.,1970. Algebraic Reconstruction Techniques (ART) for three-dimensional electron microscopy and X-ray photography. *Journal of Theoretical Biology* 29**,** pp. 471-481.

HANSIS, E. & LINGXIONG, S.,2011. *Simulation of motion artifacts in offset flat-panel cone-beam CT.Nuclear Science Symposium and Medical Imaging Conference (NSS/MIC),* 23-29 Oct. 2011.2471-2475

HOLDER, D.,1993. *Clinical and Physiological Applications of Electrical Impedance Tomography.* Taylor and Francis.

HUDSON, H. M. & LARKIN, R. S.,1994. Accelerated image reconstruction using ordered subsets of projection data. *IEEE Transactions on Medical Imaging,* 13**,** pp. 601-609.

ISHERWOOD, I.,2005. Sir Godfrey Hounsfield. *Radiology,* 234**,** pp. 975-976.

JAFFRAY, D. A. & SIEWERDSEN, J. H.,2000. Cone-beam computed tomography with a flat-panel imager: Initial performance characterization. *Medical physics,* 27**,** pp. 1311-1323.

JAFFRAY, D. A., SIEWERDSEN, J. H., WONG, J. W. & MARTINEZ, A. A.,2002. Flat-panel cone-beam computed tomography for image-guided radiation therapy. *International Journal of Radiation Oncology Biology Physics,* 53**,** pp. 1337-1349.

JIA, X., DONG, B., LOU, Y. & JIANG, S. B.,2011. GPU-based iterative cone-beam CT reconstruction using tight frame regularization. *Physics in Medicine and Biolology* 56**,** pp. 3787-3807.

JIANG, M. & WANG, G.,2003. Convergence studies on iterative algorithms for image reconstruction. *IEEE Transactions on Medical Imaging,* 22**,** pp. 569-579.

JIANG, S. B., POPE, C., JARRAH, K. M. A., KUNG, J. H., BORTFELD, T. & CHEN, G. T. Y.,2003. An experimental investigation on intra-fractional organ motion effects in lung IMRT treatments. *Physics in Medicine and Biology,* 48**,** pp. 1773-1784.

JUHLER, N. T., KORREMAN, S. S., PEDERSEN, A. N., AARUP, L. R., NYSTROM, H., OLSEN, M. & SPECHT, L.,2007. Intra- and interfraction breathing variations during curative radiotherapy for lung cancer. *Radiotherapy and Oncology,* 84**,** pp. 40-48.

KAK, A. C. & SLANEY, M.,1999. Principles of computerized tomographic imaging Philadephia, Society for Industrial and Applied Mathematics

KAO, T.-J., SAULNIER, G. J., XIA, H., TAMMA, C., NEWELL, J. C. & ISAACSON, D.,2007. A compensated radiolucent electrode array for combined EIT and mammography. *Physiological Measurement,* 28**,** pp. S291-S299.

KINAHAN, P. E., MATEJ, S., KARP, J. S., HERMAN, G. T. & LEWITT, R. M.,1994. *A comparison of transform and iterative reconstruction techniques for a volume-imaging PET scanner with a large axial acceptance angle.Nuclear Science Symposium and Medical Imaging Conference, 1994., 1994 IEEE Conference Record,* 30 October 1994 - 05 November 1994 Virginia , USA:IEEE,pp. 1320-1324

LOW, D. A., NYSTROM, M., KALININ, E., PARIKH, P., DEMPSEY, J. F., BRADLEY, J. D., MUTIC, S., WAHAB, S. H., ISLAM, T., CHRISTENSEN, G., POLITTE, D. G. & WHITING, B. R.,2003. A method for the reconstruction of four-dimensional synchronized CT scans acquired during free breathing. *Medical Physics,* 30**,** pp. 1254-1263.

MAGERAS, G. S., PEVSNER, A., YORKE, E. D., ROSENZWEIG, K. E., FORD, E. C., HERTANTO, A., LARSON, S. M., LOVELOCK, D. M., ERDI, Y. E., NEHMEH, S. A., HUMM, J. L. & LING, C. C.,2004. Measurement of lung tumor motion using respiration-correlated CT. *International Journal of Radiation Oncology Biology Physics,* 60**,** pp. 933-941.

MARCHANT, T. E., AMER, A. M. & MOORE, C. J.,2008. Measurement of inter and intra fraction organ motion in radiotherapy using cone beam CT projection images. *Physics in Medicine and Biology,* 53**,** pp. 1087.

MUELLER, K., YAGEL, R. & WHELLER, J. J.,1999. Fast implementations of algebraic methods for three-dimensional reconstruction from cone-beam data. *Medical Imaging, IEEE Transactions on,* 18**,** pp. 538-548.

NATTERER, F.,2001. *The mathematics of computerized tomography.* Philadephia: Society for Industrial and Applied Mathematics.

PENGPAN, T., SMITH, N. D., QIU, W., YAO, A., MITCHELL, C. N. & SOLEIMANI, M.,2011. A motion-compensated cone-beam CT using electrical impedance tomography imaging. *Physiological Measurement* 32**,** pp. 19-34.

POLYDORIDES, N. & LIONHEART, W. R. B.,2002. A Matlab toolkit for three-dimensional electrical impedance tomography: a contribution to the Electrical Impedance and Diffuse Optical Reconstruction Software project. *Measurement Science and Technology,* 13**,** pp. 1871-1883.

PURDIE, T. G., MOSELEY, D. J., BISSONNETTE, J.-P., SHARPE, M. B., FRANKS, K., BEZJAK, A. & JAFFRAY, D. A.,2006. Respiration correlated cone-beam computed tomography and 4DCT for evaluating target motion in Stereotactic Lung Radiation Therapy. *Acta Oncologica,* 45**,** pp. 915-922.

QIU, W., TONG, J., MITCHELL, C., MARCHANT, T., SPENCER, P., C.J.MOORE & SOLEIMANI, M.,2010. New iterative cone beam CT reconstruction software: parameter optimisation and convergence study. *Computer Methods and Programs in Biomedicine* 100**,** pp. 166-174.

RIT, S., SARRUT, D. & DESBAT, L.,2009a. Comparison of analytic and algebraic methods for motion-compensated cone-beam CT reconstruction of the thorax. *IEEE Transactions on Medical Imaging,* 28**,** pp. 1513-1525.

RIT, S., SARRUT, D. & GINESTET, C.,2005. *Respiratory signal extraction for 4D CT imaging of the thorax from cone-beam CT projections.8th International Conference on Medical Image Computing and Computer-Assisted Intervention (MICCAI),* 26-30 October 2005.California, USA 556-563

RIT, S., WOLTHAUS, J. W. H., VAN HERK, M. & SONKE, J.-J.,2009b. On-the-fly motion-compensated cone-beam CT using an a priori model of the respiratory motion. *Medical Physics,* 36**,** pp. 2283-2296.

ROS, D., FALCóN, C., JUVELLS, I. & PAVíA, J.,1996. The influence of a relaxation parameter on SPECT iterative reconstruction algorithms. *Physics in Medicine and Biology,* 41**,** pp. 925-937.

RUCHALA, K. J., OLIVERA, G. H., SCHLOESSER, E. A. & MACKIE, T. R.,1999. Megavoltage CT on a tomotherapy system. *Physics in Medicine and Biology,* 44**,** pp. 2597.

SEERAM, E.,2000. *Computed tomography: Physical principles, Clinical applications, and Quality control* 2. Elsevier Health Sciences.

SEGARS, W. P.,2001. Development and application of the new dynamic NURBS-based Cardiac-Torso (NCAT) phantom. *Biomedical Engineering.* University of North Carolina.

SEPPENWOOLDE, Y., SHIRATO, H., KITAMURA, K., SHIMIZU, S., VAN HERK, M., LEBESQUE, J. V. & MIYASAKA, K.,2002. Precise and real-time measurement of 3D tumor motion in lung due to breathing and heartbeat, measured during radiotherapy. *International Journal of Radiation Oncology Biology Physics,* 53**,** pp. 822-834.

SONKE, J.-J., LEBESQUE, J. & VAN HERK, M.,2008. Variability of four-dimensional computed tomography patient models. *International Journal of Radiation Oncology Biology Physics,* 70**,** pp. 590-598.

SONKE, J.-J., ZIJP, L., REMEIJER, P. & VAN HERK, M.,2005. Respiratory correlated cone beam CT. *Medical physics,* 32**,** pp. 1176-1186.

TERZIJA, N., PENGPAN, T., PEYTON, A. J., YIN, W. & SOLEIMANI, M.,2010. Extraction of motion information from electromagnetic induction tomography for flow imaging. *6th World Congress on Industrial Process Tomography.* Beijing, China, Sage Publications, Inc.

TUY, H.,1983. An Inversion Formula for Cone-Beam Reconstruction. *SIAM Journal on Applied Mathematics,* 43**,** pp. 546-552.

VEDAM, S. S., KEALL, P. J., KINI, V. R., MOSTAFAVI, H., SHUKLA, H. P. & MOHAN, R.,2003. Acquiring a four-dimensional computed tomography dataset using an external respiratory signal. *Physics in Medicine and Biology,* 48**,** pp. 45-62.

WEBB, S., LILLICRAP, S. C., STEERE, H. & SPELLER, R. D.,1977. Application of a radiotherapy simulator for imaging of body cross sections. *The British Journal of Radiology,* 50**,** pp. 152-153.

YU, H., YE, Y., ZHAO, S. & WANG, G.,2006. Studies on Palamodov's algorithm for cone-beam CT along a general curve. *Inverse Problems,* 22**,** pp. 447.

Appendix

This is a simple example of 2-by-2 matrix image reconstruction for ART, SART and CGLS. The initial values are assumed as all zeros. The measured data (projection data) of this example (b) are $\begin{bmatrix}3 & 7 & 5 & 6 & 4\end{bmatrix}$ as shown below.

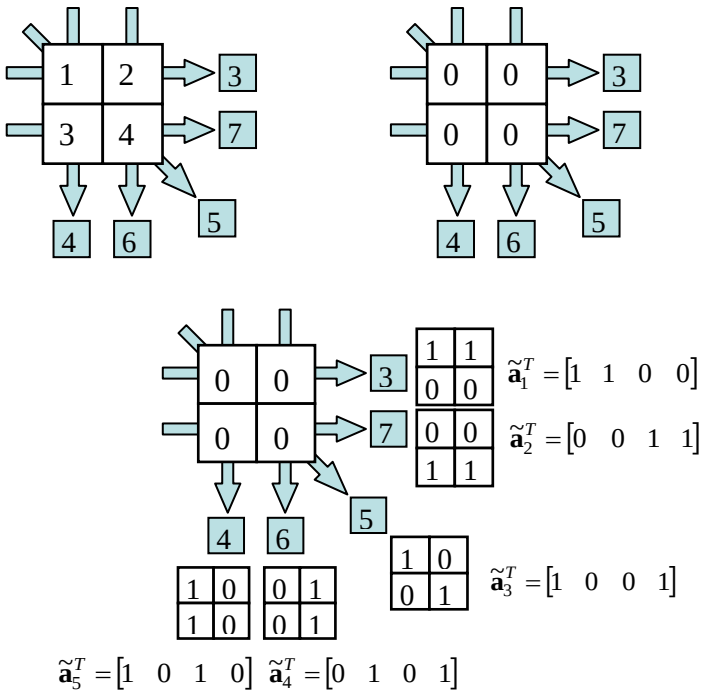

The weight matrix (**A**) is the combination of $\tilde{\mathbf{a}}_i^T$ where i is the ray index , then A is

$$\mathbf{A} = \begin{bmatrix} \tilde{\mathbf{a}}_1^T \\ \tilde{\mathbf{a}}_2^T \\ \tilde{\mathbf{a}}_3^T \\ \tilde{\mathbf{a}}_4^T \\ \tilde{\mathbf{a}}_5^T \end{bmatrix} = \begin{bmatrix} 1 & 1 & 0 & 0 \\ 0 & 0 & 1 & 1 \\ 1 & 0 & 0 & 1 \\ 0 & 1 & 0 & 1 \\ 1 & 0 & 1 & 0 \end{bmatrix}.$$

Algebraic Reconstruction Technique (ART)

To obtain $\mathbf{x}^{(k+1)}$, the weighting matrix, the measured data and the initial values are given as follows.

1st iteration: calculate for the 1st ray (highlighted in red). The weight matrix of the 1st ray ($\tilde{\mathbf{a}}_1^T = \begin{bmatrix} 1 & 1 & 0 & 0 \end{bmatrix}$) is used.

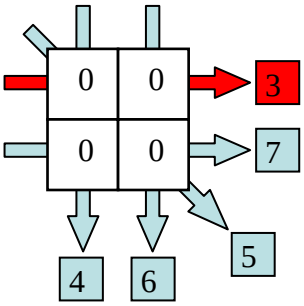

$$\mathbf{x}^{(1)} = \mathbf{x}^{(0)} + \frac{1}{\tilde{\mathbf{a}}_1^T \tilde{\mathbf{a}}_1}\left(b_1 - \tilde{\mathbf{a}}_1^T \mathbf{x}^{(0)}\right)\tilde{\mathbf{a}}_1$$

$$\mathbf{x}^{(1)} = \begin{bmatrix} 0 \\ 0 \\ 0 \\ 0 \end{bmatrix} + \frac{1}{\begin{bmatrix} 1 & 1 & 0 & 0 \end{bmatrix}\begin{bmatrix} 1 \\ 1 \\ 0 \\ 0 \end{bmatrix}}\left(3 - \begin{bmatrix} 1 & 1 & 0 & 0 \end{bmatrix}\begin{bmatrix} 0 \\ 0 \\ 0 \\ 0 \end{bmatrix}\right)\begin{bmatrix} 1 \\ 1 \\ 0 \\ 0 \end{bmatrix}$$

$$\mathbf{x}^{(1)} = \begin{bmatrix} 0 \\ 0 \\ 0 \\ 0 \end{bmatrix} + \frac{1}{2}(3-0)\begin{bmatrix} 1 \\ 1 \\ 0 \\ 0 \end{bmatrix} = \begin{bmatrix} 0 \\ 0 \\ 0 \\ 0 \end{bmatrix} + \frac{1}{2}\begin{bmatrix} 3 \\ 3 \\ 0 \\ 0 \end{bmatrix}$$

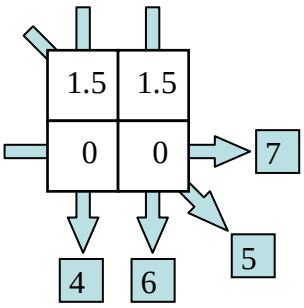

$$\mathbf{x}^{(1)} = \begin{bmatrix} 1.5 \\ 1.5 \\ 0 \\ 0 \end{bmatrix}$$

Then, the calculation is repeated for further cycles as follows.

2nd iteration: calculate for the 2nd ray (highlighted in red). The weight matrix of the 2nd ray ($\tilde{\mathbf{a}}_2^T = \begin{bmatrix} 0 & 0 & 1 & 1 \end{bmatrix}$) is used.

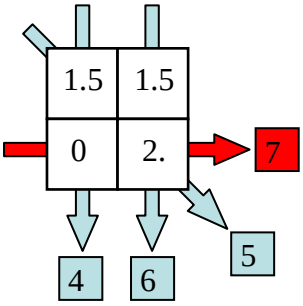

$$\mathbf{x}^{(2)} = \mathbf{x}^{(1)} + \frac{1}{\tilde{\mathbf{a}}_2^T \tilde{\mathbf{a}}_2}\left(b_2 - \tilde{\mathbf{a}}_2^T \mathbf{x}^{(1)}\right)\tilde{\mathbf{a}}_2$$

$$\mathbf{x}^{(2)} = \begin{bmatrix} 1.5 \\ 1.5 \\ 0 \\ 0 \end{bmatrix} + \frac{1}{\begin{bmatrix} 0 & 0 & 1 & 1 \end{bmatrix}\begin{bmatrix} 0 \\ 0 \\ 1 \\ 1 \end{bmatrix}}\left(7 - \begin{bmatrix} 0 & 0 & 1 & 1 \end{bmatrix}\begin{bmatrix} 1.5 \\ 1.5 \\ 0 \\ 0 \end{bmatrix}\right)\begin{bmatrix} 0 \\ 0 \\ 1 \\ 1 \end{bmatrix}$$

$$\mathbf{x}^{(2)} = \begin{bmatrix} 1.5 \\ 1.5 \\ 0 \\ 0 \end{bmatrix} + \frac{1}{2}(7-0)\begin{bmatrix} 0 \\ 0 \\ 1 \\ 1 \end{bmatrix} = \begin{bmatrix} 1.5 \\ 1.5 \\ 0 \\ 0 \end{bmatrix} + \frac{1}{2}\begin{bmatrix} 0 \\ 0 \\ 7 \\ 7 \end{bmatrix}$$

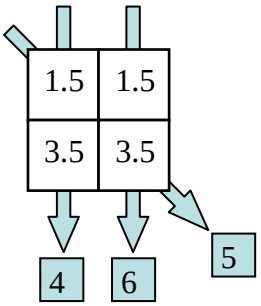

$$\mathbf{x}^{(2)} = \begin{bmatrix} 1.5 \\ 1.5 \\ 3.5 \\ 3.5 \end{bmatrix}$$

3rd iteration: calculate for the 3rd ray (highlighted in red). The weight matrix of the 3rd ray ($\tilde{\mathbf{a}}_3^T = \begin{bmatrix} 1 & 0 & 0 & 1 \end{bmatrix}$) is used.

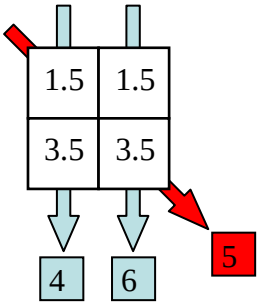

$$\mathbf{x}^{(3)} = \mathbf{x}^{(2)} + \frac{1}{\tilde{\mathbf{a}}_3^T \tilde{\mathbf{a}}_3}\left(b_3 - \tilde{\mathbf{a}}_3^T \mathbf{x}^2\right)\tilde{\mathbf{a}}_3$$

$$\mathbf{x}^{(3)} = \begin{bmatrix} 1.5 \\ 1.5 \\ 3.5 \\ 3.5 \end{bmatrix} + \frac{1}{\begin{bmatrix} 1 & 0 & 0 & 1 \end{bmatrix}\begin{bmatrix} 1 \\ 0 \\ 0 \\ 1 \end{bmatrix}}\left(5 - \begin{bmatrix} 1 & 0 & 0 & 1 \end{bmatrix}\begin{bmatrix} 1.5 \\ 1.5 \\ 3.5 \\ 3.5 \end{bmatrix}\right)\begin{bmatrix} 1 \\ 0 \\ 0 \\ 1 \end{bmatrix}$$

$$\mathbf{x}^{(3)} = \begin{bmatrix} 1.5 \\ 1.5 \\ 3.5 \\ 3.5 \end{bmatrix} + \frac{1}{2}(5-5)\begin{bmatrix} 1 \\ 0 \\ 0 \\ 1 \end{bmatrix} = \begin{bmatrix} 1.5 \\ 1.5 \\ 3.5 \\ 3.5 \end{bmatrix} + \frac{1}{2}\begin{bmatrix} 0 \\ 0 \\ 0 \\ 0 \end{bmatrix}$$

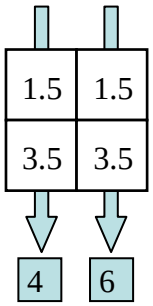

$$\mathbf{x}^{(3)} = \begin{bmatrix} 1.5 \\ 1.5 \\ 3.5 \\ 3.5 \end{bmatrix}$$

4th iteration: calculate for the 4th ray (highlighted in red). The weight matrix of the 4th ray ($\tilde{\mathbf{a}}_4^T = [0 \quad 1 \quad 0 \quad 1]$) and $b_4 = 6$ are used.

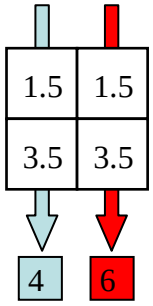

$$\mathbf{x}^{(4)} = \mathbf{x}^{(3)} + \frac{1}{\tilde{\mathbf{a}}_4^T \tilde{\mathbf{a}}_4}\left(b_4 - \tilde{\mathbf{a}}_4^T \mathbf{x}^{(3)}\right)\tilde{\mathbf{a}}_4$$

$$\mathbf{x}^{(4)} = \begin{bmatrix}1.5\\1.5\\3.5\\3.5\end{bmatrix} + \frac{1}{\begin{bmatrix}0 & 1 & 0 & 1\end{bmatrix}\begin{bmatrix}0\\1\\0\\1\end{bmatrix}}\left(6 - \begin{bmatrix}0 & 1 & 0 & 1\end{bmatrix}\begin{bmatrix}1.5\\1.5\\3.5\\3.5\end{bmatrix}\right)\begin{bmatrix}0\\1\\0\\1\end{bmatrix}$$

$$\mathbf{x}^{(4)} = \begin{bmatrix}1.5\\1.5\\3.5\\3.5\end{bmatrix} + \frac{1}{2}(6-5)\begin{bmatrix}0\\1\\0\\1\end{bmatrix} = \begin{bmatrix}1.5\\1.5\\3.5\\3.5\end{bmatrix} + \frac{1}{2}\begin{bmatrix}0\\1\\0\\1\end{bmatrix}$$

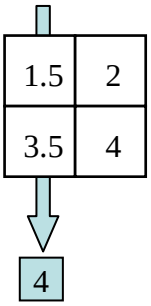

$$\mathbf{x}^{(4)} = \begin{bmatrix}1.5\\2\\3.5\\4\end{bmatrix}$$

5th iteration: calculate for the 5th ray (highlighted in red). The weight matrix of the 5th ray ($\tilde{\mathbf{a}}_5^T = [1 \quad 0 \quad 1 \quad 0]$) and b_5=4 are used.

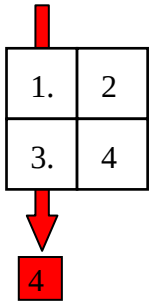

$$\mathbf{x}^{(5)} = \begin{bmatrix} 1.5 \\ 2 \\ 3.5 \\ 4 \end{bmatrix} + \frac{1}{\begin{bmatrix} 1 & 0 & 1 & 0 \end{bmatrix} \begin{bmatrix} 1 \\ 0 \\ 1 \\ 0 \end{bmatrix}} \left(4 - \begin{bmatrix} 1 & 0 & 1 & 0 \end{bmatrix} \begin{bmatrix} 1.5 \\ 2 \\ 3.5 \\ 4 \end{bmatrix} \right) \begin{bmatrix} 1 \\ 0 \\ 1 \\ 0 \end{bmatrix}$$

$$\mathbf{x}^{(5)} = \begin{bmatrix} 1.5 \\ 2 \\ 3.5 \\ 4 \end{bmatrix} + \frac{1}{2}(4-5) \begin{bmatrix} 1 \\ 0 \\ 1 \\ 0 \end{bmatrix} = \begin{bmatrix} 1.5 \\ 2 \\ 3.5 \\ 4 \end{bmatrix} + \frac{1}{2} \begin{bmatrix} -1 \\ 0 \\ -1 \\ 0 \end{bmatrix}$$

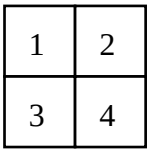

$$\mathbf{x}^{(5)} = \begin{bmatrix} 1 \\ 2 \\ 3 \\ 4 \end{bmatrix}$$

Simultaneous Algebraic Reconstruction Technique (SART)

To obtain $\mathbf{x}^{(k+1)}$, the weighting matrix, the measured data and the initial values are given. From equation 3-7, $\mathbf{x}^{(k+1)} = \mathbf{x}^{(k)} + \lambda_n \mathbf{V}^{-1}\mathbf{A}^T\mathbf{W}\left(\mathbf{b} - \mathbf{A}\mathbf{x}^{(k)}\right)$, the relaxation parameter is not considered in this example. An $V^{-1}A^TW$ is first calculated as follows.

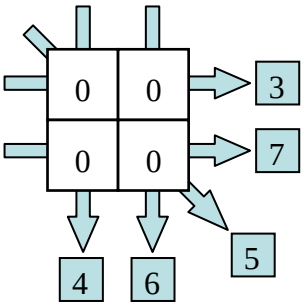

$$\mathbf{V}_{jj} = \sum_{i=1}^{M} \left|\mathbf{A}_{ij}\right| = \sum_{i=1}^{M} \left\| \begin{bmatrix} 1 & 1 & 0 & 0 \\ 0 & 0 & 1 & 1 \\ 1 & 0 & 0 & 1 \\ 0 & 1 & 0 & 1 \\ 1 & 0 & 1 & 0 \end{bmatrix} \right\| = \begin{bmatrix} 3 & 0 & 0 & 0 \\ 0 & 2 & 0 & 0 \\ 0 & 0 & 2 & 0 \\ 0 & 0 & 0 & 3 \end{bmatrix}$$

$$\mathbf{W}_{ii} = \frac{1}{\sum_{j=1}^{N} \left|\mathbf{A}_{ij}\right|} = \frac{1}{\sum_{j=1}^{N} \begin{bmatrix} 1 & 1 & 0 & 0 \\ 0 & 0 & 1 & 1 \\ 1 & 0 & 0 & 1 \\ 0 & 1 & 0 & 1 \\ 1 & 0 & 1 & 0 \end{bmatrix}} = \begin{bmatrix} \frac{1}{2} & 0 & 0 & 0 & 0 \\ 0 & \frac{1}{2} & 0 & 0 & 0 \\ 0 & 0 & \frac{1}{2} & 0 & 0 \\ 0 & 0 & 0 & \frac{1}{2} & 0 \\ 0 & 0 & 0 & 0 & \frac{1}{2} \end{bmatrix}$$

$$\mathbf{V}^{-1}\mathbf{A}^T\mathbf{W} = \begin{bmatrix} 3 & 0 & 0 & 0 \\ 0 & 2 & 0 & 0 \\ 0 & 0 & 2 & 0 \\ 0 & 0 & 0 & 3 \end{bmatrix}^{-1} \begin{bmatrix} 1 & 1 & 0 & 0 \\ 0 & 0 & 1 & 1 \\ 1 & 0 & 0 & 1 \\ 0 & 1 & 0 & 1 \\ 1 & 0 & 1 & 0 \end{bmatrix}^T \begin{bmatrix} \frac{1}{2} & 0 & 0 & 0 & 0 \\ 0 & \frac{1}{2} & 0 & 0 & 0 \\ 0 & 0 & \frac{1}{2} & 0 & 0 \\ 0 & 0 & 0 & \frac{1}{2} & 0 \\ 0 & 0 & 0 & 0 & \frac{1}{2} \end{bmatrix}$$

$$= \begin{bmatrix} 0.167 & 0 & 0.167 & 0 & 0.167 \\ 0.25 & 0 & 0 & 0.25 & 0 \\ 0 & 0.25 & 0 & 0 & 0.25 \\ 0 & 0.167 & 0.167 & 0.167 & 0 \end{bmatrix}$$

1st cycle: calculate for updating whole image. All measured data (**b**), the whole weight (**A**) matrix and initial values (x^0) are used.

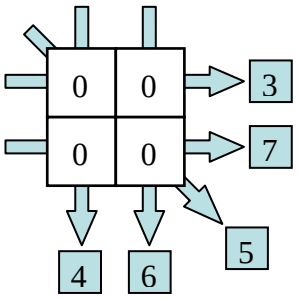

$$\mathbf{x}^{(1)} = \mathbf{x}^{(0)} + \mathbf{V}^{-1}\mathbf{A}^T\mathbf{W}\left(\mathbf{b} - \mathbf{A}\mathbf{x}^{(0)}\right)$$

$$\mathbf{x}^{(1)} = \begin{bmatrix}0\\0\\0\\0\end{bmatrix} + \begin{bmatrix}0.167 & 0 & 0.167 & 0 & 0.167\\ 0.25 & 0 & 0 & 0.25 & 0\\ 0 & 0.25 & 0 & 0 & 0.25\\ 0 & 0.167 & 0.167 & 0.167 & 0\end{bmatrix}\left(\begin{bmatrix}3\\7\\5\\6\\4\end{bmatrix} - \begin{bmatrix}1&1&0&0\\0&0&1&1\\1&0&0&1\\0&1&0&1\\1&0&1&0\end{bmatrix}\begin{bmatrix}0\\0\\0\\0\end{bmatrix}\right)$$

$$\mathbf{x}^{(1)} = \begin{bmatrix}0\\0\\0\\0\end{bmatrix} + \begin{bmatrix}2\\2.25\\2.75\\3\end{bmatrix} = \begin{bmatrix}2\\2.25\\2.75\\3\end{bmatrix}$$

2	2.25
2.75	3

2nd cycle: All measured data (**b**), the whole weight (**A**) matrix and initial values ($\mathbf{x}^{(1)}$) are used.

2	2.25
2.75	3

$$\mathbf{x}^{(2)} = \mathbf{x}^{(1)} + \mathbf{V}^{-1}\mathbf{A}^T\mathbf{W}\left(\mathbf{b} - \mathbf{A}\mathbf{x}^{(1)}\right)$$

$$\mathbf{x}^{(2)} = \begin{bmatrix}2\\2.25\\2.75\\3\end{bmatrix} + \begin{bmatrix}0.167 & 0 & 0.167 & 0 & 0.167\\ 0.25 & 0 & 0 & 0.25 & 0\\ 0 & 0.25 & 0 & 0 & 0.25\\ 0 & 0.167 & 0.167 & 0.167 & 0\end{bmatrix}\left(\begin{bmatrix}3\\7\\5\\6\\4\end{bmatrix} - \begin{bmatrix}1&1&0&0\\0&0&1&1\\1&0&0&1\\0&1&0&1\\1&0&1&0\end{bmatrix}\begin{bmatrix}2\\2.25\\2.75\\3\end{bmatrix}\right)$$

1.67	1.13
2.88	3.33

$$\mathbf{x}^{(2)} = \begin{bmatrix}1.67\\1.13\\2.88\\3.33\end{bmatrix}$$

3rd cycle: All measured data (**b**), the whole weight (**A**) matrix and initial values ($\mathbf{x}^{(2)}$) are used.

1.67	1.13
2.88	3.33

$$\mathbf{x}^3 = \mathbf{x}^{(2)} + \mathbf{V}^{-1}\mathbf{A}^T\mathbf{W}\left(\mathbf{b} - \mathbf{A}\mathbf{x}^{(2)}\right)$$

$$\mathbf{x}^{(3)} = \begin{bmatrix}1.67\\1.13\\2.88\\3.33\end{bmatrix} + \begin{bmatrix}0.167 & 0 & 0.167 & 0 & 0.167\\0.25 & 0 & 0 & 0.25 & 0\\0 & 0.25 & 0 & 0 & 0.25\\0 & 0.167 & 0.167 & 0.167 & 0\end{bmatrix}\left(\begin{bmatrix}3\\7\\5\\6\\4\end{bmatrix} - \begin{bmatrix}1 & 1 & 0 & 0\\0 & 0 & 1 & 1\\1 & 0 & 0 & 1\\0 & 1 & 0 & 1\\1 & 0 & 1 & 0\end{bmatrix}\begin{bmatrix}1.67\\1.13\\2.88\\3.33\end{bmatrix}\right)$$

1.44	2.06
2.94	3.56

$$\mathbf{x}^{(3)} = \begin{bmatrix}1.44\\2.06\\2.94\\3.56\end{bmatrix}$$

4th cycle: All measured data (**b**), the whole weight (**A**) matrix and initial values ($\mathbf{x}^{(3)}$) are used.

1.44	2.06
2.94	3.56

$$\mathbf{x}^4 = \mathbf{x}^{(3)} + \mathbf{V}^{-1}\mathbf{A}^T\mathbf{W}\left(\mathbf{b} - \mathbf{A}\mathbf{x}^{(3)}\right)$$

$$\mathbf{x}^{(4)} = \begin{bmatrix}1.44\\2.06\\2.94\\3.56\end{bmatrix} + \begin{bmatrix}0.167 & 0 & 0.167 & 0 & 0.167\\0.25 & 0 & 0 & 0.25 & 0\\0 & 0.25 & 0 & 0 & 0.25\\0 & 0.167 & 0.167 & 0.167 & 0\end{bmatrix}\left(\begin{bmatrix}3\\7\\5\\6\\4\end{bmatrix} - \begin{bmatrix}1 & 1 & 0 & 0\\0 & 0 & 1 & 1\\1 & 0 & 0 & 1\\0 & 1 & 0 & 1\\1 & 0 & 1 & 0\end{bmatrix}\begin{bmatrix}1.44\\2.06\\2.94\\3.56\end{bmatrix}\right)$$

1.30	2.03
2.97	3.70

$$\mathbf{x}^{(4)} = \begin{bmatrix}1.30\\2.03\\2.97\\3.70\end{bmatrix}$$

5th cycle: All measured data (**b**), the whole weight (**A**) matrix and initial values ($\mathbf{x}^{(4)}$) are used.

1.30	2.03
2.97	3.70

$$\mathbf{x}^{5} = \mathbf{x}^{(4)} + \mathbf{V}^{-1}\mathbf{A}^{T}\mathbf{W}\left(\mathbf{b} - \mathbf{A}\mathbf{x}^{(4)}\right)$$

$$\mathbf{x}^{(5)} = \begin{bmatrix} 1.30 \\ 2.03 \\ 2.97 \\ 3.70 \end{bmatrix} + \begin{bmatrix} 0.167 & 0 & 0.167 & 0 & 0.167 \\ 0.25 & 0 & 0 & 0.25 & 0 \\ 0 & 0.25 & 0 & 0 & 0.25 \\ 0 & 0.167 & 0.167 & 0.167 & 0 \end{bmatrix} \left(\begin{bmatrix} 3 \\ 7 \\ 5 \\ 6 \\ 4 \end{bmatrix} - \begin{bmatrix} 1 & 1 & 0 & 0 \\ 0 & 0 & 1 & 1 \\ 1 & 0 & 0 & 1 \\ 0 & 1 & 0 & 1 \\ 1 & 0 & 1 & 0 \end{bmatrix} \begin{bmatrix} 1.30 \\ 2.03 \\ 2.97 \\ 3.70 \end{bmatrix} \right)$$

1.20	2.02
2.98	3.80

$$\mathbf{x}^{(5)} = \begin{bmatrix} 1.20 \\ 2.02 \\ 2.98 \\ 3.80 \end{bmatrix}$$

6th cycle: All measured data (**b**), the whole weight (**A**) matrix and initial values ($\mathbf{x}^{(5)}$) are used.

1.20	2.02
2.98	3.80

$$\mathbf{x}^{6} = \mathbf{x}^{(5)} + \mathbf{V}^{-1}\mathbf{A}^{T}\mathbf{W}\left(\mathbf{b} - \mathbf{A}\mathbf{x}^{(5)}\right)$$

$$\mathbf{x}^{(6)} = \begin{bmatrix} 1.20 \\ 2.02 \\ 2.98 \\ 3.80 \end{bmatrix} + \begin{bmatrix} 0.167 & 0 & 0.167 & 0 & 0.167 \\ 0.25 & 0 & 0 & 0.25 & 0 \\ 0 & 0.25 & 0 & 0 & 0.25 \\ 0 & 0.167 & 0.167 & 0.167 & 0 \end{bmatrix} \left(\begin{bmatrix} 3 \\ 7 \\ 5 \\ 6 \\ 4 \end{bmatrix} - \begin{bmatrix} 1 & 1 & 0 & 0 \\ 0 & 0 & 1 & 1 \\ 1 & 0 & 0 & 1 \\ 0 & 1 & 0 & 1 \\ 1 & 0 & 1 & 0 \end{bmatrix} \begin{bmatrix} 1.20 \\ 2.02 \\ 2.98 \\ 3.80 \end{bmatrix} \right)$$

1.13	2.01
2.99	3.87

$$\mathbf{x}^{(6)} = \begin{bmatrix} 1.13 \\ 2.01 \\ 2.99 \\ 3.87 \end{bmatrix}$$

Conjugate Gradient Least Squares (CGLS)

To obtain $\mathbf{x}^{(k+1)}$, the weighting matrix, the measured data and the initial values are given. From section 3.2, equations 3-15 to 3-20 are used.

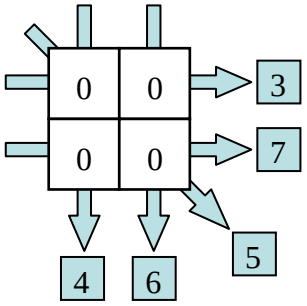

Step 1: calculate the residual ($\mathbf{r}^{(0)}$) for initial values.

$$\mathbf{r}^{(0)} = \mathbf{b} - \mathbf{A}\mathbf{x}^{(0)} = \begin{bmatrix} 3 \\ 7 \\ 5 \\ 6 \\ 4 \end{bmatrix} - \left(\begin{bmatrix} 1 & 1 & 0 & 0 \\ 0 & 0 & 1 & 1 \\ 1 & 0 & 0 & 1 \\ 0 & 1 & 0 & 1 \\ 1 & 0 & 1 & 0 \end{bmatrix} \begin{bmatrix} 0 \\ 0 \\ 0 \\ 0 \end{bmatrix} \right) = \begin{bmatrix} 3 \\ 7 \\ 5 \\ 6 \\ 4 \end{bmatrix}$$

Step 2: calculate the conjugate vector ($\mathbf{p}^{(0)}$) for initial values.

$$\mathbf{p}^{(0)} = \mathbf{A}^T\mathbf{r}^0 = \begin{bmatrix} 1 & 1 & 0 & 0 \\ 0 & 0 & 1 & 1 \\ 1 & 0 & 0 & 1 \\ 0 & 1 & 0 & 1 \\ 1 & 0 & 1 & 0 \end{bmatrix}^T \begin{bmatrix} 3 \\ 7 \\ 5 \\ 6 \\ 4 \end{bmatrix} = \begin{bmatrix} 12 \\ 9 \\ 11 \\ 18 \end{bmatrix}$$

Step 3: Calculate $\psi^{(0)}$ for initial values.

$$\psi^{(0)} = \frac{\left\|\mathbf{A}^T\mathbf{r}^{(0)}\right\|^2}{\left\|\mathbf{A}\mathbf{p}^{(0)}\right\|^2} = \frac{\begin{bmatrix}3\\7\\5\\6\\4\end{bmatrix}^T\begin{bmatrix}1&1&0&0\\0&0&1&1\\1&0&0&1\\0&1&0&1\\1&0&1&0\end{bmatrix}\begin{bmatrix}1&1&0&0\\0&0&1&1\\1&0&0&1\\0&1&0&1\\1&0&1&0\end{bmatrix}^T\begin{bmatrix}3\\7\\5\\6\\4\end{bmatrix}}{\begin{bmatrix}12\\9\\11\\18\end{bmatrix}^T\begin{bmatrix}1&1&0&0\\0&0&1&1\\1&0&0&1\\0&1&0&1\\1&0&1&0\end{bmatrix}^T\begin{bmatrix}1&1&0&0\\0&0&1&1\\1&0&0&1\\0&1&0&1\\1&0&1&0\end{bmatrix}\begin{bmatrix}12\\9\\11\\18\end{bmatrix}} = 0.2$$

Step 4: Calculate $\mathbf{x}^{(1)}$ for the 1st iteration.

2.34	1.75
2.14	3.51

$$\mathbf{x}^{(1)} = \mathbf{x}^{(0)} + \psi^{(0)}\mathbf{p} = \begin{bmatrix}0\\0\\0\\0\end{bmatrix} + 0.2\begin{bmatrix}12\\9\\11\\18\end{bmatrix} = \begin{bmatrix}2.34\\1.75\\2.14\\3.51\end{bmatrix}$$

Step 5: Calculate the residual ($\mathbf{r}^{(1)}$) for the 1st iteration.

$$\mathbf{r}^{(1)} = \mathbf{r}^{(0)} - \psi^{(0)}\mathbf{A}\mathbf{p}^{(0)} = \begin{bmatrix}3\\7\\5\\6\\4\end{bmatrix} - \left(0.2\begin{bmatrix}1&1&0&0\\0&0&1&1\\1&0&0&1\\0&1&0&1\\1&0&1&0\end{bmatrix}\begin{bmatrix}12\\9\\11\\18\end{bmatrix}\right) = \begin{bmatrix}-1.09\\1.35\\-0.84\\0.74\\-0.48\end{bmatrix}$$

Step 6: Calculate $\beta^{(0)}$ the for the 1st iteration.

$$\beta^{(0)} = \frac{\left\|\mathbf{A}^T\mathbf{r}^{(1)}\right\|^2}{\left\|\mathbf{A}^T\mathbf{r}^{(0)}\right\|^2} = \frac{\begin{bmatrix}-1.09\\1.35\\-0.84\\0.74\\-0.48\end{bmatrix}^T\begin{bmatrix}1&1&0&0\\0&0&1&1\\1&0&0&1\\0&1&0&1\\1&0&1&0\end{bmatrix}\begin{bmatrix}1&1&0&0\\0&0&1&1\\1&0&0&1\\0&1&0&1\\1&0&1&0\end{bmatrix}^T\begin{bmatrix}-1.09\\1.35\\-0.84\\0.74\\-0.48\end{bmatrix}}{\begin{bmatrix}3\\7\\5\\6\\4\end{bmatrix}^T\begin{bmatrix}1&1&0&0\\0&0&1&1\\1&0&0&1\\0&1&0&1\\1&0&1&0\end{bmatrix}\begin{bmatrix}1&1&0&0\\0&0&1&1\\1&0&0&1\\0&1&0&1\\1&0&1&0\end{bmatrix}^T\begin{bmatrix}3\\7\\5\\6\\4\end{bmatrix}} = 0.01$$

Step 7: Calculate the conjugate vector ($\mathbf{p}^{(1)}$) for the 1st iteration.

$$\mathbf{p}^{(1)} = \mathbf{A}^T\mathbf{r}^{(1)} + \beta^{(0)}\mathbf{p}^{(0)} = \begin{bmatrix}1&1&0&0\\0&0&1&1\\1&0&0&1\\0&1&0&1\\1&0&1&0\end{bmatrix}^T\begin{bmatrix}-1.09\\1.35\\-0.84\\0.74\\-0.48\end{bmatrix} + 0.01\begin{bmatrix}12\\9\\11\\18\end{bmatrix} = \begin{bmatrix}-2.26\\-0.24\\1.01\\1.47\end{bmatrix}$$

Step 8: Calculate for the 1st iteration

$$\psi^{(1)} = \frac{\left\|\mathbf{A}^T\mathbf{r}^{(1)}\right\|^2}{\left\|\mathbf{A}\mathbf{p}^{(1)}\right\|^2} = \frac{\begin{bmatrix}-1.09\\1.35\\-0.84\\0.74\\-0.48\end{bmatrix}^T\begin{bmatrix}1&1&0&0\\0&0&1&1\\1&0&0&1\\0&1&0&1\\1&0&1&0\end{bmatrix}\begin{bmatrix}1&1&0&0\\0&0&1&1\\1&0&0&1\\0&1&0&1\\1&0&1&0\end{bmatrix}^T\begin{bmatrix}-1.09\\1.35\\-0.84\\0.74\\-0.48\end{bmatrix}}{\begin{bmatrix}-2.26\\-0.24\\1.01\\1.47\end{bmatrix}^T\begin{bmatrix}1&1&0&0\\0&0&1&1\\1&0&0&1\\0&1&0&1\\1&0&1&0\end{bmatrix}^T\begin{bmatrix}1&1&0&0\\0&0&1&1\\1&0&0&1\\0&1&0&1\\1&0&1&0\end{bmatrix}\begin{bmatrix}-2.26\\-0.24\\1.01\\1.47\end{bmatrix}} = 0.51$$

Then repeat step 4 to 8 for the 2nd iteration,

1.18	1.63
2.66	4.26

$$\mathbf{x}^{(2)} = \mathbf{x}^{(1)} + \psi^{(1)}\mathbf{p} = \begin{bmatrix} 2.34 \\ 1.75 \\ 2.14 \\ 3.51 \end{bmatrix} + 0.51 \begin{bmatrix} -2.26 \\ -0.24 \\ 1.01 \\ 1.47 \end{bmatrix} = \begin{bmatrix} 1.18 \\ 1.63 \\ 2.66 \\ 4.26 \end{bmatrix}$$

$$\mathbf{r}^{(2)} = \mathbf{r}^{(1)} - \psi^{(1)}\mathbf{A}\mathbf{p}^{(1)} = \begin{bmatrix} -1.09 \\ 1.35 \\ -0.84 \\ 0.74 \\ -0.48 \end{bmatrix} - \left(0.51 \begin{bmatrix} 1 & 1 & 0 & 0 \\ 0 & 0 & 1 & 1 \\ 1 & 0 & 0 & 1 \\ 0 & 1 & 0 & 1 \\ 1 & 0 & 1 & 0 \end{bmatrix} \begin{bmatrix} -2.27 \\ -0.24 \\ 1.01 \\ 1.47 \end{bmatrix} \right) = \begin{bmatrix} 0.19 \\ 0.08 \\ -0.44 \\ 0.11 \\ -0.16 \end{bmatrix}$$

$$\beta^{(1)} = \frac{\left\| \mathbf{A}^T \mathbf{r}^{(2)} \right\|^2}{\left\| \mathbf{A}^T \mathbf{r}^{(1)} \right\|^2} = \frac{\begin{bmatrix} 0.19 \\ 0.08 \\ -0.44 \\ 0.11 \\ -0.16 \end{bmatrix}^T \begin{bmatrix} 1 & 1 & 0 & 0 \\ 0 & 0 & 1 & 1 \\ 1 & 0 & 0 & 1 \\ 0 & 1 & 0 & 1 \\ 1 & 0 & 1 & 0 \end{bmatrix} \begin{bmatrix} 1 & 1 & 0 & 0 \\ 0 & 0 & 1 & 1 \\ 1 & 0 & 0 & 1 \\ 0 & 1 & 0 & 1 \\ 1 & 0 & 1 & 0 \end{bmatrix}^T \begin{bmatrix} 0.19 \\ 0.08 \\ -0.44 \\ 0.11 \\ -0.16 \end{bmatrix}}{\begin{bmatrix} -1.09 \\ 1.35 \\ -0.84 \\ 0.74 \\ -0.48 \end{bmatrix}^T \begin{bmatrix} 1 & 1 & 0 & 0 \\ 0 & 0 & 1 & 1 \\ 1 & 0 & 0 & 1 \\ 0 & 1 & 0 & 1 \\ 1 & 0 & 1 & 0 \end{bmatrix} \begin{bmatrix} 1 & 1 & 0 & 0 \\ 0 & 0 & 1 & 1 \\ 1 & 0 & 0 & 1 \\ 0 & 1 & 0 & 1 \\ 1 & 0 & 1 & 0 \end{bmatrix}^T \begin{bmatrix} -1.09 \\ 1.35 \\ -0.84 \\ 0.74 \\ -0.48 \end{bmatrix}} = 003$$

$$\mathbf{p}^{(2)} = \mathbf{A}^T \mathbf{r}^{(2)} + \beta^{(1)}\mathbf{p}^{(1)} = \begin{bmatrix} 1 & 1 & 0 & 0 \\ 0 & 0 & 1 & 1 \\ 1 & 0 & 0 & 1 \\ 0 & 1 & 0 & 1 \\ 1 & 0 & 1 & 0 \end{bmatrix}^T \begin{bmatrix} 0.19 \\ 0.08 \\ -0.44 \\ 0.11 \\ -0.16 \end{bmatrix} + 0.03 \begin{bmatrix} -2.2647 \\ -0.2378 \\ 1.0078 \\ 1.472 \end{bmatrix} = \begin{bmatrix} -0.14 \\ 0.29 \\ 0.27 \\ -0.21 \end{bmatrix}$$

$$\psi^{(2)} = \frac{\left\|\mathbf{A}^T\mathbf{r}^{(2)}\right\|^2}{\left\|\mathbf{A}\mathbf{p}^{(2)}\right\|^2} = \frac{\begin{bmatrix} 0.19 \\ 0.08 \\ -0.44 \\ 0.11 \\ -0.16 \end{bmatrix}^T \begin{bmatrix} 1 & 1 & 0 & 0 \\ 0 & 0 & 1 & 1 \\ 1 & 0 & 0 & 1 \\ 0 & 1 & 0 & 1 \\ 1 & 0 & 1 & 0 \end{bmatrix} \begin{bmatrix} 1 & 1 & 0 & 0 \\ 0 & 0 & 1 & 1 \\ 1 & 0 & 0 & 1 \\ 0 & 1 & 0 & 1 \\ 1 & 0 & 1 & 0 \end{bmatrix}^T \begin{bmatrix} 0.19 \\ 0.08 \\ -0.44 \\ 0.11 \\ -0.16 \end{bmatrix}}{\begin{bmatrix} -0.14 \\ 0.29 \\ 0.27 \\ -0.21 \end{bmatrix}^T \begin{bmatrix} 1 & 1 & 0 & 0 \\ 0 & 0 & 1 & 1 \\ 1 & 0 & 0 & 1 \\ 0 & 1 & 0 & 1 \\ 1 & 0 & 1 & 0 \end{bmatrix}^T \begin{bmatrix} 1 & 1 & 0 & 0 \\ 0 & 0 & 1 & 1 \\ 1 & 0 & 0 & 1 \\ 0 & 1 & 0 & 1 \\ 1 & 0 & 1 & 0 \end{bmatrix} \begin{bmatrix} -0.14 \\ 0.29 \\ 0.27 \\ -0.21 \end{bmatrix}} = 1.25$$

1	2
3	4

$$\mathbf{x}^{(3)} = \mathbf{x}^{(2)} + \psi^{(2)}\mathbf{p} = \begin{bmatrix} 1.18 \\ 1.63 \\ 2.66 \\ 4.26 \end{bmatrix} + 1.25 \begin{bmatrix} -0.14 \\ 0.29 \\ 0.27 \\ -0.21 \end{bmatrix} = \begin{bmatrix} 1 \\ 2 \\ 3 \\ 4 \end{bmatrix}$$